Malaria parasites require a divergent heme oxygenase for apicoplast gene expression and biogenesis

Amanda Mixon Blackwell[1], Yasaman Jami-Alahmadi[2], Armiyaw S. Nasamu[3], Shota Kudo[4], Akinobu Senoo[5], Celine Slam[1], Kouhei Tsumoto[4,6], James A. Wohlschlegel[2], Jose M. M. Caaveiro[4], Daniel E. Goldberg[3*], and Paul A. Sigala[1,3*]

[1]Department of Biochemistry, University of Utah School of Medicine, Salt Lake City, UT; [2]Department of Biological Chemistry, University of California, Los Angeles, CA; [3]Departments of Medicine and Molecular Microbiology, Washington University School of Medicine, St. Louis, MO; [4]Department of Chemistry & Biotechnology, The University of Tokyo, Tokyo, Japan; [5]Department of Protein Drug Discovery, Graduate School of Pharmaceutical Sciences, Kyushu University, Fukuoka, Japan; [6]Department of Bioengineering, University of Tokyo, Tokyo, Japan

***For correspondence:** dgoldberg@wustl.edu, p.sigala@biochem.utah.edu

ABSTRACT:

Malaria parasites have evolved unusual metabolic adaptations that specialize them for growth within heme-rich human erythrocytes. During blood-stage infection, *Plasmodium falciparum* parasites internalize and digest abundant host hemoglobin within the digestive vacuole. This massive catabolic process generates copious free heme, most of which is biomineralized into inert hemozoin. Parasites also express a divergent heme oxygenase (HO)-like protein (PfHO) that lacks key active-site residues and has lost canonical HO activity. The cellular role of this unusual protein that underpins its retention by parasites has been unknown. To unravel PfHO function, we first determined a 2.8 Å-resolution X-ray structure that revealed a highly α-helical fold indicative of distant HO homology. Localization studies unveiled PfHO targeting to the apicoplast organelle, where it is imported and undergoes N-terminal processing but retains most of the electropositive transit peptide. We observed that conditional knockdown of PfHO was lethal to parasites, which died from defective apicoplast biogenesis and impaired isoprenoid-precursor synthesis. Complementation and molecular-interaction studies revealed an essential role for the electropositive N-terminus of PfHO, which selectively associates with the apicoplast genome and enzymes involved in nucleic acid metabolism and gene expression. PfHO knockdown resulted in a specific deficiency in levels of apicoplast-encoded RNA but not DNA. These studies reveal an essential function for PfHO in apicoplast maintenance and suggest that *Plasmodium* repurposed the conserved HO scaffold from its canonical heme-degrading function in the ancestral chloroplast to fulfill a critical adaptive role in organelle gene expression.

INTRODUCTION:

Malaria remains a devastating infectious disease marked by increasing treatment failures with frontline artemisinin therapies[1,2]. *Plasmodium* malaria parasites diverged early in eukaryotic evolution from well-studied yeast and mammalian cells, upon which most understanding of eukaryotic biology is based. Due to this evolutionary divergence, parasites acquired unusual molecular adaptations for specialized growth and survival within human erythrocytes, human hepatocytes, and mosquitos. Unraveling and understanding these adaptations will provide deep insights into the evolution of *Plasmodium* and other apicomplexan parasites and unveil new parasite-specific vulnerabilities that are suitable for therapeutic targeting to combat increasing parasite drug resistance.

Heme metabolism is central to parasite survival within red blood cells (RBCs), the most heme-rich cell in the human body. During blood-stage growth, *Plasmodium* parasites internalize and digest up to 80% of host hemoglobin within the acidic digestive vacuole (DV)[3,4]. This massive digestive process liberates an excess of cytotoxic free heme that is detoxified *in situ* within the DV via biomineralization into chemically inert hemozoin crystals. Other hematophagous organisms and cells, including certain blood-feeding insects and human liver/splenic macrophages that process senescent RBCs, depend on canonical heme oxygenase (HO) enzymes to degrade excess heme and recycle iron[5–7]. In contrast to these examples, *Plasmodium* parasites lack an active HO pathway for enzymatic heme degradation and rely fully on alternative mechanisms for heme detoxification and iron acquisition during blood-stage infection[8]. Nevertheless, malaria parasites express a divergent HO-like protein (PfHO, Pf3D7_1011900) with unusual biochemical features[9]. Although this protein shows distant homology to HO enzymes, it lacks the strictly conserved active-site His ligand and does not degrade heme *in vitro* or in live cells[8]. Genome-wide knockout and insertional mutagenesis studies in *P. berghei* and *P. falciparum* reported that the PfHO gene was refractory to disruption[10,11], but the biological function that underpins the retention and putative essentiality of this divergent HO-like protein in malaria parasites has remained a mystery.

Heme oxygenases are ubiquitous enzymes that retain a conserved α-helical structure and canonically function in regioselective cleavage of the porphyrin macrocycle of heme to release iron[12,13]. HO-catalyzed heme degradation also generates carbon monoxide and a tetrapyrrole cleavage product, typically biliverdin IXα, which is further modified for downstream metabolic utilization or excretion. These reactions play key roles in heme turnover, iron acquisition, oxidative protection, and cellular signaling[5,6,14]. There are also reports of expanded biological roles for HO proteins that are independent of heme degradation. In humans, HO1 has been reported to translocate to the nucleus upon proteolytic processing where it modulates the activity of transcription factors through an unknown mechanism that is independent of its enzymatic activity[15]. HO1-mediated transcriptional changes have been implicated in cell differentiation and physiological stress responses in humans and rats[16,17]. Pseudo-HO enzymes that retain the HO fold but lack the conserved His ligand or heme-degrading function have also been identified in multiple organisms, but their cellular roles remain largely unknown. The best-studied example is from *Arabidopsis thaliana*, which encodes three active (HY1, HO3, and HO4) and one inactive (HO2) heme oxygenase homologs that all localize to the chloroplast[18]. AtHO2 contains an Arg in place of the conserved His and lacks detectable HO activity, and knockout studies suggest an undefined role in photomorphogenesis[14]. Based on these reports of non-canonical HO roles, we set out to unravel the cellular function of PfHO in *P. falciparum*.

We localized PfHO to the parasite apicoplast and demonstrated that conditional knockdown of PfHO disrupts parasite growth and apicoplast biogenesis. We discovered that PfHO interacts with the 35-kb apicoplast genome and requires the electropositive N-terminus, which serves as an apicoplast-targeting transit peptide but is largely retained after organelle import. Loss of PfHO resulted in a strong deficiency in apicoplast-encoded RNA but not DNA levels, suggesting a key role in expression of the apicoplast genome. Phylogenetic analyses indicated that PfHO orthologs are selectively retained by hematozoan parasites, including *Babesia* and *Theileria*, but not by other apicomplexan organisms. This

study illuminates an essential role for a catalytically inactive HO-like protein in gene expression and biogenesis of the *Plasmodium* apicoplast.

RESULTS:

PfHO is a divergent HO homolog. Sequence analysis of PfHO provides limited insights into the origin and function of this protein. Previous studies identified low (15-20%) sequence identity between PfHO and known heme oxygenases from humans (human HO1, HuHO1), cyanobacteria (*Synechocystis* sp. PCC 6803 HO1, SynHO1), and plants (*A. thaliana* HO4, AtHO4)[8,9]. The N-terminal 95 residues of PfHO, which show sequence similarity only to other *Plasmodium* orthologs, display hydrophobic and electropositive features suggestive of sub-cellular targeting (**Figure 1A**), which is discussed below. Sequence homology searches with PfHO using NCBI BLAST[19] and Hidden Markov Modeling tools[20] revealed highest identity (65-99%) to protein orthologs in other *Plasmodium* species, with the next highest sequence identity (30-35%) to proteins in the hematozoan parasites, *Babesia* and *Theileria* (**Figure 1 – figure supplement 1**). These PfHO orthologs also lack the conserved active-site His residue and other sequence features required for enzymatic function. However, we were unable to identify convincing PfHO orthologs in apicomplexan organisms outside of blood-infecting hematozoan parasites, as previously reported[21]. Phylogenic analysis of HO sequences from mammals, plants, algae, insects, and parasites further highlighted the divergence of heme oxygenases between these clades of organisms (**Figure 1 – figure supplement 2**).

The low level of sequence identity to known HO enzymes and loss of heme-degrading activity by PfHO strongly suggested a repurposing of the HO scaffold for an alternative function in *Plasmodium*. As an initial step towards understanding this divergent function, we determined a 2.8 Å-resolution X-ray crystal structure of the HO-like domain of PfHO (residues 84-305) in its unliganded state (**Figure 1B and Figure 1 – figure supplement 3**), as we were unable to crystalize PfHO$^{84-305}$ in the presence of bound heme. The structure obtained for apo-PfHO$^{84-305}$ was highly α-helical with an overall fold expected for an HO homolog (**Figure 1B and Figure 1C**), including strong concordance in the positions of α-helix-forming sequences between PfHO, HuHO1, and SynHO1 (**Figure 1A**). Although the purified protein contained residues 84-305, electron density to support structural modeling began with residue 95 at the start of an

α-helix, suggesting that residues 84-94 are disordered. A structural homology search using the DALI Protein Structure Comparison Server[22] revealed strong structural similarity between PfHO and structures of HO enzymes from plants, mammals, and cyanobacteria (**Figure 1D**). Superposition of crystal structures for PfHO and SynHO1 revealed very similar α-helical folds, with a root-mean-square deviation (RMSD) in the positions of backbone atoms of 2.11 Å for the two structures (**Figure 1B**).

Despite overall structural similarity between PfHO and SynHO1, we noted several points of structural divergence beyond loss of the conserved His ligand. In structures of HO enzymes (including SynHO1), heme is sequestered within an active-site binding pocket formed by a distal helix positioned above the bound heme and a proximal helix below the heme that contains the conserved His ligand (**Figure 1B**). In our PfHO structure, the distal helix adopted a similar architecture to that observed in the SynHO1 structure but featured bulkier, charged Lys-Glu residues in place of the conserved Gly-Gly sequence in active HOs[23] (**Figure 1A**). In contrast to the ordered distal helix, we were unable to resolve the structure of the C-terminal region of the proximal helix (residues 112-133) of PfHO due to weak electron density for these residues, possibly reflecting static or dynamic structural disorder in this region. We note that ordered, coiled loops were observed at the C-terminal end of the proximal helix in recent structures of plant HOs[24,25] (**Figure 1 – figure supplement 4**). Nevertheless, disorder in the C-terminal region of the proximal helix has previously been described in a structure of human HO1 bound to synthetic 5-phenylheme (where the 5-phenyl substituent sterically disrupts proximal helix structure near the α-meso carbon) and a structure of apo rat HO1 that lacked bound heme[26,27].

To model a possible structure for the proximal helix of PfHO as a basis for evaluating its electrostatic properties, we turned to a predicted AlphaFold[28] structure for PfHO, which was very similar to our crystal structure (backbone RMSD of 0.57 Å). AlphaFold predicts a sharp kink in the proximal helix of PfHO that extends the position of this helix by several angstroms compared to the proximal helix in SynHO1 (**Figure 1C**). We also noted that the PfHO AlphaFold model predicted that residues 84-94 were

unstructured, consistent with our inability to observe electron density for these residues in our X-ray data. We identified changes in the calculated electrostatic surface potential[29] of PfHO$^{84-305}$ between the proximal and distal helices that diminish the electropositive potential in this region compared to HuHO1 and SynHO1 (**Figure 1 – figure supplement 5**). The positive charge character around the heme-binding pocket in canonical HOs interacts electrostatically with propionate groups of heme and mediates HO association with electronegative electron donors (e.g., ferredoxin and cytochrome P450 reductase) required for HO activity[26,30,31]. Based on these observations, we conclude that PfHO is a divergent HO homolog that retains the overall HO fold but has lost key active-site and surface features that suggest a unique function independent of heme degradation.

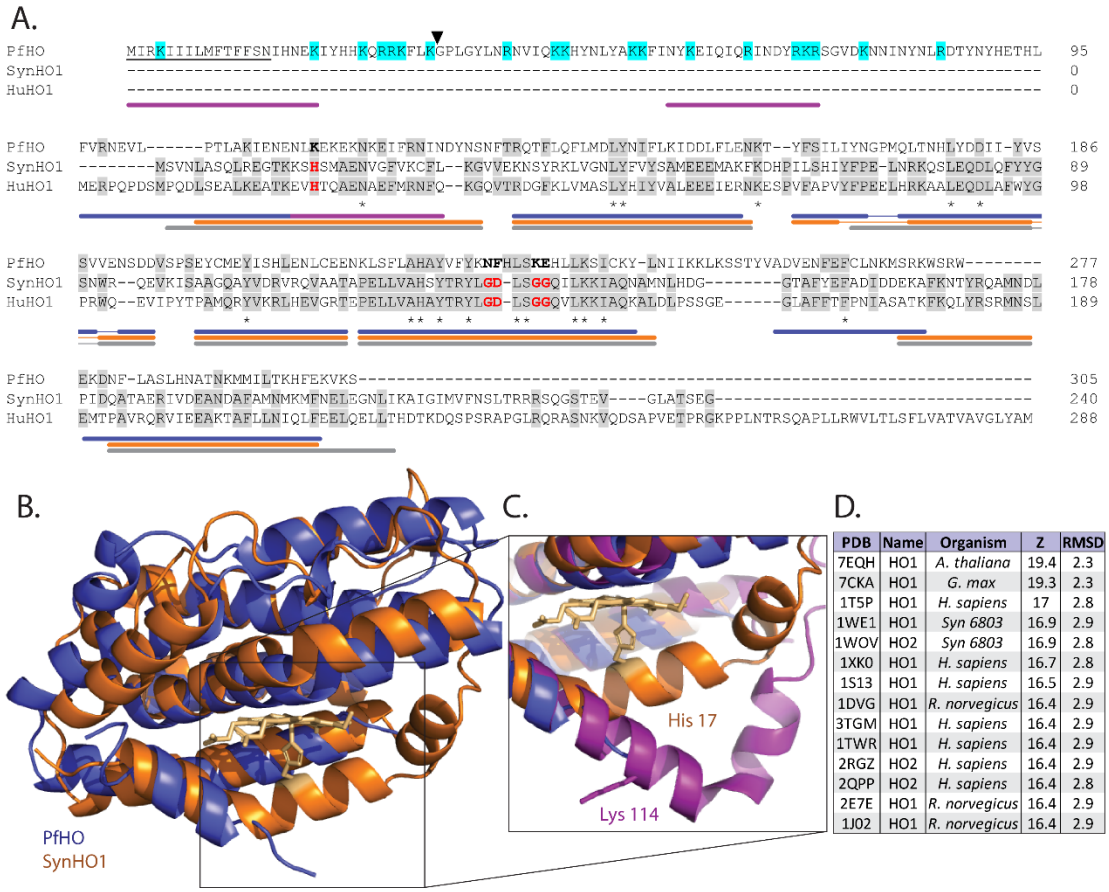

PDB	Name	Organism	Z	RMSD
7EQH	HO1	*A. thaliana*	19.4	2.3
7CKA	HO1	*G. max*	19.3	2.3
1T5P	HO1	*H. sapiens*	17	2.8
1WE1	HO1	*Syn 6803*	16.9	2.9
1WOV	HO2	*Syn 6803*	16.9	2.8
1XK0	HO1	*H. sapiens*	16.7	2.8
1S13	HO1	*H. sapiens*	16.5	2.9
1DVG	HO1	*R. norvegicus*	16.4	2.9
3TGM	HO1	*H. sapiens*	16.4	2.9
1TWR	HO1	*H. sapiens*	16.4	2.9
2RGZ	HO2	*H. sapiens*	16.4	2.9
2QPP	HO2	*H. sapiens*	16.4	2.8
2E7E	HO1	*R. norvegicus*	16.4	2.9
1J02	HO1	*R. norvegicus*	16.4	2.9

Figure 1: Sequence and structural homology of PfHO. A) Sequence alignment of *P. falciparum* (PfHO, Q8IJS6), cyanobacterial (SynHO1, P72849), and human (HuHO1, P09601) heme oxygenase homologs (Uniprot ID). Conserved histidine ligand and distal helix residues required for catalysis in SynHO1 and HuHO1 are marked in red, and identical residues in aligned sequences are in gray. Asterisks indicate identical residues in all three sequences. The predicted N-terminal signal peptide of PfHO is underlined, electropositive residues in the PfHO leader sequence are highlighted in cyan, and the black arrow marks the putative targeting peptide processing site. Colored bars below the sequence alignment mark locations of α helices observed in crystal structures of PfHO (blue), SynHO1 (orange), and HuHO1 (grey), and the AlphaFold structural prediction for PfHO (purple). B) Structural superposition of the 2.8 Å-resolution X-ray crystal structure of apo-PfHO$^{84\text{-}305}$ (blue, PDB: 8ZLD) and the 2.5 Å-resolution X-ray structure of cyanobacterial, SynHO1 (orange, PDB: 1WE1). C) Structural superposition of the proximal helix for SynHO1 active site (orange), PfHO crystal structure (blue), and the AlphaFold structural prediction of PfHO (purple). D) Top-scoring protein structures in the PDB identified by the DALI server based on structural similarity to the X-ray crystal structure of PfHO$^{84\text{-}305}$. RMSD is calculated in angstroms (Å), and Z-score is a unitless parameter describing similarity, where greater value indicates higher similarity[32].

Figure supplement 1. Sequence homologs of PfHO based on BLAST[19] and HMM[20] searches.

Figure supplement 2. Phylogenic tree of mammalian, plant, algal, and hematozoan HOs.

Figure supplement 3. X-ray crystallographic data collection and structure refinement statistics for PfHO.

Figure supplement 4. Sequence and structural alignments of PfHO to plant HOs (AtHO1, GmHO1).

Figure supplement 5. HO surface charge features.

Source data 1. PDB file for 2.8 Å-resolution structure of PfHO.

PfHO is targeted to the apicoplast organelle. The *Plasmodium*-specific N-terminus of PfHO has sequence features that suggested a possible role in sub-cellular targeting. These features include a hydrophobic stretch of ~12 residues at the N-terminus followed by electropositive sequence of ~80 residues that are characteristic of signal and transit peptides, respectively, which direct proteins to the apicoplast organelle[33,34]. Analysis using the apicoplast-targeting prediction software, PlasmoAP, identified strong sequence characteristics of an apicoplast transit peptide, but its SignalP 2.0 module failed to identify a signal peptide[8,34]. However, more recent SignalP versions (5.0 and 6.0)[35] and Phobius[36] strongly predicted a signal peptide with a consensus cleavage site after N18 (**Figure 1A**). These features, together with known HO targeting to chloroplasts in plants[18] and prior detection of PfHO in pulldown studies of apicoplast-targeted proteins[37], suggested that PfHO likely targets to the apicoplast.

To determine PfHO localization in *P. falciparum* parasites, we stably transfected Dd2 parasites with an episome encoding full-length PfHO with a C-terminal GFP-tag. Live parasite microscopy revealed focal GFP signal that was proximal to but distinct from MitoTracker Red staining of the mitochondrion (**Figure 2A and Figure 2 – figure supplement 1**), which is consistent with PfHO targeting to the apicoplast. Immunofluorescence analysis (IFA) of fixed parasites indicated strong co-localization between PfHO-GFP and the apicoplast acyl carrier protein (ACP, Pf3D7_0208500) (**Figure 2A and Figure 2 – figure supplement 2**), providing direct evidence that PfHO targets the apicoplast. Additionally, western blot analysis of parasite lysates revealed two bands by anti-GFP staining that are suggestive of precursor and N-terminally processed forms, as typically observed for apicoplast-targeted proteins[33] (**Figure 2B**).

To further test this conclusion, we stably disrupted the apicoplast by culturing parasites for one week in 1 µM doxycycline (Dox) with rescue by 200 µM isopentenyl pyrophosphate (IPP) to decouple parasite viability from apicoplast function. In these conditions, the apicoplast is lost and proteins targeted to the organelle accumulate in dispersed cytoplasmic foci[38]. As expected for an apicoplast-targeted protein, episomally expressed PfHO-GFP in Dox/IPP-treated parasites displayed a speckled constellation

of dispersed fluorescent foci in each cell (**Figure 2C and Figure 2 – figure supplement 1**). Furthermore, western blot analysis of parasite lysates after Dox/IPP-treatment revealed only a single band by anti-GFP staining at the size of the precursor protein, providing evidence that PfHO processing depends on import into the apicoplast (**Figure 2B**).

To directly test whether the N-terminal leader sequence of PfHO is sufficient for apicoplast targeting, we episomally expressed the PfHO N-terminus (residues 1-83) fused to a C-terminal GFP tag in Dd2 parasites and observed a nearly identical pattern of GFP signal in live and fixed parasites compared to full-length PfHO (**Figure 2D and Figure 2 – figure supplements 1 and 2**), as well as both precursor and processed bands by western blot analysis (**Figure 2E**). In Dox/IPP-treated parasites, PfHO N-term-GFP signal appeared as dispersed fluorescent foci (**Figure 2F and Figure 2 – figure supplement 1**). Based on these observations, we conclude that PfHO is targeted by its N-terminal leader sequence for import into the apicoplast where it undergoes proteolytic processing. This processing and previously reported protein associations for PfHO[37] suggest targeting to the apicoplast matrix. Studies described below for endogenously tagged PfHO further support this conclusion.

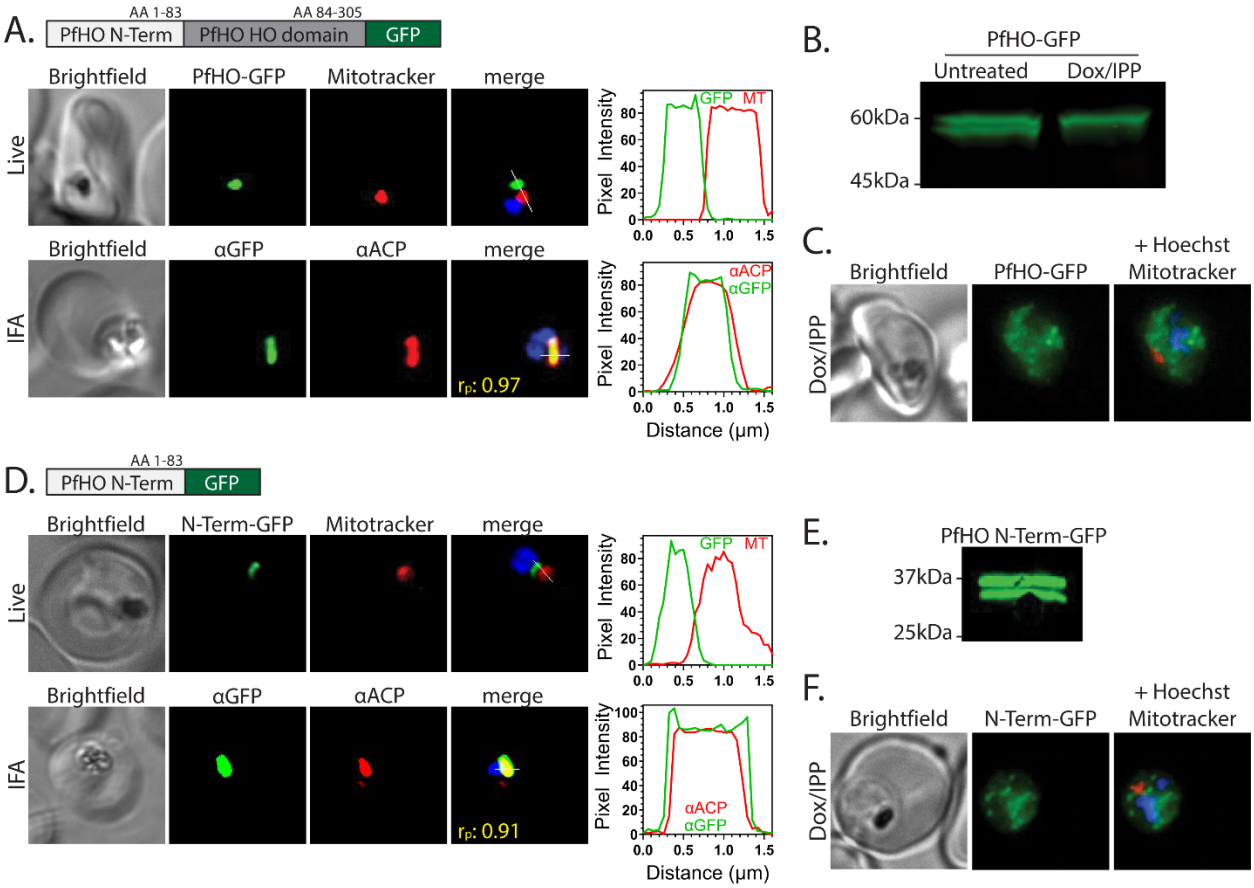

Figure 2: PfHO localization and processing. A) Widefield fluorescence microscopy of Dd2 parasites episomally expressing PfHO-GFP. For live imaging, parasites were stained with 25 nM Mitotracker Red and 10 nM Hoechst. For IFA, parasites were fixed and stained with anti-GFP and anti-apicoplast ACP antibodies, as well as DAPI. The average Pearson correlation coefficient (r_p) of red and green channels based on all images is given. Pixel intensity plots as a function of distance along the white line in merged images are displayed graphically beside each parasite. B) Western blot of untreated or Dox/IPP-treated parasites episomally expressing PfHO-GFP and stained with anti-GFP antibody. C) Live microscopy of PfHO-GFP parasites cultured 7 days in 1 µM doxycycline (Dox) and 200 µM IPP and stained with 25 nM Mitotracker Red and 10 nM Hoechst. D) Widefield fluorescence microscopy of Dd2 parasites episomally expressing PfHO N-term-GFP and stained as in panel A. E) Western blot of parasites episomally expressing PfHO N-term-GFP and stained with anti-GFP antibody. F) Live microscopy of PfHO N-term-GFP parasites cultured 7 days in 1 µM Dox and 200 µM IPP, and stained as in panel C.

Figure supplement 1. Additional widefield fluorescence microscopy of live Dd2 parasites episomally expressing PfHO-GFP and PfHO N-Term-GFP.

Figure supplement 2. Additional widefield IFA microscopy of fixed Dd2 parasites episomally expressing PfHO-GFP and PfHO N-Term-GFP.

Source data 1. Uncropped western blots of untreated or Dox/IPP-treated parasites episomally expressing PfHO-GFP in figure 2B.

Source data 2. Uncropped western blots of untreated parasites episomally expressing PfHO N-term-GFP in figure 2E.

PfHO is essential for parasite viability and apicoplast biogenesis. To directly test PfHO essentiality in blood-stage parasites, we edited the PfHO gene to enable conditional knockdown. We first used restriction endonuclease-mediated integration[39] or CRISPR/Cas9 to tag PfHO with either a C-terminal GFP-tag and the DHFR-destabilization domain[40,41] in 3D7 (PM1 KO)[42] parasites or a C-terminal dual hemagglutinin (HA_2) tag and the glmS ribozyme[43,44] in Dd2 parasites, respectively (**Figure 3 – figure supplement 1**). Although neither system provided substantial downregulation of PfHO expression, we used the GFP-tagged parasites to confirm apicoplast targeting and processing of endogenous PfHO. Western blot analysis of parasites expressing PfHO-GFP-$DHFR_{DD}$ revealed two bands by anti-GFP staining and only a single precursor protein band upon apicoplast disruption in Dox/IPP conditions (**Figure 3A**). Additionally, co-localization of anti-GFP and anti-ACP staining by IFA confirmed apicoplast targeting of endogenous PfHO-GFP-$DHFR_{DD}$ (**Figure 3 – figure supplement 2**). Immunogold transmission electron microscopy (TEM) of fixed parasites stained with anti-GFP and anti-ACP antibodies co-localized both proteins within a single multi-membrane compartment, as expected for targeting to the apicoplast. We noted that PfHO appeared to preferentially associate with the innermost apicoplast membrane, while ACP signal was distributed throughout the apicoplast matrix (**Figure 3B and Figure 3 – figure supplement 3**).

We next used CRISPR/Cas9 to tag the PfHO gene in Dd2 parasites to encode the aptamer/TetR-DOZI system, which places protein expression under control of the non-toxic small molecule, anhydrotetracycline (aTC)[45]. The PfHO gene was edited to include both a single aptamer at the 5' end and a 10x aptamer cassette at the 3' end[46,47] but without introducing an epitope tag in the encoded protein sequence. Correct integration into the PfHO locus was validated by genomic PCR and Southern blot (**Figure 3 – figure supplement 4**). Because the protein was untagged, we made a custom rabbit polyclonal antibody that was raised against the HO-like domain of PfHO and selectively recognized PfHO expressed in parasites and *E. coli* (**Figure 3 – figure supplement 5**). Using the aptamer-tagged parasites and this custom antibody, we performed western blot analysis to confirm detection of endogenous PfHO in +aTC

conditions, including observation of precursor and processed bands. Critically, we observed that growth in -aTC conditions reduced PfHO levels by >85% (**Figure 3C**), indicating substantial downregulation of PfHO protein expression. PfHO mRNA levels were also selectively decreased by ~75% upon aTC washout, consistent with prior reports that TetR-DOZI association with transcripts targets mRNA to P-bodies for degradation (**Figure 3 – figure supplement 6**)[48–50]. Because of the consistency and stringency of knockdown achieved by the PfHO-aptamer/TetR-DOZI system, all subsequent knockdown experiments were performed in this line.

By synchronous growth assay we found that PfHO knockdown in -aTC conditions resulted in a severe growth defect and widespread parasite death in the third intraerythrocytic growth cycle (**Figure 3C and Figure 3 – figure supplement 7**). Parasite growth was fully rescued by culture supplementation with the key apicoplast product, isopentenyl pyrophosphate (IPP)[38], with IPP washout after four days in -aTC/+IPP conditions resulting in rapid parasite death (**Figure 3C**). These observations directly support the conclusion that PfHO is essential for blood-stage parasite viability and has a critical function within the apicoplast. To test if PfHO knockdown impacted apicoplast biogenesis, we transfected PfHO-aptamer/TetR-DOZI parasites with the PfHO N-term-GFP episome to label the apicoplast. By widefield fluorescence microscopy, we observed that live parasites in +aTC conditions had focal GFP expression. In contrast, parasites cultured five days in -aTC/+IPP conditions displayed dispersed fluorescent foci in most parasites **(Figure 3D and Figure 3 – figure supplement 8**). Using qPCR, we determined that parasites cultured five days in -aTC/+IPP conditions showed a dramatic reduction in apicoplast genomic DNA compared to parasites grown in +aTC conditions (**Figure 3E**). We conclude that PfHO function is essential for apicoplast biogenesis such that its knockdown (+IPP) results in parasite progeny that lack the intact organelle.

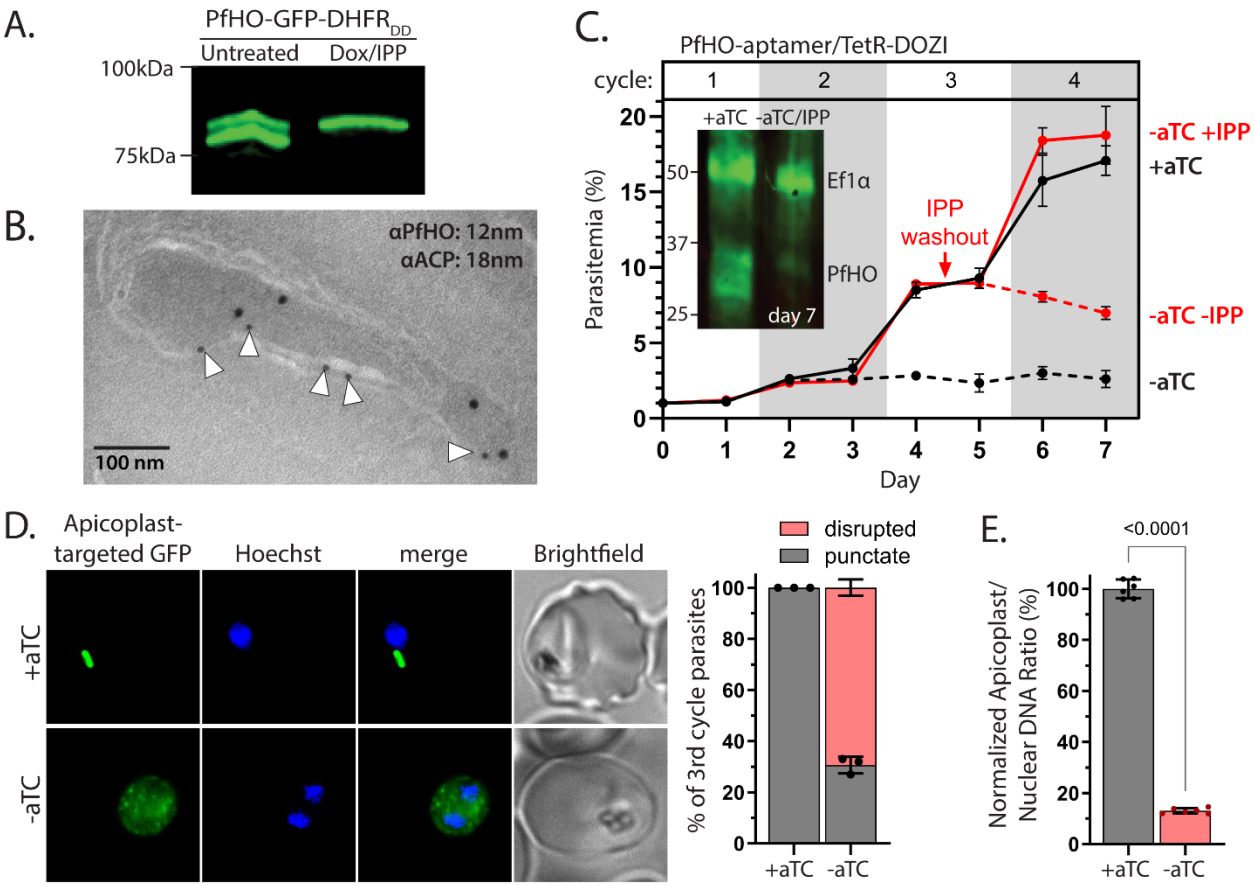

Figure 3: PfHO is essential for parasite viability and apicoplast maintenance. A) Western blot of untreated or Dox/IPP-treated parasites with endogenously tagged PfHO-GFP-DHFR$_{DD}$. B) Immunogold TEM of a fixed 3D7 parasite endogenously expressing PfHO-GFP-DHFR$_{DD}$ and stained with anti-GFP (12 nm, white arrows) and anti-apicoplast ACP (18 nm) antibodies. C) Synchronized growth assay of Dd2 parasites tagged at the PfHO locus with the aptamer/TetR-DOZI system and grown ± 1 µM aTC and ± 200 µM IPP. Data points are the average ±SD of biological triplicates. Inset: western blot analysis of PfHO expression for parasites grown 7 days ±aTC with 200 µM IPP and stained with custom anti-PfHO antibody and anti-translation elongation factor 1α (Ef1α) as loading control. Densitometry of western blot bands indicated >85% reduction in PfHO expression. D) Live microscopy of PfHO-aptamer/TetR-DOZI parasites episomally expressing apicoplast-localized GFP (PfHO N-Term-GFP) grown 5 days ±aTC with 200 µM IPP. Right: Population analysis of apicoplast morphology scored for punctate versus dispersed GFP signal in 110 total parasites from biological triplicate experiments. Statistical significance was calculated by Student's *t*-test. E) Quantitative PCR analysis of the apicoplast: nuclear genome ratio for PfHO-aptamer/TetR-DOZI parasites cultured 5 days ±aTC with 200 µM IPP, based on amplification of apicoplast (SufB: Pf3D7_API04700, ClpM: Pf3D7_API03600, TufA: Pf3D7_API02900) relative to nuclear (STL: Pf3D7_0717700, I5P: Pf3D7_0802500, ADSL: Pf3D7_0206700) genes. Indicated qPCR ratios were normalized to +aTC and are the average ±SD of biological triplicates. Significance of ±aTC difference was analyzed by Student's *t*-test.

Figure supplement 1. Schemes for modification of the PfHO genomic locus to integrate the C-terminal GFP-DHFR$_{DD}$ or HA$_2$-glmS tags.

Figure supplement 2. IFA microscopy of 3D7 parasites expressing PfHO-GFP-DHFR$_{DD}$.

Figure supplement 3. Additional immunogold TEM images of 3D7 parasites expressing PfHO-GFP-DHFR$_{DD}$.

Figure supplement 4. Scheme for modification of the PfHO genomic locus to integrate the aptamer/TetR-DOZI system.

Figure supplement 5. Validation of custom PfHO antibody specificity.

Figure supplement 6. Quantitative PCR of PfHO expression ±aTC with 200 µM IPP.

Figure supplement 7. Giemsa-stained smears of PfHO-aptamer/TetR-DOZI parasites grown in ±aTC.

Figure supplement 8. Additional fluorescence microscopy images of PfHO-aptamer/TetR-DOZI parasites episomally expressing apicoplast-localized GFP grown 5 days ±aTC with 200 µM IPP.

Source data 1. Uncropped western blots of parasites with endogenously tagged PfHO-GFP-DHFR$_{DD}$.

Source data 2. Uncropped western blot of PfHO expression

Source data 3. Uncropped Southern blot of parasite DNA from PfHO-GFP-DHFR$_{DD}$ cultures.

Source data 4. Uncropped PCR gel of parasite DNA from PfHO- HA$_2$-glmS cultures.

Source data 5. Uncropped PCR gel of parasite DNA from PfHO-aptamer/TetR-DOZI cultures.

Source data 6. Uncropped Southern blot of parasite DNA from PfHO-aptamer/TetR-DOZI cultures.

Source Data 7. Uncropped western blot of 3D7 parasites stained with rabbit serum prior to inoculation with PfHO protein antigen.

Source Data 8. Uncropped western blot of *E. coli* expressing PfHO$^{84-305}$ and 3D7 parasites stained with crude serum from the final bleed of a rabbit inoculated with PfHO protein antigen.

Electropositive transit peptide of PfHO is largely retained after apicoplast import and required for essential function. Apicoplast-targeted proteins containing bipartite N-terminal leader sequences typically undergo proteolytic cleavage that fully or mostly removes the targeting peptide upon import into the organelle[33,51]. Western blot analyses confirmed that PfHO is N-terminally processed (**Figure 2B and Figure 3A**), but we noted that the size of the mature protein was several kDa larger than the estimated size of $PfHO^{84-305}$ which was previously studied as the mature HO-like domain[8]. Using the endogenously tagged PfHO-HA_2 (glmS) line, we observed that the mature protein migrated by SDS-PAGE/western blot with an apparent molecular mass of ~34 kDa while the HO-like domain ($PfHO^{84-305}$-HA_2) recombinantly expressed in *E. coli* migrated at ~31 kDa (**Figure 4A and Figure 3 – figure supplement 4**). This observation strongly suggested that only a portion of the targeting sequence was removed upon apicoplast import and that additional N-terminal sequence beyond the HO-like domain was present in mature PfHO. Based on this approximate size difference, we estimated that ~30-40 residues of the apicoplast-targeting sequence upstream of residue 84 were likely retained in mature PfHO.

To specify the N-terminus of mature PfHO, we immunoprecipitated endogenous PfHO from parasites using the PfHO-specific antibody, fractionated the eluted sample by SDS-PAGE, transferred to PVDF membrane, and performed N-terminal protein sequencing of the Coomassie-stained band corresponding to mature PfHO. This analysis suggested an N-terminal sequence of GPLGYLNR, which corresponds to a single sequence starting at residue 33 within the electropositive transit peptide of PfHO (**Figure 1A**). Mass spectrometry analysis of PfHO protein purified from parasites and subjected to tryptic digest provided broad peptide coverage of PfHO sequence and identified GPLGYLNR as the most N-terminal peptide that was detected (**Figure 4 – figure supplement 1**). The calculated molecular mass of 35.3 kDa for $PfHO^{33-305}$-HA_2 is similar to the observed SDS-PAGE migration for mature PfHO-HA_2 ~34 kDa (**Figure 4A**). Based on these observations, we conclude that PfHO is proteolytically processed upon

apicoplast import to remove part but not all of the targeting peptide and result in an N-terminus at or near Gly_{33} in mature PfHO.

Cleavage before Gly_{33} leaves ~50 residues of the electropositive targeting peptide attached to the HO-like domain of mature PfHO. Intrinsic structural disorder is a fundamental property of apicoplast-targeting peptides[52]. Consistent with overall structural heterogeneity in these ~50 residues, we were unable to crystallize recombinant $PfHO^{33-305}$ that matched the mature protein, despite the presence of the structured HO-like domain. Nevertheless, we note that AlphaFold predicts that residues 57-72 of the N-terminus form an α-helix that folds across the HO-like domain of PfHO between the proximal and distal helices **(Figure 4B**). Additionally, the abundance of Arg and Lys residues within the retained N-terminal sequence (**Figure 1A**) grants a strong electropositive character to the surface of mature PfHO (**Figure 4B**).

To test if this retained N-terminal sequence contributes to essential PfHO function beyond a role in apicoplast targeting, we performed complementation studies using PfHO knockdown parasites. We transfected the PfHO-aptamer/TetR-DOZI parasites with episomes encoding the PfHO N-terminus fused to GFP ($PfHO^{1-83}$-GFP), the HO-like domain of PfHO fused to the apicoplast ACP leader sequence (1-60)[33] on its N-terminus and GFP on its C-terminus (ACP_L-$PfHO^{84-305}$-GFP), or full-length PfHO-GFP. We first confirmed knockdown of endogenous PfHO under -aTC conditions and proper expression and processing of the episomally expressed proteins in these parasite lines (**Figure 2 and Figure 4 – figure supplements 2 and 3**). Although all three proteins were correctly targeted to the apicoplast and proteolytically processed, only expression of full-length PfHO with cognate leader sequence rescued parasite growth from knockdown of endogenous PfHO (**Figure 4C**). We conclude that the retained N-terminal sequence of mature PfHO contributes to essential function beyond its role in apicoplast targeting.

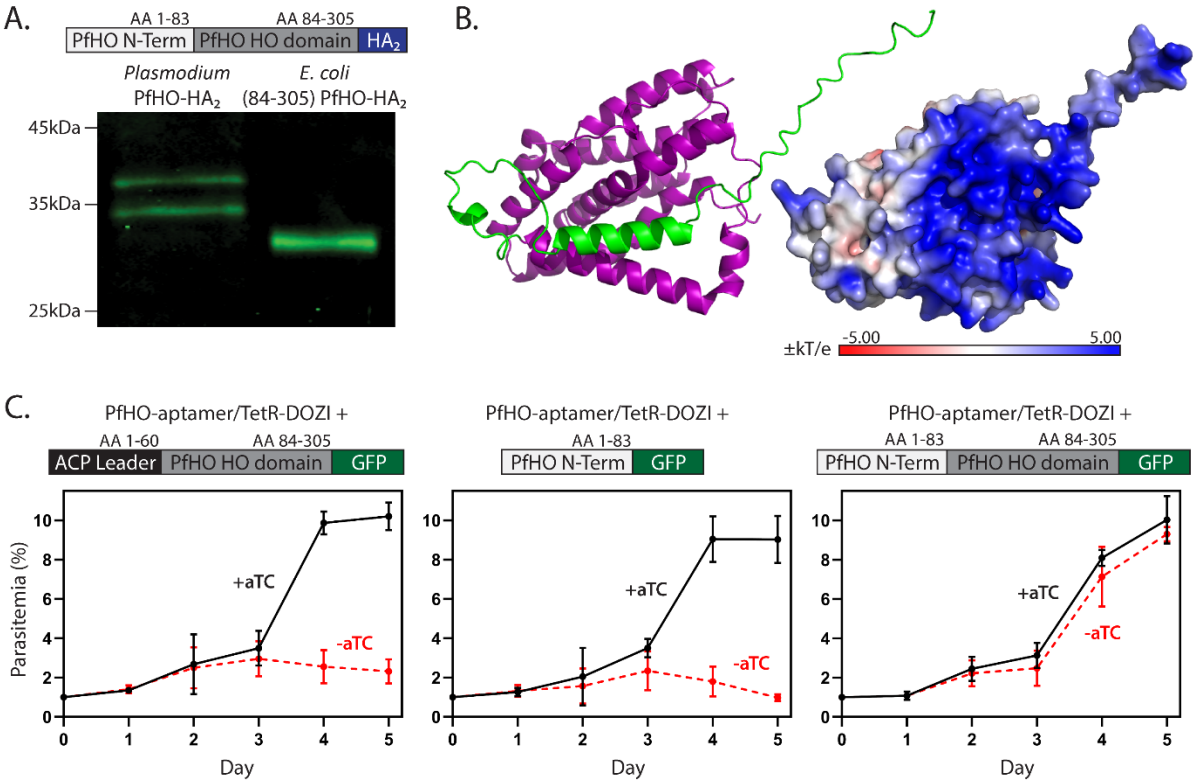

Figure 4: Processing and essentiality of the PfHO N-terminus. A) Western blot of lysates from Dd2 parasites endogenously expressing PfHO-HA_2 and from *E. coli* recombinantly expressing $PfHO^{84-305}$-HA_2. B) AlphaFold structure and electrostatic surface charge predicted for $PfHO^{33-305}$ corresponding to mature PfHO after apicoplast import. C) Synchronized growth assays of PfHO knockdown Dd2 parasites complemented by episomal expression of the indicated PfHO constructs in ±1 µM aTC. Growth assay data points are the average ±SD of biological triplicates.

Figure supplement 1. Peptide coverage of PfHO sequence detected by mass spectrometry.

Figure supplement 2. RT-qPCR analysis of endogenous PfHO transcript levels ±aTC in PfHO-aptamer/TetR-DOZI parasites complemented with PfHO episomes.

Figure supplement 3. Western blot of episomal PfHO expression in PfHO-aptamer/TetR-DOZI parasites.

Figure supplement 4. Sequence alignment of alveolate HO-like proteins indicating α-helical structure.

Source data 1. Uncropped western blots of parasites endogenously expressing PfHO-HA_2 and *E.coli* expressing PfHO HO-like domain ($PfHO^{84-305}$-HA_2).

Source data 2. Uncropped western blot of episomal PfHO expression in PfHO-aptamer/TetR-DOZI parasites.

PfHO associates with the apicoplast genome and mediates apicoplast gene expression. HO enzymes associate with a range of protein-interaction partners that depend on the organism and functional context. Known HO interactors include ferredoxin in plants and bacteria[25,30], cytochrome P450 reductase in mammals[12,31], and direct or indirect interactions with transcription factors that impact nuclear gene expression in mammals[53–55]. To identify protein-interaction partners of PfHO in parasites that might give insight into its essential role in apicoplast biogenesis, we used anti-HA immunoprecipitation (IP) to isolate endogenous PfHO-HA_2 from parasites. Co-purifying proteins were identified by tryptic digest and tandem mass spectrometry (MS), then compared to protein interactors identified in negative-control samples containing HA-tagged mitochondrial proteins mACP[56] or cyt *c*[57] to filter out non-specific interactions. In two independent experiments, 509 proteins co-purified with PfHO but were not detected in pulldowns of either mitochondrial control (**Figure 5 – figure supplement 1**). These PfHO-specific interactors included a range of cellular proteins, including proteins targeted to the apicoplast.

Because our microscopy and biochemical studies indicated exclusive PfHO localization to the apicoplast, we focused our analysis on co-purifying proteins that were known to localize to this organelle from prior IP/MS studies[37,58] (**Figure 5 – figure supplement 2**). Of the 65 apicoplast-targeted proteins, 37 had annotated functions, and the majority were associated with nucleic acid metabolism (e.g. GyrA/B, PREX, RAP, PKII) or protein translation (e.g., EF-G/Tu/Ts, RPS1, RPL15) pathways (**Figure 5A and Figure 5 – figure supplement 3**). The most highly enriched PfHO-specific interactor in both IP/MS experiments was an unannotated protein (Pf3D7_1025300) that contains a putative aspartyl protease domain and shows distant structural similarity to DNA damage-inducible protein (Ddi-1, P40087) – a ubiquitin-dependent protease associated with transcription factor processing[59–61] (**Figure 5 – figure supplement 2**). These putative interactors are consistent with reports of non-canonical HO roles in gene expression[62–64], retention by mature PfHO of an electropositive N-terminus favorable for interacting with nucleic acids (**Figure 4B**), and apparent PfHO localization to the membrane periphery of the apicoplast lumen (**Figure**

3B) where the apicoplast genome, DNA replication factors, and ribosomes associate[65–67]. We thus considered it most likely that PfHO had an essential function in either apicoplast genome replication or DNA-dependent gene expression.

To test the capability of PfHO to associate with the apicoplast genome, we leveraged an anti-GFP chromatin IP (ChIP) assay[68,69] in parasites episomally expressing the GFP-tagged PfHO constructs tested in **Figure 4C**, or ACP_L-GFP as a negative control. We attempted to PCR or qPCR amplify multiple nuclear- and apicoplast-encoded genes in purified ChIP and input samples that had been sonicated to shear DNA into fragments ≤2-kb in size prior to IP (**Figure 5- figure supplement 4**). Target nuclear and apicoplast genes were both successfully amplified in all input samples. However, only the anti-GFP pulldown from parasites expressing full-length PfHO-GFP showed robust amplification of an apicoplast- but not nuclear-encoded gene (**Figure 5B and Figure 5 – figure supplements 5 and 6A**). Although the portion of the PfHO N-terminus retained in mature PfHO has substantial electropositive character (**Figure 1A and Figure 1B**) favorable for association with DNA, this sequence in the $PfHO^{1-83}$-GFP construct was not sufficient for stable pull-down of apicoplast DNA. A faint amplicon for apicoplast DNA was detected for ACP_L-$PfHO^{84-305}$-GFP, but this signal was >4-fold weaker than observed for full-length PHO (**Figure 5B and Figure 5 – figure supplements 5 and 6A**). Based on these observations, we conclude that PfHO associates with the apicoplast genome and that DNA-binding requires both the cognate N-terminus and HO-like domain.

HO proteins in other species are reported to bind nuclear DNA[53], but the sequence features and nature of those associations are unclear. We note that our ChIP-PCR experiments cannot distinguish whether PfHO pull-down with the apicoplast genome reflects direct association with DNA and/or indirect interactions mediated by other proteins. Nevertheless, the unique sequence features of the PfHO N-terminus and its requirement for DNA association may suggest a *Plasmodium*-specific mechanism of DNA interaction that differs from other organisms. Selective interaction of full-length PfHO with the apicoplast genome was independent of the target gene amplified by PCR (**Figure 5 – figure supplement 5**) or qPCR

and persisted in the absence of crosslinking (**Figure 5 – figure supplement 6**). Our observation that 12 distinct genes spanning the apicoplast genome show similar amplification in sheared PfHO ChIP samples (**Figure 5 – figure supplements 5 and 6**) suggests that PfHO broadly interacts with apicoplast DNA in a sequence-independent manner akin to DNA topology regulators, gyrases, ligases, and single-strand stabilizing proteins[70–72], which our IP/MS data suggest are key interactors of PfHO (see discussion below).

Our observation that full-length PfHO, containing the cognate N-terminus and HO-like domain, was concordantly required for both DNA binding (**Figure 5B**) and essential function (**Figure 4C**) suggested most simply that association with the apicoplast genome was critical to PfHO function. To test possible roles for PfHO in DNA replication and/or RNA expression, we synchronized parasites to a 5-hour window and determined the impact of PfHO knockdown on DNA and RNA abundance by qPCR and RT-qPCR, respectively, in the first and second cycles after aTC washout but before apicoplast loss and parasite death. Parasites were grown in the presence of 200 µM IPP to decouple cellular viability from apicoplast-specific defects. We observed that PfHO knockdown in -aTC conditions caused a modest ~20% decrease in apicoplast DNA levels in second-cycle parasites relative to +aTC conditions (**Figure 5C**). In contrast, apicoplast RNA levels were strongly reduced upon PfHO knockdown, with a 30% reduction observed in the first cycle and nearly 90% reduction in the second cycle after aTC washout (**Figure 5D**). This PfHO-dependent reduction in RNA abundance was observed for all tested protein-coding and non-coding apicoplast genes spanning all of the currently known or predicted polycistronic apicoplast transcripts (**Figure 5 – figure supplement 7**)[73–76]. In contrast to its impact on apicoplast RNA, PfHO knockdown had no measurable impact on RNA transcript abundance for nuclear or mitochondrial genes (**Figure 5 – figure supplement 7**).

To dissect the time-course of this apicoplast-specific defect in RNA abundance, we collected samples from tightly synchronized parasites throughout the first and second growth cycles after aTC washout. In +aTC conditions, apicoplast RNA levels peaked around 36 hours for most genes, consistent

with prior studies of apicoplast transcription[77–79]. In -aTC conditions, there was a modest decrease in RNA transcript levels in the first cycle but complete failure to increase RNA abundance in the second cycle (**Figure 5E and Figure 5 – figure supplement 8**). We conclude that PfHO function is essential for apicoplast gene expression and that PfHO knockdown results in a specific defect in RNA abundance that underpins higher-order defects in apicoplast biogenesis that lead to parasite death (**Figure 6**).

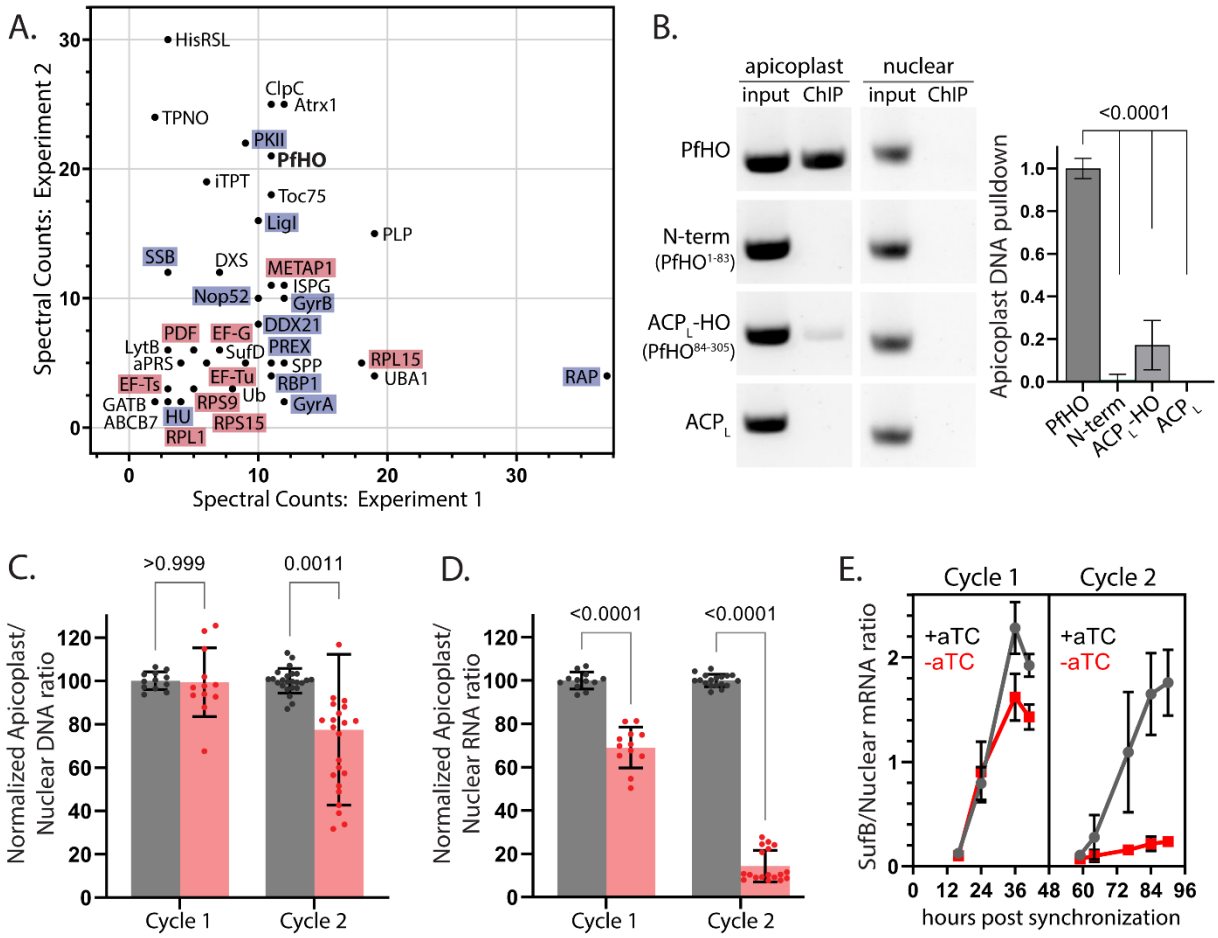

Figure 5: PfHO interactions with proteins and DNA and impacts of its knockdown on apicoplast DNA and RNA levels. A) Spectral counts of functionally annotated, apicoplast-targeted proteins detected in two independent anti-HA IP/MS experiments on endogenously tagged PfHO-HA_2. The names of proteins in DNA/RNA metabolism are highlighted blue and proteins in translation are highlighted in red. A list of all detected proteins can be found in Source Data 1. B) Representative image showing PCR amplification of nuclear-encoded (apicoplast ACP: Pf3D7_0208500) and apicoplast-encoded (SufB: Pf3D7_API04700) genes from DNA co-purified with full-length PfHO-GFP, $PfHO^{1-83}$-GFP, ACP_L-$PfHO^{84-305}$-GFP, or ACP_L-GFP by αGFP ChIP. "Input" is total parasite DNA collected after parasite lysis and sonication, and "ChIP" is DNA eluted after αGFP IP. Densitometry quantification of 3 biological replicates is plotted on right. Statistical significance of differences between PfHO and each other construct was calculated by Student's *t*-tests. C) Quantitative PCR analysis of DNA isolated from tightly synchronized PfHO-aptamer/TetR-DOZI parasites grown ±1 µM aTC with 200 µM IPP and harvested at 36 and 84 hours in biological triplicates, with normalization of Ct values averaged from three apicoplast genes (SufB, TufA, ClpM) to Ct values averaged from three nuclear (STL, I5P, ADSL) genes. Grey bars represent +aTC and red bars represent –aTC, and observed ratios are displayed as percentages. D) Quantitative RT-PCR on RNA isolated from the same parasites as in panel C to determine the normalized ratio of apicoplast transcripts (SufB, TufA, ClpM) relative to nuclear (STL, I5P, ADSL) transcripts. Significance of ±aTC differences for C and D were analyzed by Student's *t*-test. E) Representative time-course showing Ct values of SufB normalized to three nuclear (STL, I5P, ADSL) genes at indicated time in PfHO-aptamer/TetR-DOZI parasites grown ±1 µM aTC with 200 µM IPP. Data points are the average ±SD of biological triplicates.

Figure supplement 1. Spectral counts for proteins co-purified with PfHO in IP/MS experiments.

Figure supplement 2. List of apicoplast-localized proteins that co-purified with PfHO in IP/MS experiments.

Figure supplement 3. Functional pathway predictions for apicoplast-localized proteins that co-purified with PfHO in IP/MS experiments.

Figure supplement 4. Fragment analyzer quantification of parasite DNA fragment size after shearing.

Figure supplement 5. Steady-state PCR amplification of additional nuclear and apicoplast genes from DNA co-purified with indicated PfHO constructs.

Figure supplement 6. Additional ChIP experiments in parasites with GFP-tagged PfHO constructs.

Figure supplement 7. RT-qPCR of additional apicoplast genes in PfHO-aptamer/TetR-DOZI parasites grown for 3 days ±1 µM aTC with 200 µM IPP.

Figure supplement 8. Representative time-course of ClpM: nuclear transcript levels in synchronous PfHO-aptamer/TetR-DOZI parasites grown ±1 µM aTC with 200 µM IPP.

Source data 1. Table of proteins identified in PfHO IP/MS experiments.

Source data 2. Uncropped PCR gel of PfHO ChIP experiments in parasites with GFP-tagged PfHO constructs

Source data 3. Uncropped PCR gel of PfHO ChIP experiments ±crosslinking

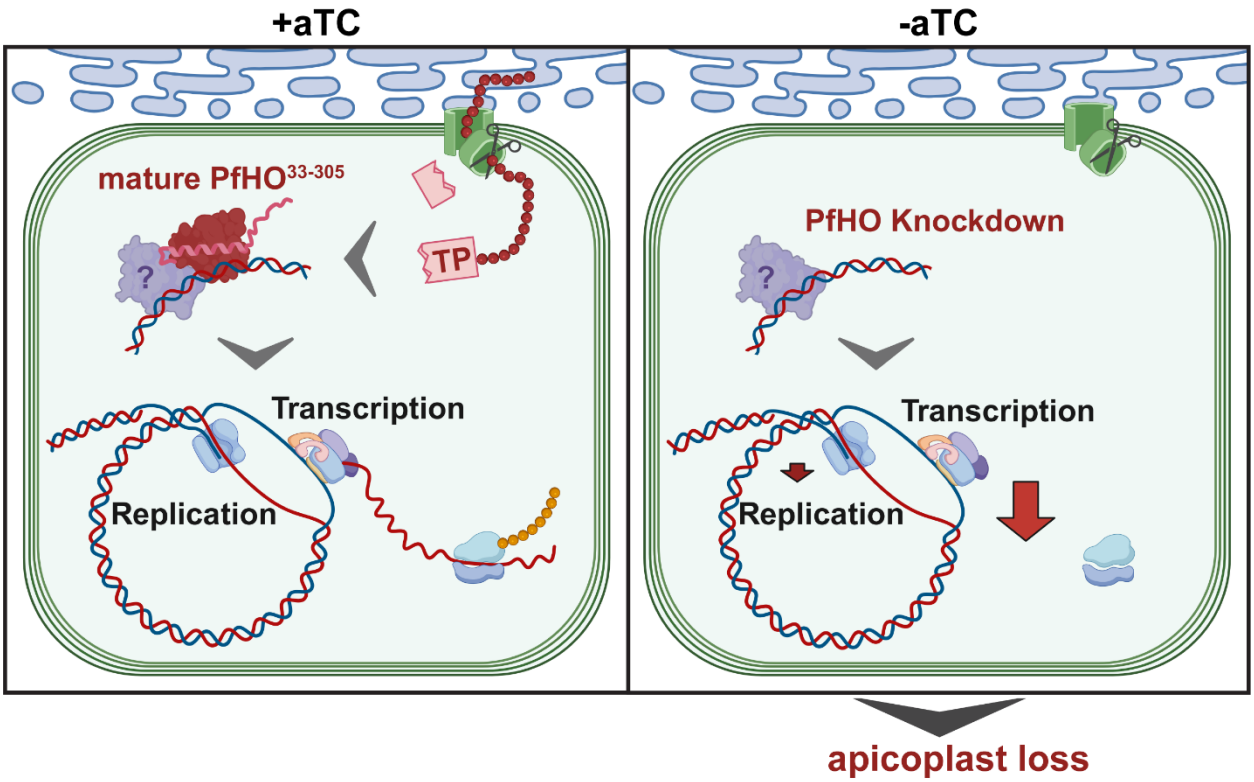

Figure 6: Model for essential PfHO function in apicoplast genome expression and organelle biogenesis. TP = transit peptide. Scissors represent proteolytic processing of PfHO N-terminus upon apicoplast import.

Supplementary file 1. Table of PCR primers.

Supplementary file 2. Table of reagents

DISCUSSION:

Heme metabolism is a central cellular feature and critical therapeutic vulnerability of blood-stage malaria parasites, which have evolved unusual molecular adaptations to survive and grow within heme-rich red blood cells. Hemozoin is the dominant fate of labile heme released from large-scale hemoglobin digestion. Nevertheless, malaria parasites express a divergent and inactive heme oxygenase-like protein, whose cellular function underpinning its evolutionary retention has remained mysterious. We have elucidated an essential role for PfHO within the apicoplast organelle of *P. falciparum*, where it associates with the apicoplast genome and nucleic acid metabolism enzymes and is required for organelle gene expression and apicoplast biogenesis.

Molecular function of PfHO. Our study unveils that *P. falciparum* parasites have repurposed the HO scaffold from its canonical role in heme degradation towards a divergent function required for expression of the apicoplast genome. This essential function appears to involve direct and/or indirect association with both the apicoplast genome and a variety of DNA/RNA-metabolism enzymes. Also, both the cognate N-terminal leader sequence, most of which remains attached in the mature protein, and the HO-like domain are required for function. We hypothesize that the electropositive N-terminus (**Figures 1A and 5B**) may mediate direct association with the apicoplast genome, while an electronegative face on the HO-like domain opposite the heme-binding region (**Figure 1 – figure supplement 5**) may interact with other DNA-binding proteins (e.g., gyrases and helicases) which co-purified with PfHO in IP/MS studies (**Figure 6**).

The specific molecular function of PfHO that impacts RNA transcript levels in the apicoplast remains to be defined, along with the broader prokaryotic-like biochemical processes that enable transcription in the apicoplast. The apicoplast genome is organized into two polycistronic operons that each consist of roughly half the genome, orient in opposite directions, and contain duplicated rRNA genes

at their 5' ends[76]. No promotor sequences have been identified in the apicoplast genome, but detection of transcripts up to 15 kb[73] and studies on mRNA processing sites[74] suggest that full polycistronic operons are transcribed and undergo "punctuation processing" at tRNAs distributed throughout transcripts[80,81]. The primary subunits of a prokaryotic-like RNA polymerase complex have been identified in *Plasmodium*. Although associated sigma factors and other interacting proteins are proposed to exist, they have thus far remained difficult to identify[73,75]. We initially considered a model whereby PfHO might function as a sigma factor-like adaptor that directly binds to the multi-subunit prokaryotic RNA polymerase to mediate genomic association and transcription initiation. However, none of the core RNA polymerase subunits co-purified with PfHO in our IP/MS studies, suggesting that such a function may be unlikely.

Based on PfHO association with a variety of DNA-binding proteins and topology regulators, we consider it more likely that PfHO functions in association with other effector proteins to regulate and optimize DNA topology to enable transcriptional activity. The apicoplast-targeted gyrase A, gyrase B, DDX21 DEAD-box helicase, ligase I, the helicase domain of PREX, histone-like protein (HU)[82], and single-strand DNA binding protein[71] all co-purify with PfHO in our IP/MS experiments (**Figure 5A**). Of these proteins, DNA gyrase A[83], gyrase B[84], PREX[85], and HU[86] have been directly tested as essential apicoplast biogenesis factors in *Plasmodium* parasites. The relationship of most of these proteins with apicoplast transcription is unknown, but their activity in other organisms may shed light on a functional pathway in *Plasmodium*. Prokaryotic transcription is blocked by chemical or genetic disruption of DNA gyrase[87–89], a hetero-tetramer of gyrase A and B proteins[90]. DNA gyrase-induced negative supercoiling locally unwinds circular DNA molecules[89] to facilitate transcriptional initiation by RNA polymerase complexes[87,91]. DNA gyrase also relieves torsional stress formed by the procession of RNA polymerase complexes along DNA molecules and prevents stalling during transcription of long, polycistronic operons[92,93]. Additionally, HU coordinates prokaryotic DNA structure and supercoiling in conjunction with DNA gyrase and has been reported to regulate the spatial distribution of RNA polymerase and transcription levels in *E. coli*[94,95].

Although these proteins have exclusively been associated with apicoplast DNA replication in *Plasmodium*, regulation of DNA supercoiling is also a major mechanism of prokaryotic transcriptional control[92,96]. This biological property may have been present in ancestral plastids and inherited by the prokaryotic-like *Plasmodium* apicoplast.

We also noted that RNA processing and translation-associated proteins co-purified with PfHO, including ribosomal RNA (rRNA) and transfer RNA (tRNA) maturation proteins, elongation factors, and ribosomal protein subunits (**Figure 5A**). RNA metabolism in the *Plasmodium* apicoplast is sparsely understood. No RNA-degrading enzymes have been identified, and the specific functions of RNA-binding proteins remain unknown. DEAD-box DNA/RNA helicases such as DDX21 have been implicated in the removal of aberrant R-loops (DNA/RNA hybrids) during RNA transcription[97–99], but *Plasmodium* DDX21 has also been implicated with rRNA maturation in ribosome biogenesis[37]. Other RNA-binding proteins that co-purified with PfHO, Nop52 and RAP, also show low-level sequence homology to ribosome assembly factors[100,101]. Prokaryotic ribosome assembly is a co-transcriptional process regulated by, and in close proximity to RNA transcriptional machinery[102–104]. Apicoplast ribosome assembly is poorly studied but appears to be similar to prokaryotic systems. Indeed, a prior IP/MS study reported that apicoplast ribosomes and ribosomal assembly complexes co-purified with RNA transcription complexes and DNA topology regulators[37]. PfHO pulldown with RNA-processing and protein-translation components may therefore reflect the underlying physical and temporal coupling of RNA transcription and protein translation in the apicoplast. It is also possible that PfHO contributes to other aspects of RNA metabolism that remain undefined.

Evolution of PfHO and its divergent function. Although PfHO retains the conserved α-helical structure of HO enzymes, it has strikingly low sequence similarity, implying substantial evolutionary distance from well-studied HO orthologs in humans, plants, and bacteria (**Figure 1 and Figure 1 – figure supplement 2)**.

What then is the evolutionary origin of PfHO and its non-canonical function? The *Plasmodium* apicoplast is thought to derive from secondary endosymbiosis through ancestral engulfment of a plastid-containing red algae that had previously engulfed a photosynthetic cyanobacterium[65,105–108]. Subsequent loss of photosynthesis accompanied the transition to intracellular parasitism by proto-apicomplexan ancestors[109,110]. HO enzymes are commonly found in photosynthetic cyanobacteria and eukaryotic chloroplasts, where they initiate biosynthesis of biliverdin and other bilin chromophores utilized in phytochrome proteins for light sensing and signaling[14,111,112]. Retention of PfHO in the *Plasmodium* apicoplast likely reflects the original presence of HO enzymes in the cyanobacterial ancestors of this organelle.

The transition from free-living algae to apicomplexan parasitism involved significant genome reduction, including loss of plastid photosynthesis and phytochrome biosynthesis pathways[110]. These functional reductions presumably removed the selective pressure to retain enzymatic HO activity. Indeed, the only identifiable HO homologs retained in Apicomplexa are found exclusively in hematozoan parasites such as *Plasmodium*, *Babesia*, and *Theileria*, and have lost the active-site His ligand like PfHO (**figure 1 – figure supplement 2**). Insights into the evolutionary origin of PfHO are provided by comparison to HO-like proteins in coral-symbiotic chromerid algae, the closest free-living and photosynthetic relatives to apicomplexan parasites[109,110]. *Vitrella brassicaformis* and *Chromera velia* both express multiple HO homologs thought to be remnants of prior endosymbioses[113]. These HO proteins segregate phylogenetically with either active metazoan, active plant, or inactive hematozoan HOs (**figure 1 – figure supplement 2**) featuring the retention or loss of the active-site His ligand, respectively. Similarly, *Arabidopsis thaliana* expresses four chloroplast-targeted HO homologs that include three active HO enzymes and the inactive AtHO2 that lacks the conserved His ligand but contributes to photomorphogenesis[14]. These observations support a model in which active HO homologs were lost along

with photosynthetic machinery during the transition to apicomplexan parasitism with the exclusive retention of an inactive HO-like homolog in Hematozoa.

It remains unclear why hematozoan but no other apicomplexan parasites retained an inactive HO-like homolog. The common infection of heme-rich RBCs by hematozoans may suggest that remnant heme- or porphyrin-binding activity[8] may play a role in functional regulation of these HO-like proteins within the apicoplast. Indeed, apicoplast transcription[78], heme released by hemoglobin digestion[114], and PfHO expression (**Figure 3- figure supplement 5**) all peak coincidentally around 30 hours post-infection. The affinity of PfHO for heme (K_d ~8 μM)[8] is also notably similar to the ~2 μM concentration of labile heme estimated in the parasite cytoplasm[115]. Future studies can test the intriguing hypothesis that labile heme levels sensed by PfHO in the apicoplast tune functional interactions by PfHO that regulate apicoplast gene expression.

Although PfHO has diverged from canonical HO function, it retains many structural and biochemical features present in metazoan HOs which are reported to mediate transcription factor activity independent of heme degradation[15–17,53,116]. Thus, a role for PfHO in gene expression may be an ancient functional property of the HO scaffold that was further expanded and honed by parasites after heme-degrading activity was lost. In this regard, PfHO may be conceptually similar to other parasite proteins (e.g., mitochondrial acyl carrier protein[56]) that have lost canonical function but whose retention of an essential role unveils a latent secondary activity that was previously un- or under-appreciated in the shadow of the dominant primary function in well-studied orthologs from other organisms.

Implications for expanded functions of N-terminal pre-sequences beyond organelle targeting. Our discovery that PfHO requires a portion of its N-terminal transit peptide for essential function within the apicoplast expands the molecular paradigm for understanding the evolution and function of organelle-targeting leader sequences. PfHO homologs in *Vitrella* and *Chromera* also contain a predicted α-helix in

their N-terminal sequences that differ from chloroplast-targeting HOs in plants (**figure 4 – figure supplement 4**). This unique α-helix predicted in alveolate HO-like proteins adds positive-charge to the HO-like protein that we propose mediates interaction with DNA. It is possible that the alveolate ancestors of *Plasmodium* expanded and functionally repurposed the targeting sequences of other plastid and/or mitochondrial proteins to provide unique organelle-specific functions that remain to be discovered. The recent report that *Toxoplasma gondii* parasites repurpose the cleaved leader sequence of mitochondrial cyt c_1 as a stable subunit of ATP synthase supports this view[117,118]. Identifying adaptations in *P. falciparum* that diverge from human host cells can reveal novel parasite vulnerabilities that underpin the development of new therapeutic strategies.

MATERIALS AND METHODS:

Sequence homology searches and phylogenetic analyses.

We acquired *Plasmodium* and alveolate protein sequences from VEuPathDB.org[119] and all other protein sequences from UniProt.org[120] databases. The protein sequence for PfHO (Pf3D7_1011900) was analyzed by NCBI Protein BLAST[19] and HMMER[20] with the exclusion of *Plasmodium* or apicomplexan organisms to identify putative orthologs. Orthologous protein sequences and select reference HO proteins were aligned via Clustal Omega[121] and analyzed using Jalview[122]. The multi-sequence alignment was uploaded to the IQ-TREE webserver (http://iqtree.cibiv.univie.ac.at) with ultrafast bootstrap analysis. The resulting maximum likelihood phylogenetic tree from 1000 bootstrap alignments was analyzed and displayed using FigTree (http://tree.bio.ed.ac.uk/software/figtree/).

Recombinant protein expression and purification for crystal structure determination.

The gene encoding residues 84-305 of PfHO was cloned into a pET21d expression vector (Novagen) using NcoI and XhoI sites, in frame with a C-terminal His_6 tag[8]. *E. coli* BL21 (DE3) cells transformed with this vector were grown in LB medium supplemented with ampicillin (50 µg/mL) (Sigma A9518) and protein expression was induced with 0.5 mM isopropyl β-D-1-thiogalactopyranoside (IPTG) (Sigma 16758) at an OD of 0.5, after which the cells were grown at 20 °C overnight. Cells were harvested by centrifugation (7,000 × *g*, 10 min), the pellet was resuspended in binding buffer (20 mM Tris-HCl, 500 mM NaCl, 20 mM imidazole, pH 8.5), and the cells were lysed by sonication. The cell lysate was cleared by centrifugation (40,000×g, 30 min), and the supernatant was subjected to immobilized metal affinity chromatography using a 1 mL Ni-NTA agarose column (Qiagen, 30210) equilibrated with binding buffer. The protein was eluted with a buffer containing 20 mM Tris-HCl, 500 mM NaCl, and 300 mM imidazole at pH 8.5. The eluted protein was further purified by size-exclusion chromatography employing a 26/60 Superdex75 column equilibrated with a buffer containing 20 mM HEPES and 300 mM NaCl at pH 7.5. To

produce the protein containing SeMet, *E. coli* B834 (DE3) cells transformed with the same plasmid as above were grown in minimal media (2 g L^{-1} NH_4Cl, 6 g L^{-1} KH_2PO_4, 17g L^{-1} $Na_2HPO_4 \cdot 12H_2O$, 1 g L^{-1} NaCl, 1.6 mg L^{-1} $FeCl_3$, 0.5 g L^{-1} $MgSO_4 \cdot 7H_2O$, 22 mg L^{-1} $CaCl_2 \cdot 6H_2O$, 4 g L^{-1} Glucose, and 50 mg L^{-1} L-SeMet). Purification was identical to that of the WT protein. Protein purity was confirmed by observation of a single band at the appropriate molecular mass by Coomassie-stained SDS-PAGE.

Protein crystallization.

Protein in a buffer containing 20 mM HEPES and 300 mM NaCl at pH 7.5 was subjected to crystallization trials using sitting-drop vapour diffusion using commercially available screening kits form Hampton Research in an Oryx8 system (Douglas Instruments). Protein (0.5 μL at 9.5 mg mL^{-1}) was mixed with an equal volume of reservoir solution, and crystallization plates were maintained at 20 °C for several weeks while being examined. The crystallization solutions producing the best crystals were optimized using hanging-drop geometry in 24-well plates by mixing manually 2 μL of protein solution (5.0 mg mL^{-1}) and an equal volume of reservoir solution. The best crystals appeared in a few days in a reservoir solution containing 0.4 M $(NH_4)_2SO_4$, 0.65 M Li_2SO_4, and 0.1 M sodium citrate tribasic dihydrate at pH 5.6 and a temperature of 20 °C. Single crystals were mounted in nylon Cryo-Loops (Hampton Research, HR4-932) coated with Paratone (Hampton Research, HR2-862) and directly transferred to liquid nitrogen for storage.

Structural data collection and processing.

Diffraction data from single crystals of WT and SeMet protein were collected in beamlines AR-NW12A and BL5A, respectively, at the Photon Factory (Tsukuba, Japan) under cryogenic conditions (100 K). Diffraction images were processed with the program MOSFLM and merged and scaled with the program SCALA or AIMLESS of the CCP4 suite. The structure of the SeMet protein was solved by the

method of single anomalous diffraction using the Autosol module included in the PHENIX suite. The structure of the WT protein was determined by the molecular replacement method using the coordinates of the SeMet protein from above with the program PHASER. The models were refined with the programs REFMAC5 and built manually with COOT. Validation was carried out with PROCHECK. Data collection and structure refinement statistics are given in **Figure 1 – figure supplement 3**. The final structural coordinates and structure factors were deposited as RCSB Protein Data Bank entry 8ZLD.

Structural visualization and analyses.

A predicted structural model for PfHO (Pf3D7_1011900) was acquired from the AlphaFold Protein Structure Database (https://alphafold.ebi.ac.uk), and published HO structures were acquired from the RCSB Protein Data Bank (https://www.rcsb.org). The AlphaFold structural model, PfHO crystal structure, and HO structures were visualized and analyzed using The PyMOL Molecular Graphics System, Version 2.5, Schrödinger, LLC. Structural superpositions were performed with the PyMOL integrated command "align" and assessed by the total number of atoms aligned and RMSD (Å). We uploaded PDB files of PfHO crystal structure and AlphaFold model to the DALI protein structural comparison server (http://ekhidna2.biocenter.helsinki.fi/dali) to identify proteins structurally related to PfHO. To determine surface charge of structures, we uploaded PDB files to APBS-PDB2PQR online software suite (https://server.poissonboltzmann.org/)[123], and displayed the calculated Poisson-Boltzmann surface charge using the PyMOL APBS tool 2.1 plugin.

Parasite culturing and transfection.

Plasmodium falciparum Dd2[124] or 3D7[42] parasites were cultured in human erythrocytes obtained from Barnes-Jewish Hospital (St. Louis, MO) or the University of Utah Hospital blood bank (Salt Lake City, UT) in RPMI-1640 medium (Thermo Fisher, 23400021) supplemented with 2.5 g/L Albumax I Lipid-Rich

BSA (Thermo Fisher, 11020039), 15 mg/L hypoxanthine (Sigma, H9636), 110 mg/L sodium pyruvate (Sigma, P5280), 1.19 g/L HEPES (Sigma, H4034), 2.52 g/L sodium bicarbonate (Sigma, S5761), 2 g/L glucose (Sigma, G7021), and 10 mg/L gentamicin (Invitrogen, 15750060), as previously described[49]. Parasites were maintained at 37˚ C in 90% N_2/5% CO_2/5% O_2 or in 5% CO_2/95% air. For drug-induced apicoplast-disruption experiments, parasites were cultured for ~7 days in 1 µM doxycycline (Sigma, D9891) and 200 µM isopentenyl pyrophosphate (Isoprenoids, IPP001).

Transfections were performed in 1x cytomix containing 50-100 µg DNA by electroporation of parasite-infected RBCs in 0.2 cm cuvetes using a Bio-Rad Gene Pulser Xcell system (0.31 kV, 925 µF). Transgenic parasites were selected based on plasmid resistance cassettes encoding human DHFR[125], yeast DHOD[126], or blasticidin-S deaminase[127] and cultured in 5 nM WR99210 (Jacobus Pharmaceutical Co.), 2 µM DSM1 (Sigma, 53330401), or 6 µM blasticidin-S (Invitrogen, R21001), respectively. After stable transfection and selection, parasites were grown in the continual presence of selection drugs, and aptamer-tagged parasites were grown in 0.5-1 µM anhydrotetrocycline (Cayman Chemicals, 10009542).

Parasite growth assays.

Parasites were synchronized to the ring stage with an estimated 10-15-hour synchrony window by treatment with 5% D-sorbitol (Sigma, S7900). For aptamer-based knockdown experiments, aTC was washed out during synchronization with additional 3-5 washes in media and/or PBS. Parasite growth was monitored by plating synchronized parasites at ~1% parasitemia and allowing culture expansion over several days with daily media changes. Parasitemia was monitored daily by flow cytometry by diluting 10 µL of each parasite culture well from each of three biological replicate samples into 200 µL of 1.0 µg/mL acridine orange (Invitrogen, A3568) in phosphate buffered saline (PBS) then analyzed on a BD FACSCelesta flow cytometry system monitoring SSC-A, FSC-A, PE-A, FITC-A, and PerCP-Cy5-5-A channels.

Cloning and episomal expression of PfHO variants in parasites.

The genes encoding PfHO (Pf3D7_1011900) and apicoplast ACP (Pf3D7_0208500) were PCR amplified from *P. falciparum* strain 3D7 cDNA using primers with ≥20 bp homology overhangs (primers 10-15) for ligation-independent insertion into the XhoI and AvrII sites of pTEOE (human DHFR selection cassette) in frame with a C-terminal GFP tag, and with expression driven by HSP86 promoter[128]. Correct plasmid sequences were confirmed by Sanger sequencing, and plasmids were transfected as described above in combination with 25 µg pHTH plasmid containing piggyBac transposase to drive stable, random integration into the parasite genome[129].

Parasite genome editing to enable ligand-dependent regulation of PfHO expression.

We first used restriction endonuclease-mediated integration[39] and single-crossover homologous recombination to tag the PfHO gene to encode a C-terminal GFP-tag fused to the DHFR-destabilization domain[40,41] and a single hemagglutinin (HA) tag in 3D7 (PM1 KO)[42] parasites. PCR primers 18 and 19 were used to clone the 3' 1kb DNA sequence of the PfHO gene into the XhoI and AvrII sites of the pGDB vector[40] to serve as a homology region for integration. 50 µg of this plasmid along with 50 units of MfeI restriction enzyme (NEB R3589), which cuts at a single site within the PfHO gene just upstream of the homologous sequence cloned into the donor-repair pGDB plasmid, was transfected into 3D7 PM1 KO parasites[42] (which express human DHFR), as described above. Parasites were positively selected with blasticidin-S in the continuous presence of trimethoprim (Sigma, T7883), cloned by limiting dilution, and genotyped by Southern blot (**Figure 3- figure supplement 1**). Conditional knockdown was evaluated by washing synchronized parasites 3-5x in PBS to remove trimethoprim.

We next used CRISPR/Cas9 and single-crossover homologous recombination to tag the PfHO gene to encode a C-terminal HA_2 tag fused to the glmS ribozyme[43,44] in Dd2 parasites. The 1 kb homology

sequence or PfHO was excised from pGDB and sub-cloned by ligation into a modified pPM2GT vector[130] in which the linker-GFP sequence between the AvrII and EagI sites was replaced with a HA-HA tag and stop codon followed by the 166 bp glmS ribozyme[43,44]. QuikChange II site-directed mutagenesis (Agilent Technologies) was used with primers 20 and 21 to introduce silent shield mutations into the PfHO homology region for purposes of CRISPR/Cas9-based genome editing, such that the AGATGG sequence in the most 3' exon was changed to CGGTGG. A guide RNA sequence corresponding to TGAGTAGGAAATGGAGTAGA was cloned into a modified version of the previously published pAIO CRISPR/Cas9 vector[131] in which the BtgZI site was replaced with a unique HindIII site to facilitate cloning[49]. 50 µg each of the pPM2GT and pAIO vectors were transfected into Dd2 parasites, as described above. Parasites were positively selected by WR99210, cloned by limiting dilution, and genotyped by PCR (**Figure 3 – figure supplement 1**). Conditional knockdown was evaluated by adding 0-10 mM glucosamine (Sigma, G1514) to synchronized parasite cultures and evaluating protein expression and parasite growth relative to untagged parental Dd2 parasites.

CRISPR/Cas9 and double-crossover homologous recombination was used to tag the PfHO gene to encode a single RNA aptamer at the 5' end and a 10x aptamer cassette at the 3' end for inducible knockdown with the aptamer/TetR-DOZI system[46,47]. A donor plasmid was created by ligation-independent insertion of a synthetic gene (gBlock, IDT) containing PfHO cDNA (*T. gondii* codon bias) into the linear pSN1847L vector[46], along with PCR amplified (primers 22-25) left and right homology flanks corresponding to the 5' (426 bp immediately upstream of start codon) and 3' (455 bp starting at position 47 after the TAA stop codon) untranslated regions of PfHO. Because the aptamer sequence contains two ATG motifs that can serve as alternate translation start sites, a viral 2A peptide sequence was introduced between the 5' aptamer sequence and the start ATG of PfHO. This donor repair plasmid (50 µg) and the pAIO CRISPR/Cas9 vector (50 µg) with guide sequence TGAGTAGGAAATGGAGTAGA targeting the 3' end of the endogenous PfHO gene was transfected into Dd2 parasites, as described above. No shield mutation

in the donor plasmid was required due to the altered codon bias of the synthetic PfHO cDNA in that vector. Parasites were positively selected with blasticidin-S in the presence of 1 µM aTC. Integration was confirmed by Southern blot and PCR (**Figure 3 – figure supplement 4**). No evidence of remnant WT locus was detected in polyclonal transfectants, which were used for most experiments. Parasites were also cloned by limiting dilution.

Microscopy.

Live microscopy of parasites expressing GFP-tagged proteins was performed by staining mitochondria with 25 nM MitotrackerRed CMXRos (Invitrogen, M7512) for 30 minutes and staining nuclei with 5 µg/mL Hoechst 33342 (Invitrogen, H3570) for 5-10 minutes in PBS. Stained parasites were then imaged in PBS under a coverslip on an Invitrogen EVOS M5000. Images were adjusted for brightness and contrast in FIJI with linear variations equally applied across images. Signal intensity profiles were calculated for the red and green channels respectively using the FIJI plot profile tool along a single line that transects the region of highest signal for both channels (identified on images as white line).

For immunofluorescence (IFA) experiments, parasitized red blood cells were fixed in 4% paraformaldehyde and 0.0016% glutaraldehyde for 30 minutes at 25°C, then deposited onto poly-D-lysine coated coverslips. Fixed cells were permeabilized in PBS supplemented with 0.1% Triton-X100, reduced in 0.1 mg/mL $NaBH_4$, and blocked in 3% BSA for 30 minutes. Parasites were stained with primary antibodies: mouse anti-GFP (Invitrogen, A-11120), and rabbit anti-apicoplast ACP[132] at 1:100 dilution in 1% BSA for 1 hour at 25°C, washed thrice in PBS-T (PBS with 0.1% Tween-20), stained with secondary antibodies: goat anti-mouse AF488 (Invitrogen, A-11001) and goat anti-rabbit AF647 (Invitrogen, A21244) in 1% BSA for 1 hour at 25°C, and washed thrice in PBS-T before imaging. Coverslips were mounted onto slides using ProLong Diamond Antifade Mountant with DAPI (Invitrogen, P36971) overnight at 25°C, then imaged on an Axio Imager M1 epifluorescence microscope (Carl Zeiss Microimaging Inc.) equipped with a

Hamamatsu ORCA-ER digital CCD camera. Images were adjusted for brightness and contrast in FIJI with linear variations equally applied across images. Pearson correlation was automatically calculated with the FIJI Coloc2 tool on unmasked images using a point spread function of 3 pixels and 50 Costes iterations.

Immunogold transmission electron microscopy was performed (Dr. Wandy Beatty, Washington University in St. Louis) as previously described[133] using endogenously tagged PfHO-GFP-DHFR$_{DD}$ 3D7 parasites and staining with goat anti-GFP (Abcam, ab5450) and rabbit anti-apicoplast ACP[134] antibodies along with gold-conjugated anti-goat and anti-rabbit secondary antibodies.

Production and validation of custom anti-PfHO rabbit antibody.

The HO domain of PfHO (84-305) was cloned into pET28 with an N-terminal His-tag and start codon, purified by Ni-NTA, cleaved by thrombin, and purified by FPLC as previously reported[8]. Purified protein was then injected into a rabbit for polyclonal Ab production by Cocalico Biologicals Inc. (https://www.cocalicobiologicals.com) following their standard protocol. Rabbit serum was validated for specific detection of PfHO in parasite lysates and with recombinant protein expressed in bacteria prior to use (**Figure 3 – figure supplement 5**).

SDS-PAGE and western blots.

Parasite cultures were grown to ~10% parasitemia in 10 mL cultures for western blots and 50-100 mL cultures for immunoprecipitation. Parasites were released from red blood cells by treatment with 0.05% saponin and subsequently lysed by sonication (20 pulses 50% duty cycle, 50% power) on a Branson microtip sonicator in TBS lysis buffer (50mM Tris pH 7.4, 150 µM NaCl, 1% v/v Triton X-100) with protease inhibitors (Invitrogen, A32955) followed by incubation at 4°C for 1 hour. Recombinantly expressed protein was obtained for western blot analysis by inducing BL21 (DE3) *E. coli* grown to an OD of 0.5 in LB medium with 0.5 mM IPTG at 20 °C overnight. Cells were harvested by centrifugation (5,000 RPM, 10 min), and

lysed with the same methods described above. Lysates were clarified by centrifugation (14,000 RPM, 10 min) and quantified by Lowry colorimetry. 50 µg of total protein was mixed in SDS sample buffer, heated at 95C for 10 minutes, and separated by electrophoresis on 12% SDS-PAGE gels in Tris-HCl buffer. Proteins were transferred onto nitrocellulose membranes using the Bio-Rad wet-transfer system for 1 hour at 100 V, and blocked with 5% non-fat milk in TBS-T (50mM Tris pH 7.4, 150 µM NaCl, 0.5% v/v Tween-20). Membranes were stained with primary antibodies: goat anti-GFP (Abcam ab5450), rat anti-HA (Roche), mouse anti-hDHFR, rabbit anti-apicoplast ACP[132], custom rabbit anti-PfHO, or rabbit anti-EF1α[135] diluted 1:1000-1:2500 in blocking buffer for ≥ 18 hours at 4 °C. Samples were then washed thrice in TBS-T and stained with secondary antibodies: rabbit anti-Goat HRP (Santa Cruz, sc2768), goat anti-Rabbit HRP (Invitrogen, A27036), donkey anti-rabbit IRDye800CW (LiCor, 926-32213), donkey anti-rabbit IRDye680 (LiCor, 926-68023), or donkey anti-goat IRDye800CW (LiCor, 926-32214), diluted 1:10,000 in TBS-T for 1-2 hours at 25 °C, and again washed thrice before imaging. All blots stained with horseradish peroxidase (HRP) were developed 3 minutes with Prometheus™ ProSignal Femto ECL reagent (Genesee Scientific 20-302) and imaged on a BioRad ChemiDoc MP imaging system, and all blots stained with IRDye antibodies were imaged on a Licor Odyssey CLx system. Protein size was estimated by migration relative to the protein ladder using Licor Image Studio software v5.5.4.

N-terminal protein sequencing of PfHO.

A 170 mL culture of 3D7 parasites at 3% hematocrit and ~15% asynchronous parasitemia was harvested by centrifugation followed by release of parasites from RBCs in 5% saponin (Sigma S7900). The resulting parasite pellet was subsequently lysed in 1 mL RIPA buffer with sonication and clarified by centrifugation. PfHO was isolated by immunoprecipitation using 60 µl of affinity-purified custom anti-PfHO rabbit antibody and 400 µl of Protein A dynabeads (Invitrogen, 1001D). The beads were washed 3X in RIPA buffer, eluted with 110 µl 1X SDS sample buffer, fractionated by 10% SDS-PAGE, followed by

transfer to PVDF membrane and staining by Coomassie. The band corresponding to mature PfHO was excised and subjected to N-terminal sequencing by Edman degradation at the Stanford University Protein and Nucleic Acid Facility.

Immunoprecipitation.

Dd2 parasites expressing endogenously tagged PfHO with C-terminal HA-HA tag were harvested from ~75 mL of culture by centrifugation, released from RBCs by incubating in 0.05% saponin (Sigma 84510) in PBS for 5 minutes at room temperature, and pelleted by centrifugation (5000 rpm, 30 min, 4°C). Parasites were then lysed by sonication (20 pulses 50% duty cycle, 50% power) on a Branson microtip sonicator in TBS lysis buffer (50mM Tris pH 7.4, 150 µM NaCl, 1% v/v Triton X-100) with protease inhibitors (Invitrogen A32955) followed by incubation at 4°C for 1 hour and centrifugation (14,000 rpm, 10 min), The clarified lysates were mixed with equilibrated resin from 30 µl of Pierce anti-HA-tag magnetic beads (Invitrogen 88836) and incubated for 1 hour at 4°C on a rotator. Beads were placed on a magnetic stand, supernatants were removed by aspiration, and beads were washed thrice with cold TBS-T. Bound proteins were eluted with 100 µl of 8M urea (in 100 mM Tris-HCl at pH 8.8). Proteins were precipitated by adding 100% trichloroacetic acid (Sigma 76039) to a final concentration of 20% v/v and incubated on ice for 1 hour. Proteins were then pelleted by centrifugation (13,000 rpm, 25 min, 4°C) and washed once with 500 µl of cold acetone. The protein pellets were air-dried for 30 min and stored at −20°C.

Mass spectroscopy.

Protein samples isolated by anti-HA-tag IP of endogenous PfHO were reduced and alkylated using 5 mM Tris (2-carboxyethyl) phosphine and 10 mM iodoacetamide, respectively, and then enzymatically digested by sequential addition of trypsin and lys-C proteases, as previously described[136]. The digested peptides were desalted using Pierce C18 tips (Thermo Fisher Scientific), dried, and resuspended in 5% formic acid.

Approximately 1 µg of digested peptides was loaded onto a 25-cm-long, 75-µm inner diameter fused silica capillary packed in-house with bulk ReproSil-Pur 120 C18-AQ particles, as described previously[137]. The 140-min water-acetonitrile gradient was delivered using a Dionex Ultimate 3,000 ultra-high performance liquid chromatography system (Thermo Fisher Scientific) at a flow rate of 200 nl/min (Buffer A: water with 3% DMSO and 0.1% formic acid, and Buffer B: acetonitrile with 3% DMSO and 0.1% formic acid). Eluted peptides were ionized by the application of distal 2.2 kV and introduced into the Orbitrap Fusion Lumos mass spectrometer (Thermo Fisher Scientific) and analyzed by tandem mass spectrometry. Data were acquired using a Data-Dependent Acquisition method consisting of a full MS1 scan (resolution = 120,000) followed by sequential MS2 scans (resolution = 15,000) for the remainder of the 3-s cycle time. Data was analyzed using the Integrated Proteomics Pipeline 2 (Integrated Proteomics Applications, San Diego, CA). Data were searched against the protein database from P. falciparum 3D7 downloaded from UniprotKB (10,826 entries) on October 2013. Tandem mass spectrometry spectra were searched using the ProLuCID algorithm followed by filtering of peptide-to-spectrum matches by DTASelect using a decoy database-estimated false discovery rate of <1%. The proteomics data are deposited in the MassIVE data repository (https://massive.ucsd.edu) under the identifier MSV000094692.

Measuring apicoplast DNA and RNA abundance in parasites.

Highly synchronous parasites were obtained by sorbitol synchronization of high parasitemia cultures followed by magnet-purification of schizonts after 36-40 hours using MACS LD separation columns (Miltenyi, 130-042-901) with stringent washing. Purified schizonts were allowed to reinvade fresh RBCs for 5 hours on an orbital shaker at 100 rpm in media containing 1 µM aTC. Immediately prior to experimental plating, parasites were treated with sorbitol to ensure ≤5-hour synchrony window and washed 3-5 times in media and/or PBS to remove aTC. Times listed in growth assays are post-

synchronization and reflect T=0 at the time that magnet-purified schizonts were allowed to reinvade fresh RBCs.

Highly synchronous parasites were plated in 4 mL of either +aTC or -aTC media. Parasites to be harvested in the first life cycle were cultured at 3%, second cycle at 1%, and third cycle at 0.5% starting parasitemia. 4 mL of +aTC and -aTC cultures were collected for whole DNA and RNA extraction, respectively, at 36, 84, and 132 hours, snap frozen in liquid N_2, and stored at -80°C. Parasite DNA was extracted with a QIAamp DNA Blood Mini kit (Qiagen, 51106), and RNA was purified by Trizol (Invitrogen, 15596026) and phenol-chloroform isolation. We converted 1 µg of purified RNA to cDNA using a SuperScript IV VILO RT kit (Invitrogen, 11766050). Since apicoplast genes are extremely AT- rich[76] and mRNA transcripts are not poly-adenylated or poly-uridylylated[80], gene-specific reverse primers were used to prime the reverse transcription reactions. RT-qPCR was then used to assess the DNA/RNA abundance of four nuclear genes: STL (Pf3D7_0717700), I5P (Pf3D7_0802500), ADSL (Pf3D7_0206700), and PfHO (Pf3D7_1011900), one mitochondrial gene: CytB (Pf3D7_MIT02300), and twelve apicoplast genes: rpl-4 (Pf3D7_API01300), rpl-2 (Pf3D7_API01500), rpl-14 (Pf3D7_API02000), rps-12 (Pf3D7_API02700), EF-Tu (Pf3D7_API02900), ClpM (Pf3D7_API03600), RpoC2 (Pf3D7_API04200), RpoC1 (Pf3D7_API04300), RpoB (Pf3D7_API04400), SufB (Pf3D7_API04700), ls-rRNA (Pf3D7_API06700), and ss-rRNA (Pf3D7_API05700) (primers 28-61). Invitrogen Quantstudio Real-Time PCR systems were used to quantify abundance of DNA and cDNA using SYBR green dye and primers 28-61. The relative DNA or cDNA abundance of each apicoplast gene was normalized to the average of three nuclear-encoded genes for each sample, and -aTC was compared to +aTC by the comparative Ct method[138]. All qPCR experiments were performed in triplicate and data was analyzed by unpaired Student's t-test.

PfHO chromatin immunoprecipitation (ChIP) analysis

We saponin-released 75mL of high parasitemia Dd2 cultures transfected with episomes encoding expression of PfHO-GFP, PfHO$^{1-83}$-GFP, ACP$_L$-PfHO$^{84-305}$-GFP, and ACP$_L$-GFP and crosslinked in 1% paraformaldehyde for 15 minutes at 20°C, then quenched with 125mM glycine. Crosslinked parasites were transferred into 2 mL ChIP lysis/sonication buffer (200 mM NaCl, 25 mM Tris pH 7.5, 5 mM EDTA pH 8, 1% v/v Triton X-100, 0.1% SDS w/v, 0.5% sodium deoxycholate w/v, and protease inhibitors), and sonicated for 15 cycles of 30s ON/OFF at 25% power using a microtip on a Branson sonicator, then clarified by centrifugation (14,000 rpm, 10 min, 4°C). DNA fragment size after shearing was determined by Agilent Bioanalyzer DNA analysis (University of Utah DNA Sequencing Core) (**Figure 5 – figure supplement 4**). We collected 200µL (10%) of the clarified, sheared lysates as "input controls" and the incubated the rest with goat anti-GFP antibody (Abcam, ab5450) at 4°C overnight. Antibody-bound protein was mixed with equilibrated resin from 25 µL protein A-conjugated dynabeads (Invitrogen, 1011D) for 1 hour at 4°C rotating, then washed in lysis/sonication buffer, 1 mg/mL salmon sperm DNA (Invitrogen, AM9680) in lysis/sonication buffer, high salt wash buffer (500 mM NaCl, 25 mM Tris pH 7.5, 2 mM EDTA pH 8, 1% v/v Triton X-100, 0.1% w/v SDS, and protease inhibitors), and Tris-EDTA buffer. Samples were eluted from protein A dynabeads by two rounds of 5-minute incubation at 65°C in 100 µL elution buffer (10 mM Tris pH 8, 1 mM EDTA, 1% w/v SDS). We increased NaCl concentration in both input control and ChIP elution samples to 200 mM and added 50 µg/mL RNAse A, then incubated overnight (at least 8 hours) at 65°C to reverse crosslinks and digest RNA. We increased EDTA concentration to 5 mM and added 2 uL of 20 mg/mL Proteinase K and digested at 60°C for 1 hour, then purified DNA using the Qiagen PCR purification kit. Purified DNA was immediately used for either steady-state PCR using primers 62-73 or qPCR amplification using protocol described above. Relative quantification of steady-state PCR bands was performed by area-under-the-curve densitometry analysis in FIJI. In qPCR experiments, amplification of each gene in ChIP DNA was normalized to amplification of the same gene in DNA purified from the input control to account for variability between parasite lines. All densitometry and qPCR experiments were performed in triplicate

and statistical significance of differences between PfHO-GFP and other constructs was calculated using Student's t-test.

Acknowledgements. We thank Wandy Beatty and Josh Beck for assistance with electron microscopy and western blot experiments, respectively, and thank Geoff McFadden, Jacquin Niles, Akhil Vaidya, Dennis Winge, and members of the Goldberg and Sigala labs for helpful discussions. We thank Dick Winant at the Stanford PAN facility for assistance with N-terminal protein sequencing. We thank the staff of the Photon factory for excellent technical support. Access to beamline BL5A and AR-NW12A was granted by the Photon Factory Advisory Committee (Proposals 2011G574, and 2012G191). This work was supported by NIH grants R35GM153408 (J.A.W.), R21AI110712 (D.E.G.), and R35GM133764 (P.A.S.); a Burroughs Wellcome Fund Career Award at the Scientific Interface (P.A.S.); and a Pew Biomedical Scholarship from the Pew Charitable Trusts (P.A.S.). A.M.B. was supported in part by NIH Training Grant T32DK007115. C.S. was supported by NIH grant R25HG009886 and by R35GM133764-02S1 (P.A.S.). DNA synthesis and sequencing, fluorescence microscopy, and flow cytometry were performed using core facilities at the University of Utah.

Data availability. Atomic coordinates and structure factors have been deposited in the RCSB Protein Data Bank as entry 8ZLD. The proteomics data are deposited in the MassIVE data repository (https://massive.ucsd.edu) under the identifier MSV000094692.

References.

1. Naß J, Efferth T. Development of artemisinin resistance in malaria therapy. *Pharmacol Res*. 2019;146:104275. doi:10.1016/j.phrs.2019.104275

2. Lubell Y, Dondorp A, Guérin PJ, et al. Artemisinin resistance – modelling the potential human and economic costs. *Malar J*. 2014;13(1):452. doi:10.1186/1475-2875-13-452

3. Ball EG, McKee RW, Anfinsen CB, Cruz WO, Geiman QM. STUDIES ON MALARIAL PARASITES: IX. CHEMICAL AND METABOLIC CHANGES DURING GROWTH AND MULTIPLICATION IN VIVO AND IN VITRO. *J Biol Chem*. 1948;175(2):547-571. doi:10.1016/S0021-9258(18)57175-1

4. Francis SE, Sullivan DJ, Goldberg DE. Hemoglobin metabolism in the malaria parasite Plasmodium falciparum. *Annu Rev Microbiol*. 1997;51:97-123. doi:10.1146/annurev.micro.51.1.97

5. Elbirt KK, Bonkovsky HL. Heme Oxygenase: Recent Advances in Understanding Its Regulation and Role. *Proc Assoc Am Physicians*. 2018;111(5):438-447. doi:10.1111/paa.1999.111.5.438

6. Vijayan V, Wagener FADTG, Immenschuh S. The macrophage heme-heme oxygenase-1 system and its role in inflammation. *Biochem Pharmacol*. 2018;153:159-167. doi:10.1016/j.bcp.2018.02.010

7. Bottino-Rojas V, Pereira LOR, Silva G, et al. Non-canonical transcriptional regulation of heme oxygenase in Aedes aegypti. *Sci Rep*. 2019;9:13726. doi:10.1038/s41598-019-49396-3

8. Sigala PA, Crowley JR, Hsieh S, Henderson JP, Goldberg DE. Direct tests of enzymatic heme degradation by the malaria parasite Plasmodium falciparum. *J Biol Chem*. 2012;287(45):37793-37807. doi:10.1074/jbc.M112.414078

9. Okada K. The novel heme oxygenase-like protein from Plasmodium falciparum converts heme to bilirubin IXα in the apicoplast. *FEBS Lett*. 2009;583(2):313-319. doi:10.1016/j.febslet.2008.12.015

10. Bushell E, Gomes AR, Sanderson T, et al. Functional Profiling of a Plasmodium Genome Reveals an Abundance of Essential Genes. *Cell*. 2017;170(2):260-272.e8. doi:10.1016/j.cell.2017.06.030

11. Zhang M, Wang C, Otto TD, et al. Uncovering the essential genome of the human malaria parasite Plasmodium falciparum by saturation mutagenesis. *Science*. 2018;360(6388):eaap7847. doi:10.1126/science.aap7847

12. Wilks A. Heme Oxygenase: Evolution, Structure, and Mechanism. *Antioxid Redox Signal*. 2002;4(4):603-614. doi:10.1089/15230860260220102

13. Tenhunen R, Marver HS, Schmid R. The enzymatic conversion of heme to bilirubin by microsomal heme oxygenase. *Proc Natl Acad Sci*. 1968;61(2):748-755. doi:10.1073/pnas.61.2.748

14. Davis SJ, Bhoo SH, Durski AM, Walker JM, Vierstra RD. The Heme-Oxygenase Family Required for Phytochrome Chromophore Biosynthesis Is Necessary for Proper Photomorphogenesis in Higher Plants. *Plant Physiol*. 2001;126(2):656-669.

15. Lin Q, Weis S, Yang G, et al. Heme Oxygenase-1 Protein Localizes to the Nucleus and Activates Transcription Factors Important in Oxidative Stress. *J Biol Chem*. 2007;282(28):20621-20633. doi:10.1074/jbc.M607954200

16. Mascaró M, Alonso EN, Alonso EG, Lacunza E, Curino AC, Facchinetti MM. Nuclear Localization of Heme Oxygenase-1 in Pathophysiological Conditions: Does It Explain the Dual Role in Cancer? *Antioxidants*. 2021;10(1):87. doi:10.3390/antiox10010087

17. Jagadeesh ASV, Fang X, Kim SH, et al. Non-canonical vs. Canonical Functions of Heme Oxygenase-1 in Cancer. *J Cancer Prev*. 2022;27(1):7-15. doi:10.15430/JCP.2022.27.1.7

18. Gisk B, Yasui Y, Kohchi T, Frankenberg-Dinkel N. Characterization of the haem oxygenase protein family in Arabidopsis thaliana reveals a diversity of functions. *Biochem J*. 2009;425(2):425-434. doi:10.1042/BJ20090775

19. Altschul SF, Gish W, Miller W, Myers EW, Lipman DJ. Basic local alignment search tool. *J Mol Biol*. 1990;215(3):403-410. doi:10.1016/S0022-2836(05)80360-2

20. Potter SC, Luciani A, Eddy SR, Park Y, Lopez R, Finn RD. HMMER web server: 2018 update. *Nucleic Acids Res*. 2018;46(W1):W200-W204. doi:10.1093/nar/gky448

21. Kloehn J, Harding CR, Soldati-Favre D. Supply and demand—heme synthesis, salvage and utilization by Apicomplexa. *FEBS J*. 2021;288(2):382-404. doi:10.1111/febs.15445

22. Holm L, Laiho A, Törönen P, Salgado M. DALI shines a light on remote homologs: One hundred discoveries. *Protein Sci*. 2023;32(1):e4519. doi:10.1002/pro.4519

23. Lad L, Koshkin A, Montellano PRO de, Poulos TL. Crystal structures of the G139A, G139A–NO and G143H mutants of human heme oxygenase-1. A finely tuned hydrogen-bonding network controls oxygenase versus peroxidase activity. *JBIC J Biol Inorg Chem*. 2005;10(2):138-146. doi:10.1007/s00775-004-0620-6

24. Wang J, Li X, Chang JW, et al. Enzymological and structural characterization of Arabidopsis thaliana heme oxygenase-1. *FEBS Open Bio*. 2022;12(9):1677-1687. doi:10.1002/2211-5463.13453

25. Tohda R, Tanaka H, Mutoh R, et al. Crystal structure of higher plant heme oxygenase-1 and its mechanism of interaction with ferredoxin. *J Biol Chem*. 2021;296:100217. doi:10.1074/jbc.RA120.016271

26. Sugishima M, Sakamoto H, Kakuta Y, et al. Crystal Structure of Rat Apo-Heme Oxygenase-1 (HO-1): Mechanism of Heme Binding in HO-1 Inferred from Structural Comparison of the Apo and Heme Complex Forms,. *Biochemistry*. 2002;41(23):7293-7300. doi:10.1021/bi025662a

27. Wang J, Niemevz F, Lad L, et al. Human Heme Oxygenase Oxidation of 5- and 15-Phenylhemes*. *J Biol Chem*. 2004;279(41):42593-42604. doi:10.1074/jbc.M406346200

28. Jumper J, Evans R, Pritzel A, et al. Highly accurate protein structure prediction with AlphaFold. *Nature*. 2021;596(7873):583-589. doi:10.1038/s41586-021-03819-2

29. Baker NA, Sept D, Joseph S, Holst MJ, McCammon JA. Electrostatics of nanosystems: Application to microtubules and the ribosome. *Proc Natl Acad Sci*. 2001;98(18):10037-10041. doi:10.1073/pnas.181342398

30. Sugishima M, Migita CT, Zhang X, Yoshida T, Fukuyama K. Crystal structure of heme oxygenase-1 from cyanobacterium Synechocystis sp. PCC 6803 in complex with heme. *Eur J Biochem*. 2004;271(22):4517-4525. doi:10.1111/j.1432-1033.2004.04411.x

31. Wang J, de Montellano PRO. The binding sites on human heme oxygenase-1 for cytochrome p450 reductase and biliverdin reductase. *J Biol Chem*. 2003;278(22):20069-20076. doi:10.1074/jbc.M300989200

32. Holm L. Using Dali for Protein Structure Comparison. *Methods Mol Biol Clifton NJ*. 2020;2112:29-42. doi:10.1007/978-1-0716-0270-6_3

33. Waller RF, Reed MB, Cowman AF, McFadden GI. Protein trafficking to the plastid of Plasmodium falciparum is via the secretory pathway. *EMBO J*. 2000;19(8):1794-1802. doi:10.1093/emboj/19.8.1794

34. Zuegge J, Ralph S, Schmuker M, McFadden GI, Schneider G. Deciphering apicoplast targeting signals – feature extraction from nuclear-encoded precursors of Plasmodium falciparum apicoplast proteins. *Gene*. 2001;280(1):19-26. doi:10.1016/S0378-1119(01)00776-4

35. Almagro Armenteros JJ, Tsirigos KD, Sønderby CK, et al. SignalP 5.0 improves signal peptide predictions using deep neural networks. *Nat Biotechnol*. 2019;37(4):420-423. doi:10.1038/s41587-019-0036-z

36. Käll L, Krogh A, Sonnhammer ELL. A combined transmembrane topology and signal peptide prediction method. *J Mol Biol*. 2004;338(5):1027-1036. doi:10.1016/j.jmb.2004.03.016

37. Mallari JP, Oksman A, Vaupel B, Goldberg DE. Kinase-associated Endopeptidase 1 (Kae1) Participates in an Atypical Ribosome-associated Complex in the Apicoplast of Plasmodium falciparum. *J Biol Chem*. 2014;289(43):30025-30039. doi:10.1074/jbc.M114.586735

38. Yeh E, DeRisi JL. Chemical Rescue of Malaria Parasites Lacking an Apicoplast Defines Organelle Function in Blood-Stage Plasmodium falciparum. *PLOS Biol*. 2011;9(8):e1001138. doi:10.1371/journal.pbio.1001138

39. Black M, Seeber F, Soldati D, Kim K, Boothroyd JC. Restriction enzyme-mediated integration elevates transformation frequency and enables co-transfection of Toxoplasma gondii. *Mol Biochem Parasitol*. 1995;74(1):55-63. doi:10.1016/0166-6851(95)02483-2

40. Muralidharan V, Oksman A, Iwamoto M, Wandless TJ, Goldberg DE. Asparagine repeat function in a Plasmodium falciparum protein assessed via a regulatable fluorescent affinity tag. *Proc Natl Acad Sci*. 2011;108(11):4411-4416. doi:10.1073/pnas.1018449108

41. Armstrong CM, Goldberg DE. An FKBP destabilization domain modulates protein levels in Plasmodium falciparum. *Nat Methods*. 2007;4(12):1007-1009. doi:10.1038/nmeth1132

42. Liu J, Gluzman IY, Drew ME, Goldberg DE. The role of Plasmodium falciparum food vacuole plasmepsins. *J Biol Chem*. 2005;280(2):1432-1437. doi:10.1074/jbc.M409740200

43. Prommana P, Uthaipibull C, Wongsombat C, et al. Inducible Knockdown of Plasmodium Gene Expression Using the glmS Ribozyme. *PLOS ONE*. 2013;8(8):e73783. doi:10.1371/journal.pone.0073783

44. Winkler WC, Nahvi A, Roth A, Collins JA, Breaker RR. Control of gene expression by a natural metabolite-responsive ribozyme. *Nature*. 2004;428(6980):281-286. doi:10.1038/nature02362

45. Goldfless SJ, Wagner JC, Niles JC. Versatile control of Plasmodium falciparum gene expression with an inducible protein-RNA interaction. *Nat Commun*. 2014;5:5329. doi:10.1038/ncomms6329

46. Nasamu AS, Falla A, Pasaje CFA, et al. An integrated platform for genome engineering and gene expression perturbation in Plasmodium falciparum. *Sci Rep*. 2021;11(1):342. doi:10.1038/s41598-020-77644-4

47. Ganesan SM, Falla A, Goldfless SJ, Nasamu AS, Niles JC. Synthetic RNA–protein modules integrated with native translation mechanisms to control gene expression in malaria parasites. *Nat Commun*. 2016;7:10727. doi:10.1038/ncomms10727

48. Maruthi M, Ling L, Zhou J, Ke H. Dispensable Role of Mitochondrial Fission Protein 1 (Fis1) in the Erythrocytic Development of Plasmodium falciparum. *mSphere*. 2020;5(5):e00579-20. doi:10.1128/mSphere.00579-20

49. Okada M, Rajaram K, Swift RP, et al. Critical role for isoprenoids in apicoplast biogenesis by malaria parasites. Soldati-Favre D, Ralph SA, Kooij TW, eds. *eLife*. 2022;11:e73208. doi:10.7554/eLife.73208

50. García-Guerrero AE, Marvin RG, Blackwell AM, Sigala PA. Biogenesis of cytochromes c and c1 in the electron transport chain of malaria parasites. Published online February 1, 2024:2024.02.01.575742. doi:10.1101/2024.02.01.575742

51. van Dooren GG, Su V, D'Ombrain MC, McFadden GI. Processing of an Apicoplast Leader Sequence inPlasmodium falciparum and the Identification of a Putative Leader Cleavage Enzyme*. *J Biol Chem*. 2002;277(26):23612-23619. doi:10.1074/jbc.M201748200

52. Gallagher JR, Matthews KA, Prigge ST. Plasmodium falciparum apicoplast transit peptides are unstructured in vitro and during apicoplast import. *Traffic Cph Den*. 2011;12(9):1124-1138. doi:10.1111/j.1600-0854.2011.01232.x

53. Scaffa A, Tollefson GA, Yao H, et al. Identification of Heme Oxygenase-1 as a Putative DNA-Binding Protein. *Antioxid Basel Switz*. 2022;11(11):2135. doi:10.3390/antiox11112135

54. Dennery PA. Signaling function of heme oxygenase proteins. *Antioxid Redox Signal*. 2014;20(11):1743-1753. doi:10.1089/ars.2013.5674

55. Wu J, Li S, Li C, Cui L, Ma J, Hui Y. The non-canonical effects of heme oxygenase-1, a classical fighter against oxidative stress. *Redox Biol*. 2021;47:102170. doi:10.1016/j.redox.2021.102170

56. Falekun S, Sepulveda J, Jami-Alahmadi Y, Park H, Wohlschlegel JA, Sigala PA. Divergent acyl carrier protein decouples mitochondrial Fe-S cluster biogenesis from fatty acid synthesis in malaria parasites. *eLife*. 2021;10:e71636. doi:10.7554/eLife.71636

57. Espino-Sanchez TJ, Wienkers H, Marvin RG, et al. Direct tests of cytochrome c and c1 functions in the electron transport chain of malaria parasites. *Proc Natl Acad Sci*. 2023;120(19):e2301047120. doi:10.1073/pnas.2301047120

58. Boucher MJ, Ghosh S, Zhang L, et al. Integrative proteomics and bioinformatic prediction enable a high-confidence apicoplast proteome in malaria parasites. *PLOS Biol*. 2018;16(9):e2005895. doi:10.1371/journal.pbio.2005895

59. Trempe JF, Šašková KG, Sivá M, et al. Structural studies of the yeast DNA damage-inducible protein Ddi1 reveal domain architecture of this eukaryotic protein family. *Sci Rep*. 2016;6:33671. doi:10.1038/srep33671

60. Koizumi S, Irie T, Hirayama S, et al. The aspartyl protease DDI2 activates Nrf1 to compensate for proteasome dysfunction. *eLife*. 2016;5:e18357. doi:10.7554/eLife.18357

61. Lehrbach NJ, Ruvkun G. Proteasome dysfunction triggers activation of SKN-1A/Nrf1 by the aspartic protease DDI-1. Dillin A, ed. *eLife*. 2016;5:e17721. doi:10.7554/eLife.17721

62. Biswas C, Shah N, Muthu M, et al. Nuclear Heme Oxygenase-1 (HO-1) Modulates Subcellular Distribution and Activation of Nrf2, Impacting Metabolic and Anti-oxidant Defenses. *J Biol Chem*. 2014;289(39):26882-26894. doi:10.1074/jbc.M114.567685

63. Hsu FF, Chiang MT, Li FA, Yeh CT, Lee WH, Chau LY. Acetylation is essential for nuclear heme oxygenase-1-enhanced tumor growth and invasiveness. *Oncogene*. 2017;36(49):6805-6814. doi:10.1038/onc.2017.294

64. Krzeptowski W, Chudy P, Sokołowski G, et al. Proximity Ligation Assay Detection of Protein–DNA Interactions—Is There a Link between Heme Oxygenase-1 and G-quadruplexes? *Antioxidants*. 2021;10(1):94. doi:10.3390/antiox10010094

65. Köhler S, Delwiche CF, Denny PW, et al. A Plastid of Probable Green Algal Origin in Apicomplexan Parasites. *Science*. 1997;275(5305):1485-1489. doi:10.1126/science.275.5305.1485

66. Martins-Duarte ÉS, Sheiner L, Reiff SB, de Souza W, Striepen B. Replication and partitioning of the apicoplast genome of Toxoplasma gondii is linked to the cell cycle and requires DNA polymerase and gyrase. *Int J Parasitol*. 2021;51(6):493-504. doi:10.1016/j.ijpara.2020.11.004

67. Lemgruber L, Kudryashev M, Dekiwadia C, et al. Cryo-electron tomography reveals four-membrane architecture of the Plasmodium apicoplast. *Malar J*. 2013;12:25. doi:10.1186/1475-2875-12-25

68. Sullivan AE, Santos SDM. An Optimized Protocol for ChIP-Seq from Human Embryonic Stem Cell Cultures. *STAR Protoc*. 2020;1(2):100062. doi:10.1016/j.xpro.2020.100062

69. Wang W, Cheng L, Sun Q. Chromatin Immunoprecipitation in Chloroplasts. *Curr Protoc*. 2022;2(1):e360. doi:10.1002/cpz1.360

70. Raghu Ram EVS, Kumar A, Biswas S, et al. Nuclear gyrB encodes a functional subunit of the Plasmodium falciparum gyrase that is involved in apicoplast DNA replication. *Mol Biochem Parasitol*. 2007;154(1):30-39. doi:10.1016/j.molbiopara.2007.04.001

71. Prusty D, Dar A, Priya R, et al. Single-stranded DNA binding protein from human malarial parasite Plasmodium falciparum is encoded in the nucleus and targeted to the apicoplast. *Nucleic Acids Res*. 2010;38(20):7037-7053. doi:10.1093/nar/gkq565

72. Buguliskis JS, Casta LJ, Butz CE, Matsumoto Y, Taraschi TF. Expression and biochemical characterization of *Plasmodium falciparum* DNA ligase I. *Mol Biochem Parasitol*. 2007;155(2):128-137. doi:10.1016/j.molbiopara.2007.06.011

73. Nisbet RER, McKenzie JL. Transcription of the apicoplast genome. *Mol Biochem Parasitol*. 2016;210(1-2):5-9. doi:10.1016/j.molbiopara.2016.07.004

74. Nisbet RER, Kurniawan DP, Bowers HD, Howe CJ. Transcripts in the Plasmodium Apicoplast Undergo Cleavage at tRNAs and Editing, and Include Antisense Sequences. *Protist*. 2016;167(4):377-388. doi:10.1016/j.protis.2016.06.003

75. Kobayashi Y, Komatsuya K, Imamura S, et al. Coordination of apicoplast transcription in a malaria parasite by internal and host cues. *Proc Natl Acad Sci*. 2023;120(28):e2214765120. doi:10.1073/pnas.2214765120

76. Wilson RJ, Denny PW, Preiser PR, et al. Complete gene map of the plastid-like DNA of the malaria parasite Plasmodium falciparum. *J Mol Biol*. 1996;261(2):155-172. doi:10.1006/jmbi.1996.0449

77. Milton ME, Nelson SW. Replication and maintenance of the Plasmodium falciparum apicoplast genome. *Mol Biochem Parasitol*. 2016;208(2):56-64. doi:10.1016/j.molbiopara.2016.06.006

78. Painter HJ, Chung NC, Sebastian A, Albert I, Storey JD, Llinás M. Genome-wide real-time in vivo transcriptional dynamics during Plasmodium falciparum blood-stage development. *Nat Commun*. 2018;9(1):2656. doi:10.1038/s41467-018-04966-3

79. Llinás M, Bozdech Z, Wong ED, Adai AT, DeRisi JL. Comparative whole genome transcriptome analysis of three Plasmodium falciparum strains. *Nucleic Acids Res*. 2006;34(4):1166-1173. doi:10.1093/nar/gkj517

80. Dorrell RG, Drew J, Nisbet RER, Howe CJ. Evolution of Chloroplast Transcript Processing in Plasmodium and Its Chromerid Algal Relatives. *PLOS Genet*. 2014;10(1):e1004008. doi:10.1371/journal.pgen.1004008

81. Ojala D, Montoya J, Attardi G. tRNA punctuation model of RNA processing in human mitochondria. *Nature*. 1981;290(5806):470-474. doi:10.1038/290470a0

82. Ram EVSR, Naik R, Ganguli M, Habib S. DNA organization by the apicoplast-targeted bacterial histone-like protein of Plasmodium falciparum. *Nucleic Acids Res*. 2008;36(15):5061-5073. doi:10.1093/nar/gkn483

83. Augagneur Y, Wesolowski D, Tae HS, Altman S, Ben Mamoun C. Gene selective mRNA cleavage inhibits the development of Plasmodium falciparum. *Proc Natl Acad Sci*. 2012;109(16):6235-6240. doi:10.1073/pnas.1203516109

84. Pakosz Z, Lin TY, Michalczyk E, Nagano S, Heddle JG. Inhibitory Compounds Targeting Plasmodium falciparum Gyrase B. *Antimicrob Agents Chemother*. 2021;65(10):e0026721. doi:10.1128/AAC.00267-21

85. Lindner SE, Llinás M, Keck JL, Kappe SHI. The primase domain of PfPrex is a proteolytically matured, essential enzyme of the apicoplast. *Mol Biochem Parasitol*. 2011;180(2):69-75. doi:10.1016/j.molbiopara.2011.08.002

86. Sasaki N, Hirai M, Maeda K, et al. The Plasmodium HU homolog, which binds the plastid DNA sequence-independent manner, is essential for the parasite's survival. *FEBS Lett*. 2009;583(9):1446-1450. doi:10.1016/j.febslet.2009.03.071

87. Oostra BA, Gruber M. Involvement of DNA gyrase in the transcription of ribosomal RNA. *Nucleic Acids Res*. 1980;8(18):4235-4246.

88. Gupta R, China A, Manjunatha UH, Ponnanna NM, Nagaraja V. A complex of DNA gyrase and RNA polymerase fosters transcription in *Mycobacterium smegmatis*. *Biochem Biophys Res Commun*. 2006;343(4):1141-1145. doi:10.1016/j.bbrc.2006.02.195

89. Wahle E, Mueller K, Orr E. Effect of DNA gyrase inactivation on RNA synthesis in Escherichia coli. *J Bacteriol*. 1985;162(1):458-460. doi:10.1128/jb.162.1.458-460.1985

90. Champoux JJ. DNA Topoisomerases: Structure, Function, and Mechanism. *Annu Rev Biochem*. 2001;70(1):369-413. doi:10.1146/annurev.biochem.70.1.369

91. Ahmed W, Sala C, Hegde SR, Jha RK, Cole ST, Nagaraja V. Transcription facilitated genome-wide recruitment of topoisomerase I and DNA gyrase. *PLOS Genet*. 2017;13(5):e1006754. doi:10.1371/journal.pgen.1006754

92. Dorman CJ. DNA supercoiling and transcription in bacteria: a two-way street. *BMC Mol Cell Biol*. 2019;20(1):26. doi:10.1186/s12860-019-0211-6

93. Feagin JE, Drew ME. Plasmodium falciparum: Alterations in Organelle Transcript Abundance during the Erythrocytic Cycle. *Exp Parasitol*. 1995;80(3):430-440. doi:10.1006/expr.1995.1055

94. Berger M, Farcas A, Geertz M, et al. Coordination of genomic structure and transcription by the main bacterial nucleoid-associated protein HU. *EMBO Rep*. 2010;11(1):59-64. doi:10.1038/embor.2009.232

95. Oberto J, Nabti S, Jooste V, Mignot H, Rouviere-Yaniv J. The HU regulon is composed of genes responding to anaerobiosis, acid stress, high osmolarity and SOS induction. *PloS One*. 2009;4(2):e4367. doi:10.1371/journal.pone.0004367

96. Dillon SC, Dorman CJ. Bacterial nucleoid-associated proteins, nucleoid structure and gene expression. *Nat Rev Microbiol*. 2010;8(3):185-195. doi:10.1038/nrmicro2261

97. Hao JD, Liu QL, Liu MX, et al. DDX21 mediates co-transcriptional RNA m6A modification to promote transcription termination and genome stability. *Mol Cell*. Published online March 26, 2024:S1097-2765(24)00188-6. doi:10.1016/j.molcel.2024.03.006

98. Song C, Hotz-Wagenblatt A, Voit R, Grummt I. SIRT7 and the DEAD-box helicase DDX21 cooperate to resolve genomic R loops and safeguard genome stability. *Genes Dev*. 2017;31(13):1370-1381. doi:10.1101/gad.300624.117

99. Saha S, Yang X, Huang SYN, et al. Resolution of R-loops by topoisomerase III-β (TOP3B) in coordination with the DEAD-box helicase DDX5. *Cell Rep*. 2022;40(2):111067. doi:10.1016/j.celrep.2022.111067

100. Savino TM, Bastos R, Jansen E, Hernandez-Verdun D. The nucleolar antigen Nop52, the human homologue of the yeast ribosomal RNA processing RRP1, is recruited at late stages of nucleologenesis. *J Cell Sci*. 1999;112 (Pt 12):1889-1900. doi:10.1242/jcs.112.12.1889

101. Sanghai ZA, Piwowarczyk R, Broeck AV, Klinge S. A co-transcriptional ribosome assembly checkpoint controls nascent large ribosomal subunit maturation. *Nat Struct Mol Biol*. 2023;30(5):594-599. doi:10.1038/s41594-023-00947-3

102. Davis JH, Williamson JR. Structure and dynamics of bacterial ribosome biogenesis. *Philos Trans R Soc B Biol Sci*. 2017;372(1716):20160181. doi:10.1098/rstb.2016.0181

103. Paul BJ, Ross W, Gaal T, Gourse RL. rRNA transcription in Escherichia coli. *Annu Rev Genet*. 2004;38:749-770. doi:10.1146/annurev.genet.38.072902.091347

104. Jourdain AA, Popow J, de la Fuente MA, Martinou JC, Anderson P, Simarro M. The FASTK family of proteins: emerging regulators of mitochondrial RNA biology. *Nucleic Acids Res*. 2017;45(19):10941-10947. doi:10.1093/nar/gkx772

105. Boucher MJ, Yeh E. Plastid–endomembrane connections in apicomplexan parasites. *PLoS Pathog*. 2019;15(6):e1007661. doi:10.1371/journal.ppat.1007661

106. Sanchez-Puerta MV, Delwiche CF. A HYPOTHESIS FOR PLASTID EVOLUTION IN CHROMALVEOLATES(1). *J Phycol*. 2008;44(5):1097-1107. doi:10.1111/j.1529-8817.2008.00559.x

107. Keeling PJ. The number, speed, and impact of plastid endosymbioses in eukaryotic evolution. *Annu Rev Plant Biol*. 2013;64:583-607. doi:10.1146/annurev-arplant-050312-120144

108. McFadden GI, Reith ME, Munholland J, Lang-Unnasch N. Plastid in human parasites. *Nature*. 1996;381(6582):482-482. doi:10.1038/381482a0

109. Janouškovec J, Tikhonenkov DV, Burki F, et al. Factors mediating plastid dependency and the origins of parasitism in apicomplexans and their close relatives. *Proc Natl Acad Sci U S A*. 2015;112(33):10200-10207. doi:10.1073/pnas.1423790112

110. Woo YH, Ansari H, Otto TD, et al. Chromerid genomes reveal the evolutionary path from photosynthetic algae to obligate intracellular parasites. *eLife*. 4:e06974. doi:10.7554/eLife.06974

111. Emborg TJ, Walker JM, Noh B, Vierstra RD. Multiple Heme Oxygenase Family Members Contribute to the Biosynthesis of the Phytochrome Chromophore in Arabidopsis. *Plant Physiol*. 2006;140(3):856-868. doi:10.1104/pp.105.074211

112. Aoki R, Goto T, Fujita Y. A heme oxygenase isoform is essential for aerobic growth in the cyanobacterium Synechocystis sp. PCC 6803: modes of differential operation of two isoforms/enzymes to adapt to low oxygen environments in cyanobacteria. *Plant Cell Physiol*. 2011;52(10):1744-1756. doi:10.1093/pcp/pcr108

113. Oborník M, Lukeš J. Chapter Eight - Cell Biology of Chromerids: Autotrophic Relatives to Apicomplexan Parasites. In: Jeon KW, ed. *International Review of Cell and Molecular Biology*. Vol 306. International Review of Cell and Molecular Biology. Academic Press; 2013:333-369. doi:10.1016/B978-0-12-407694-5.00008-0

114. Goldberg DE, Slater AF, Cerami A, Henderson GB. Hemoglobin degradation in the malaria parasite Plasmodium falciparum: an ordered process in a unique organelle. *Proc Natl Acad Sci U S A*. 1990;87(8):2931-2935. doi:10.1073/pnas.87.8.2931

115. Abshire JR, Rowlands CJ, Ganesan SM, So PTC, Niles JC. Quantification of labile heme in live malaria parasites using a genetically encoded biosensor. *Proc Natl Acad Sci*. 2017;114(11):E2068-E2076. doi:10.1073/pnas.1615195114

116. Vanella L, Barbagallo I, Tibullo D, Forte S, Zappalà A, Volti GL. The non-canonical functions of the heme oxygenases. *Oncotarget*. 2016;7(42):69075. doi:10.18632/oncotarget.11923

117. Maclean AE, Bridges HR, Silva MF, et al. Complexome profile of Toxoplasma gondii mitochondria identifies divergent subunits of respiratory chain complexes including new subunits of cytochrome bc1 complex. *PLoS Pathog*. 2021;17(3):e1009301. doi:10.1371/journal.ppat.1009301

118. Mühleip A, Kock Flygaard R, Ovciarikova J, et al. ATP synthase hexamer assemblies shape cristae of Toxoplasma mitochondria. *Nat Commun*. 2021;12(1):120. doi:10.1038/s41467-020-20381-z

119. Amos B, Aurrecoechea C, Barba M, et al. VEuPathDB: the eukaryotic pathogen, vector and host bioinformatics resource center. *Nucleic Acids Res*. 2022;50(D1):D898-D911. doi:10.1093/nar/gkab929

120. The UniProt Consortium. UniProt: the Universal Protein Knowledgebase in 2023. *Nucleic Acids Res*. 2023;51(D1):D523-D531. doi:10.1093/nar/gkac1052

121. Sievers F, Higgins DG. Clustal Omega, accurate alignment of very large numbers of sequences. *Methods Mol Biol Clifton NJ*. 2014;1079:105-116. doi:10.1007/978-1-62703-646-7_6

122. Waterhouse AM, Procter JB, Martin DMA, Clamp M, Barton GJ. Jalview Version 2—a multiple sequence alignment editor and analysis workbench. *Bioinformatics*. 2009;25(9):1189-1191. doi:10.1093/bioinformatics/btp033

123. Jurrus E, Engel D, Star K, et al. Improvements to the APBS biomolecular solvation software suite. *Protein Sci Publ Protein Soc*. 2018;27(1):112-128. doi:10.1002/pro.3280

124. Wellems TE, Panton LJ, Gluzman IY, et al. Chloroquine resistance not linked to mdr-like genes in a Plasmodium falciparum cross. *Nature*. 1990;345(6272):253-255. doi:10.1038/345253a0

125. Fidock DA, Wellems TE. Transformation with human dihydrofolate reductase renders malaria parasites insensitive to WR99210 but does not affect the intrinsic activity of proguanil. *Proc Natl Acad Sci U S A*. 1997;94(20):10931-10936. doi:10.1073/pnas.94.20.10931

126. Ganesan SM, Morrisey JM, Ke H, et al. Yeast Dihydroorotate Dehydrogenase as a New Selectable Marker for Plasmodium falciparum Transfection. *Mol Biochem Parasitol*. 2011;177(1):29-34. doi:10.1016/j.molbiopara.2011.01.004

127. Mamoun CB, Gluzman IY, Goyard S, Beverley SM, Goldberg DE. A set of independent selectable markers for transfection of the human malaria parasite Plasmodium falciparum. *Proc Natl Acad Sci*. 1999;96(15):8716-8720. doi:10.1073/pnas.96.15.8716

128. Sigala PA, Crowley JR, Henderson JP, Goldberg DE. Deconvoluting heme biosynthesis to target blood-stage malaria parasites. Clardy J, ed. *eLife*. 2015;4:e09143. doi:10.7554/eLife.09143

129. Balu B, Shoue DA, Fraser MJ, Adams JH. High-efficiency transformation of Plasmodium falciparum by the lepidopteran transposable element piggyBac. *Proc Natl Acad Sci*. 2005;102(45):16391-16396. doi:10.1073/pnas.0504679102

130. Klemba M, Beatty W, Gluzman I, Goldberg DE. Trafficking of plasmepsin II to the food vacuole of the malaria parasite Plasmodium falciparum. *J Cell Biol*. 2004;164(1):47-56. doi:10.1083/jcb200307147

131. Spillman NJ, Beck JR, Ganesan SM, Niles JC, Goldberg DE. The chaperonin TRiC forms an oligomeric complex in the malaria parasite cytosol. *Cell Microbiol*. 2017;19(6):e12719. doi:10.1111/cmi.12719

132. Gallagher JR, Prigge ST. Plasmodium falciparum acyl carrier protein crystal structures in disulfide-linked and reduced states and their prevalence during blood stage growth. *Proteins*. 2010;78(3):575-588. doi:10.1002/prot.22582

133. Beck JR, Muralidharan V, Oksman A, Goldberg DE. PTEX component HSP101 mediates export of diverse malaria effectors into host erythrocytes. *Nature*. 2014;511(7511):592-595. doi:10.1038/nature13574

134. Ponpuak M, Klemba M, Park M, Gluzman IY, Lamppa GK, Goldberg DE. A role for falcilysin in transit peptide degradation in the Plasmodium falciparum apicoplast. *Mol Microbiol*. 2007;63(2):314-334. doi:10.1111/j.1365-2958.2006.05443.x

135. Mamoun CB, Goldberg DE. Plasmodium protein phosphatase 2C dephosphorylates translation elongation factor 1beta and inhibits its PKC-mediated nucleotide exchange activity in vitro. *Mol Microbiol*. 2001;39(4):973-981. doi:10.1046/j.1365-2958.2001.02289.x

136. Wohlschlegel JA. Identification of SUMO-conjugated proteins and their SUMO attachment sites using proteomic mass spectrometry. *Methods Mol Biol Clifton NJ*. 2009;497:33-49. doi:10.1007/978-1-59745-566-4_3

137. Jami-Alahmadi Y, Pandey V, Mayank AK, Wohlschlegel JA. A Robust Method for Packing High Resolution C18 RP-nano-HPLC Columns. *J Vis Exp JoVE*. 2021;(171). doi:10.3791/62380

138. Schmittgen TD, Livak KJ. Analyzing real-time PCR data by the comparative CT method. *Nat Protoc*. 2008;3(6):1101-1108. doi:10.1038/nprot.2008.73

A.

Accession	Description	Organism	BLAST Identity	BLAST E-value	HMM Identity	HMM E-value
XP_009689667.1	conserved hypothetical protein	*Theileria orientalis* strain Shintoku	33.3%	5.0E-25	33.2%	6.0E-26
XP_004833458.1	signal peptide containing protein	*Theileria equi* strain WA	33.1%	1.0E-24	34.7%	5.0E-26
PVC54810.1	hypothetical protein	*Theileria orientalis*	33.3%	1.0E-23	——	——
XP_012649431.2	heme oxygenase (HO)	*Babesia microti* strain RI	30.6%	2.0E-22	31.9%	1.5E-24
EAN34111.2	hypothetical protein	*Theileria parva* strain Muguga	33.9%	5.0E-20	——	——
EDO07256.2	putative integral membrane protein	*Babesia bovis* T2Bo	30.1%	7.0E-20	——	——
XP_953900.1	uncharacterized protein	*Theileria annulata*	——	——	33.9%	8.5E-22
XP_028870008.1	uncharacterized protein	*Babesia* sp. Xinjiang	29.4%	2.0E-19	30.3%	2.7E-21
XP_766394.1	hypothetical protein	*Theileria parva* strain Muguga	35.4%	2.0E-18	34.2%	2.9E-20
CEL99648.1	uncharacterized protein	*Vitrella brassicaformis*	——	——	26.6%	1.9E-14
ORY02253.1	heme oxygenase	*Basidiobolus meristosporus*	——	——	23.3%	3.0E-08
OEL18617.1	heme oxygenase 1, chloroplastic	*Dichanthelium oligosanthes*	——	——	27.4%	2.8E-06

B.

```
P. falciparum    MIRKIIILMFTFFSNIHNEKIY-HHKQRRKFLKGPLGYLNRNVIQKKHYNLY-AKKFINYKEIQIQRINDYRKRSGVDKN  78
T. orientalis    MYIGVVIATLTIFCDFNVIRCLGLAVESGLAFSPPRPYLRRIKVKNRISRDERKRRSEFSKQLHKELRMKYWRRIDPKIN  80
B. microti       MHNGQV----NIFLAILYVTMVVGYVPKRATLRPPKPNRKTPKG--P--ILHRREKAKESNQLRDELIMKYWRRVGKEVN  72
Syn sp.PCC 6803  ------------------------------------------------------------------------------  0
H. sapiens       ----------------------------------------------------------------------MERPQPD--  7

P. falciparum    NIN---YNLRDTYNYHETHLFVRNEVLPTLAKIENENLKEKEKNKEIFRNINDYNSNFTRQTFLQFLMDLYNIFLKIDDL  155
T. orientalis    EILKFDDPLAESYDLDPKRGFVVQEVIPRMVYVSD-SLKP-------LPLDESRSEEFDRQAGLQFLANIAAVTGVFVKE  152
B. microti       EVPFTDQSH--QQHIDTRRAFMSMYVLPKMAEISYKECDI-------LKLDEKKSSNFTRHSCLQFLCEIRNFFSVCAHG  143
Syn sp.PCC 6803  --------------------MSVNLASQLREGTK-KSHSMAENVGFVKC--FLKGVVEKNSYRKLVGNLYFVYSAMEEE  56
H. sapiens       --------------------SMPQDLSEALKEATK-EVHTQAENAEFMRN--FQKGQVTRDGFKLVMASLYHIYVALEEE  64
                                        :   :   :      . .       .      .  . :.    .: .:  .     .

P. falciparum    FLENKTYFSILI--YNGPMQLTNHLYDDIIYVSSVVENSDDVSPSEYCMEYISHLENLCEENKLSFLAHAYVFYKNFHLS  233
T. orientalis    FES-RKGLSFLS--EMGPSELLTRLETDISYISSLLNVEQ-QSLSRSCLEYVEFLKSLCEKSEIRFLSQCYVFFKEWHVS  228
B. microti       FNK-NEGLKELV--EMGPINEIPYLSNDITYIRKLINGSG-E-FTTEHGKYIDFLQKIAENDPIALVSHAYYFYKEWCLC  218
Syn sp.PCC 6803  MAKFKDHPILSHIYFPE-LNRKQSLEQDLQFYYGS-NWRQEVKISAAGQAYVDRVRQVAATAPELLVAHSYTRYLGD-LS  133
H. sapiens       IERNKESPVFAPVYFPEELHRKAALEQDLAFWYGP-RWQEVIPYTPAMQRYVKRLHEVGRTEPELLVAHAYTRYLGD-LS  142
                 :   .             .    *  *: :     .       :     *:. :..:       ::::.*  :    :.

P. falciparum    KEHLLKSICKY-LNIIKKLK-SSTYV----ADVENFEF----CLNKM------SRKWSRWEKDNFLASLHNATNKMM-IL  296
T. orientalis    KKTLLTNLRDH-LRLVNKLK-CSFYD----PDARNLEG----VLNLM------ASEWTRRQKDEFLNEIPLAYQKLSESL  292
B. microti       KFHVLNSIKLH-LRITRHFQ-SAGFN----EDVLNFEY----VLNML------ACSWSQVEKDNFLRNLSIASDMAK-CY  281
Syn sp.PCC 6803  GGQILKKIAQNAMNLHDG--GTAFYEFADIDDEKAFKNTYRQAMNDLPIDQATAERIVDEANDAFAMNMKMFNEL-EGNL  210
H. sapiens       GGQVLKKIAQKALDLPSSGEGLAFFTFPNIASATKFKQLYRSRMNSLEMTPAVRQRVIEEAKTAFLLNIQLFEEL-QELL  221
                    :*..:    : :       : :      .   ::      :* :              :  *  .:    :

P. falciparum    T-----KHFEKVKS-------------------------------------------------------  305
T. orientalis    V-----MPFV----------------------------------------------------------  297
B. microti       T-----QCFT----------------------------------------------------------  286
Syn sp.PCC 6803  IKAIGIMVFNSLTRRRSQGSTEV----GLATSEG--------------------------------  240
H. sapiens       THDTKDQSPSRAPGLRQRASNKVQDSAPVETPRGKPPLNTRSQAPLLRWVLTLSFLVATVAVGLYAM  288
```

Figure 1 – Figure supplement 1. Sequence homology of PfHO. (A) Sequence homologs of PfHO based on BLAST[1] and HMM[2] sequence-similarity searches. (B) Sequence alignment of PfHO (Q8IJS6) with SynHO1 (P72849), Human HO1 (P09601), and HO homologs in *Theileria orientalis* (J4C2V8) and *Babesia microti* (A0A1R4ACC9). Uniprot accession codes given in parentheses.

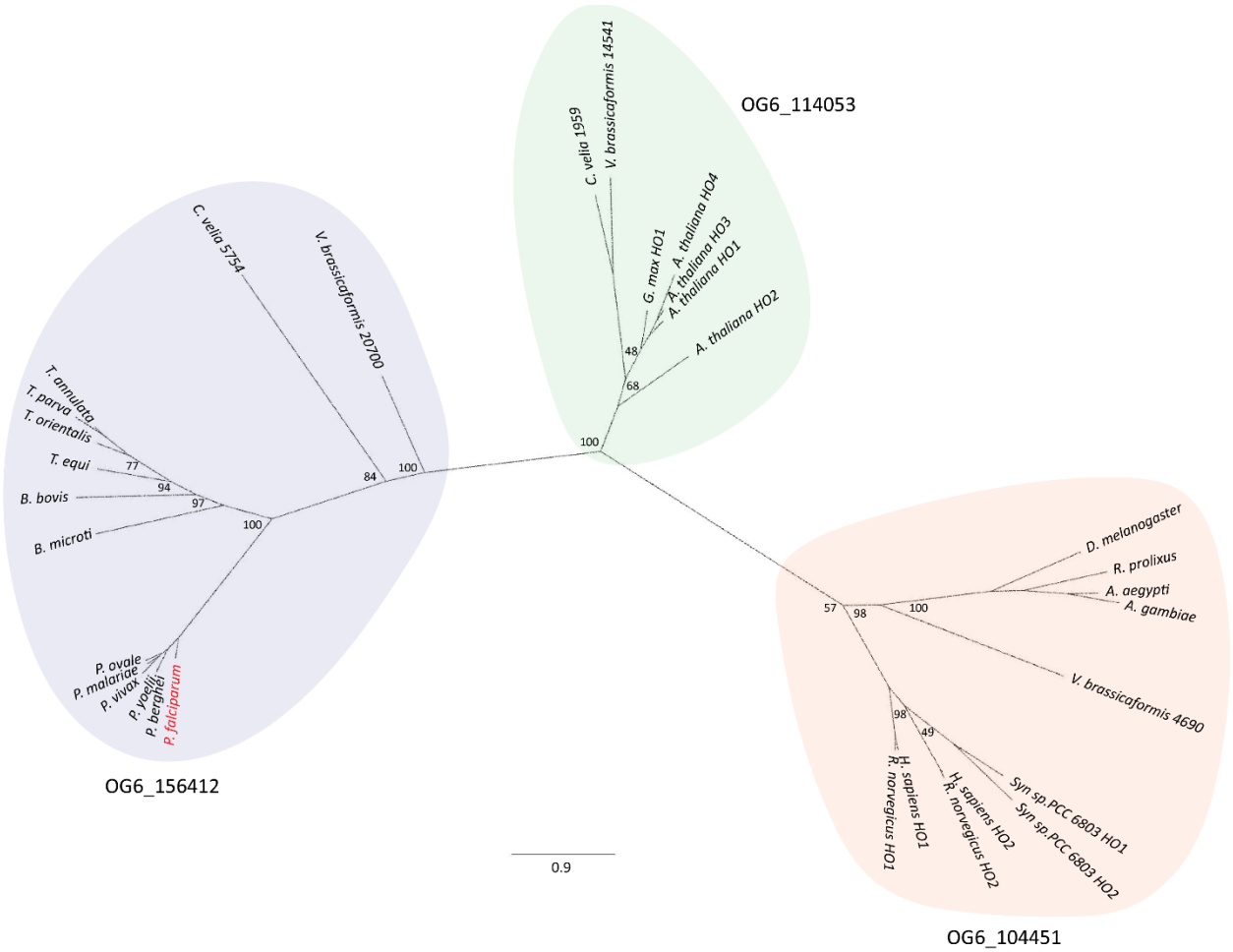

Figure 1 – Figure supplement 2. Phylogenic tree of mammalian, plant, algal, and hematozoan HOs. Nodes are annotated with bootstrap values for each branch. Ortholog groups independently predicted by OrthoMCL[3] are annotated for each colored section. Only select *Plasmodium* HOs are included for clarity, but all other known proteins of OG6_156412 are displayed. PfHO is marked in red.

Data Collection	**WT**	**SeMet**
Space Group	$P\ 2_1\ 2_1\ 2_1$	$P\ 2_1\ 2_1\ 2_1$
Unit cell		
a, b, c (Å)	54.91, 55.37, 162.40	55.37, 55.64, 164.64
Angles (°)	α = β = γ = 90	α = β = γ = 90
Resolution (Å)	55.4 – 2.78 (2.93 – 2.78)	31.9 – 2.65 (2.79 – 2.65)
Wavelength	1.0000	0.97921
Observations	85,682 (11,778)	128,208 (18,962)
Unique reflections	13,064 (1,843)	15,379 (2,206)
R_{merge}	10.7 (0.715)	0.084 (0.614)
$R_{p.i.m.}$[a]	0.045 (0.303)	0.044 (0.323)
$I / \sigma (I)$	11.2 (2.3)	14.2 (3.1)
Multiplicity	6.6 (6.4)	4.5 (8.6)[a]
Completeness (%)	99.8 (99.5)	99.7 (100)[a]
Refinement Statistics		
Resolution (Å)	55.4 – 2.78	
R_{work} / R_{free} (%)[b]	20.3 / 26.4	
No. protein chains	2	
No. atoms		
Protein	3,083	
Other (not solvent)	10	
Water	15	
B-factor (Å^2)		
Protein	70.0	
Other (not solvent)	52.2	
Water	50.7	
Ramachandran Plot		
Preferred (%)	93.4	
Allowed (%)	6.6	
Outliers (%)	0	
RMSD Bond (Å)	0.009	
RMSD Angle (°)	1.56	
PDB identification code	8ZLD	

[a] Calculated for equivalent reflections (within I^+ or I^-).

Figure 1 – Figure supplement 3. X-ray crystallographic data collection and structure refinement statistics for PfHO. Statistical values given in parentheses refer to the highest resolution bin.

A.

```
PfHO    ------MIRKIII-LMFTFFS--NIHNEKIYHHKQRRKFLKGPLGYLNRNVIQKKHYNLYAKKFINYKEIQIQRINDYRKRSGVDKNNINYNLRDTYNYHETHL   95
GmHO1   ---MASSLSTIALFLPQSLYIKPRLAPRPLPPPQFRSLFLTSPAGARTATVMPRRAAVI-VS----------AATAETPKKKGESK-----------GFVEEMR   79
AtHO1   MAYLAPISSSL------SIFKNPQLSRFQFSSSSPNPLFLRPRIQILS-MTMNKSPSLVVVAAT-------TAAEKQKKRYPGESK-----------GFVEEMR   79
                                                **                                          *  *             *

PfHO    FVRNEVLPTLAKIENENLKEKEK--NKEIFRNINDYNSNFTRQTFLQFLMDLYNIFLKIDDLFLENKTYFSILIYNGPMQLTNHLYDDIIYVSSVVENSDDVSP   197
GmHO1   FVAMRLH------TRDQAREGEKEVKQPEEKAVTKWD--PSVEGYLKFLVDSKLVYDTLEKIVQEAPHPSYAEFRNTGLERSASLAEDLEWFKEQ--GYTIPEP   173
AtHO1   FVAMRLH------TKDQAKEGEKETKSIEERPVAKWE--PTVEGYLRFLVDSKLVYDTLELIIQDSNFPTYAEFKNTGLERAEKLSTDLEWFKEQ--GYEIPEP   173
        **                *                                                      *        *  *               *

PfHO    SEYCMEYISHLENLCEENKLSFLAHAYVFYKNFHLSKEHLLKSICKYLNIIKKLKSSTY----VADVENFEFCLNKMSRKWSRWEKDNFLASLHNATNK-----   292
GmHO1   SSPGLTYAQYLKELSVKDPQAFICHFYNIYFAHSAGGRMIGKKVAEKLLNNKALEFYKWDDDLPRLLQNVRDKLNKVAEPWSREEKDHCLEETEKSFKLSGEIL   277
AtHO1   TAPGKTYSQYLKELAEKDPQAFICHFYNIYFAHSAGGRMIGRKVAERILDNKELEFYKWDGELSQLLQNVREKLNKVAEEWTREEKNHCLEETEKSFKYSGEIL   277
             *   *  *       *  * *  *                    * *             *    ***    * * **   *

PfHO    MMILTKHFEKVKS              305
GmHO1   RLILS--------              282
AtHO1   RLILS--------              282
          **
```

B.

	% Identity	
	N-term	HO
Babesia	20%	33%
Theileria	17%	33%
SynHO	-	15%
HuHO1	-	16%
AtHO1	8%	14%
GmHO1	13%	17%

C.

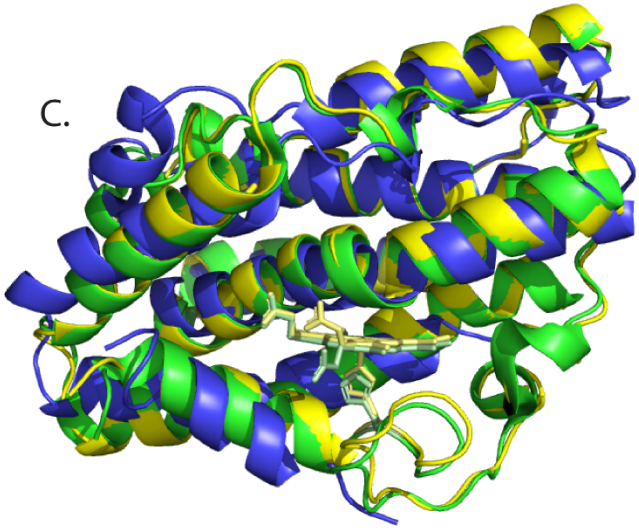

Figure 1 - Figure supplement 4. Sequence and structural alignment of PfHO and plant HOs. A) Sequence alignment of PfHO with *Arabidopsis thaliana* (O48782) and *Glycine max* (C6THA4) HO1s (Uniprot ID). Heme-coordinating histidine and distal helix glycines in plant HOs are highlighted in red. B) Sequence identity of PfHO with proteins identified in our sequence homology analysis showing N-terminal targeting sequence and HO-domain separately. C) Structural alignment of the 2.8 Å-resolution PfHO crystal structure (blue, PDB: 8ZLD) with X-ray structures of *A. thaliana* HO1 (green, PDB: 7EQH) and *G. max* HO1 (yellow, PDB: 7CKA).

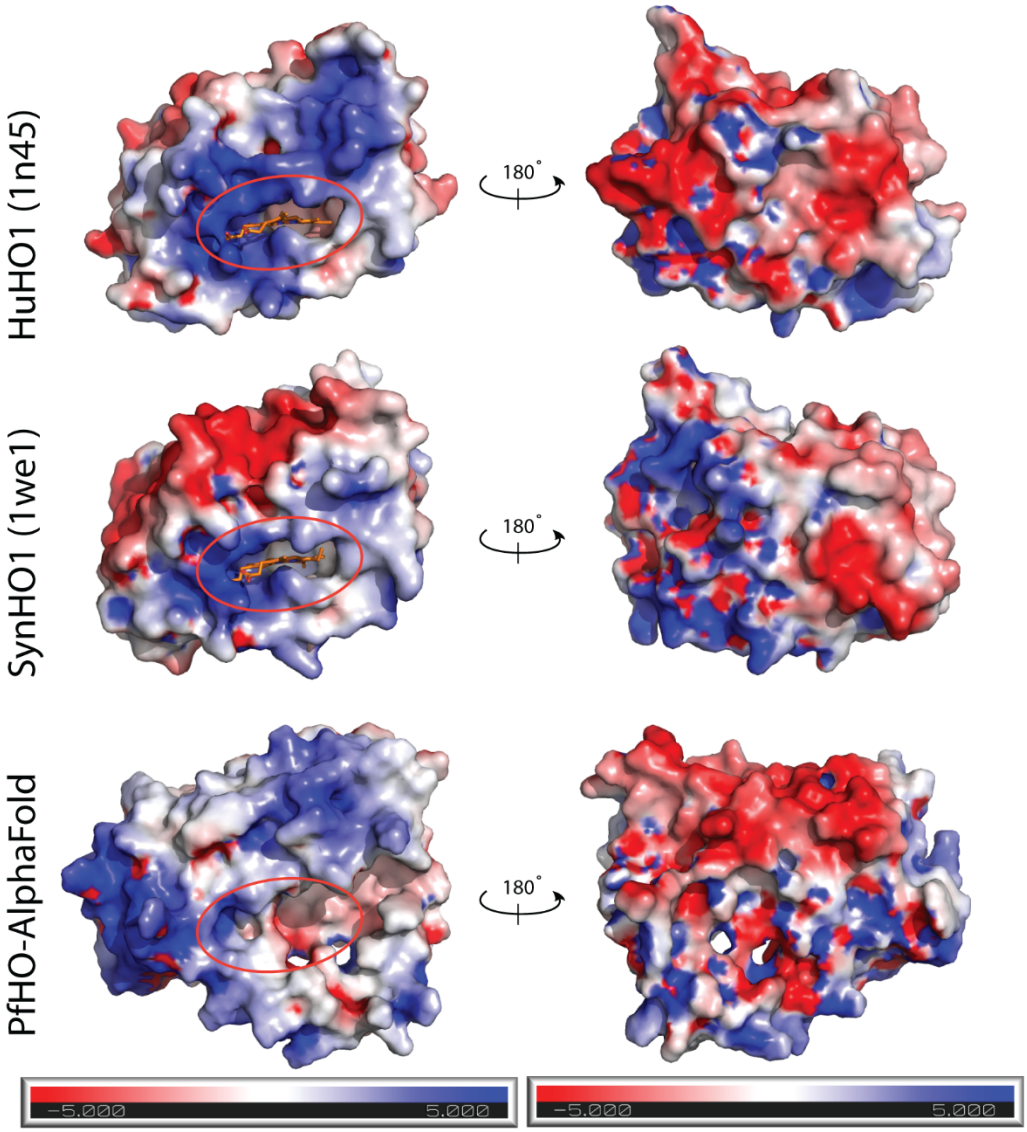

Figure 1 – Figure supplement 5. HO surface charge features. Electrostatic surface potential maps calculated for human HO1 (PDB 1N45), SynHO1 (PDB 1WE1), and the AlphaFold-predicted structure for PfHO (HO domain only) and contoured at ±5 kT/e. Calculations were performed using the APBS PDB2PQR online software suite[4].

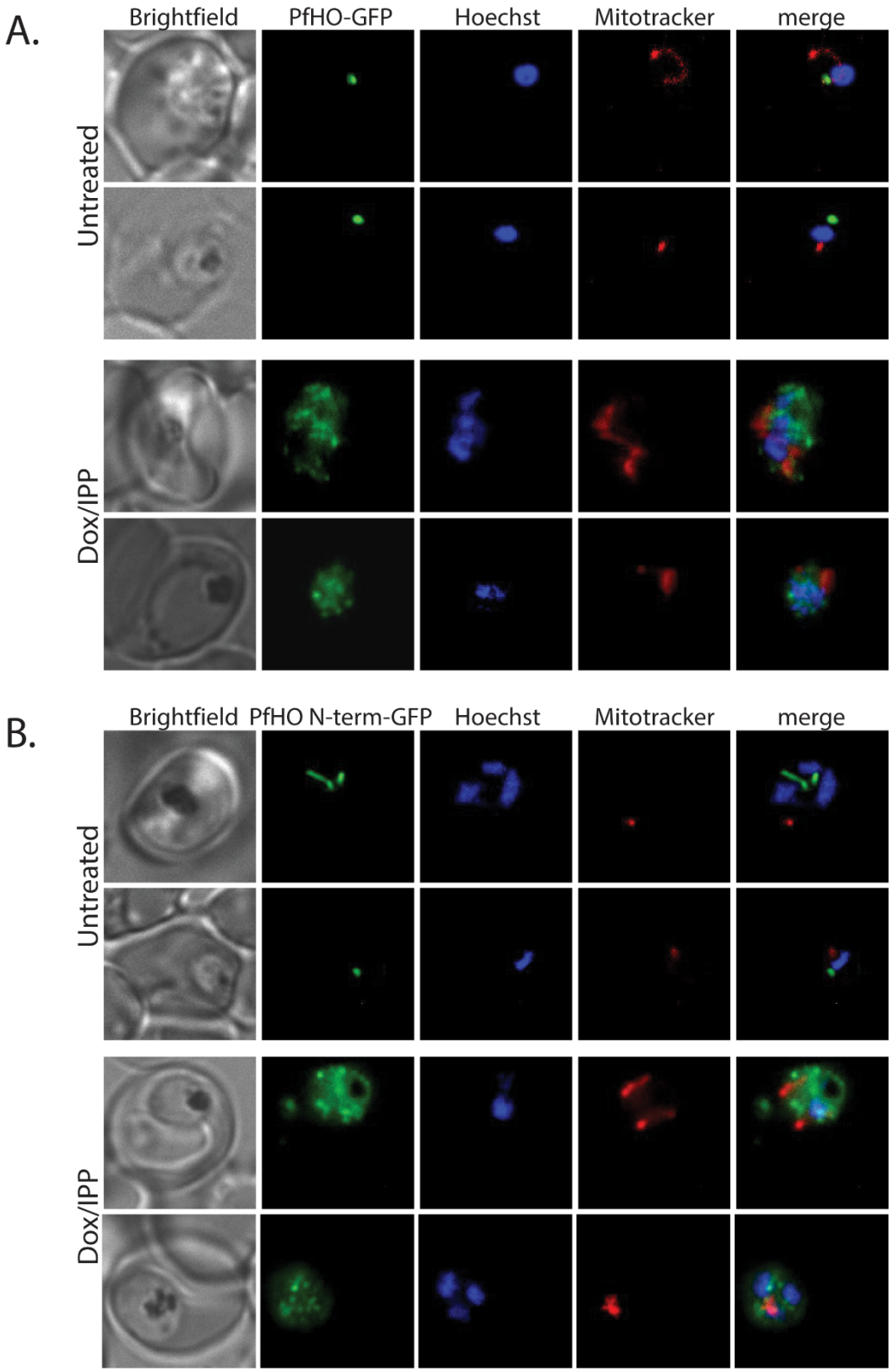

Figure 2 – Figure supplement 1. Additional widefield fluorescence microscopy of live, untreated or Dox/IPP-treated Dd2 parasites episomally expressing (A) PfHO-GFP or (B) PfHO N-term-GFP and stained with 25 nM Mitotracker Red and 10 nM Hoechst.

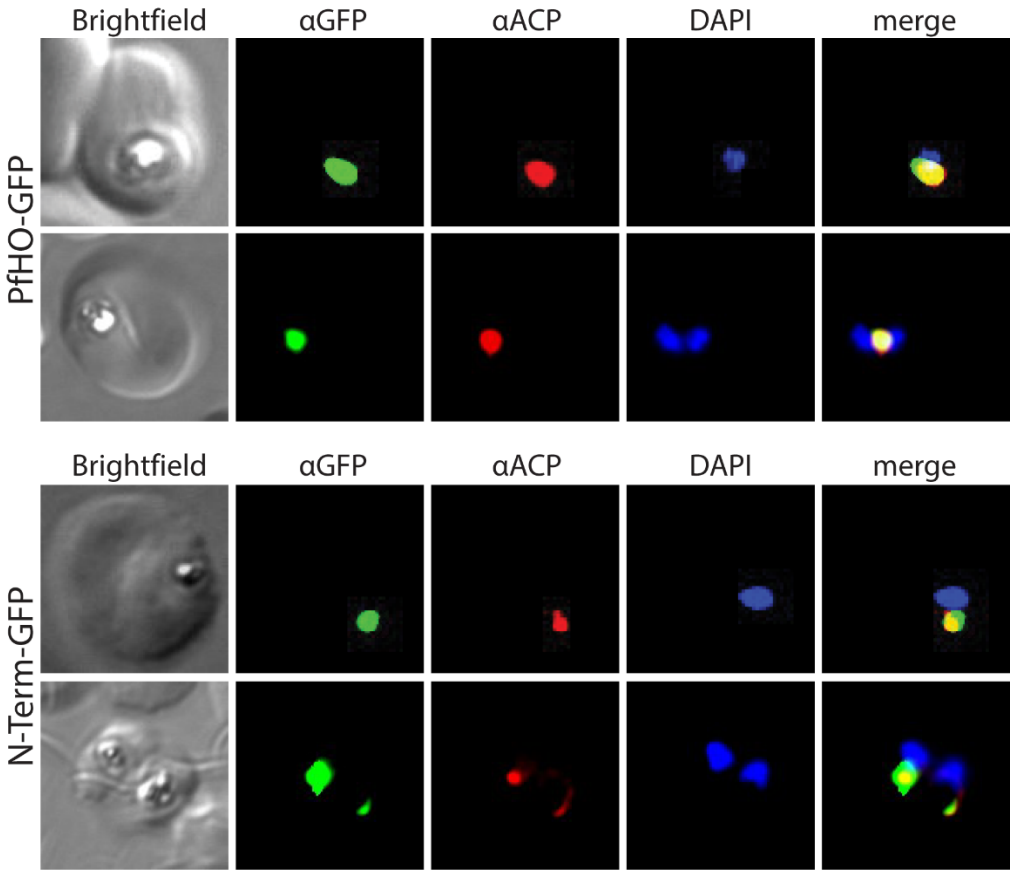

Figure 2 – Figure supplement 2. Additional widefield immunofluorescence microscopy of fixed Dd2 parasites episomally expressing PfHO-GFP and PfHO N-Term-GFP and stained with anti-GFP and anti-apicoplast acyl carrier protein (ACP) antibodies, and DAPI.

Figure 2 – Source Data 1. Uncropped western blots of untreated or Dox/IPP-treated parasites episomally expressing PfHO-GFP, stained with goat anti-GFP primary and anti-goat-IRDye800 secondary antibodies, and visualized on a Licor CLx imager.

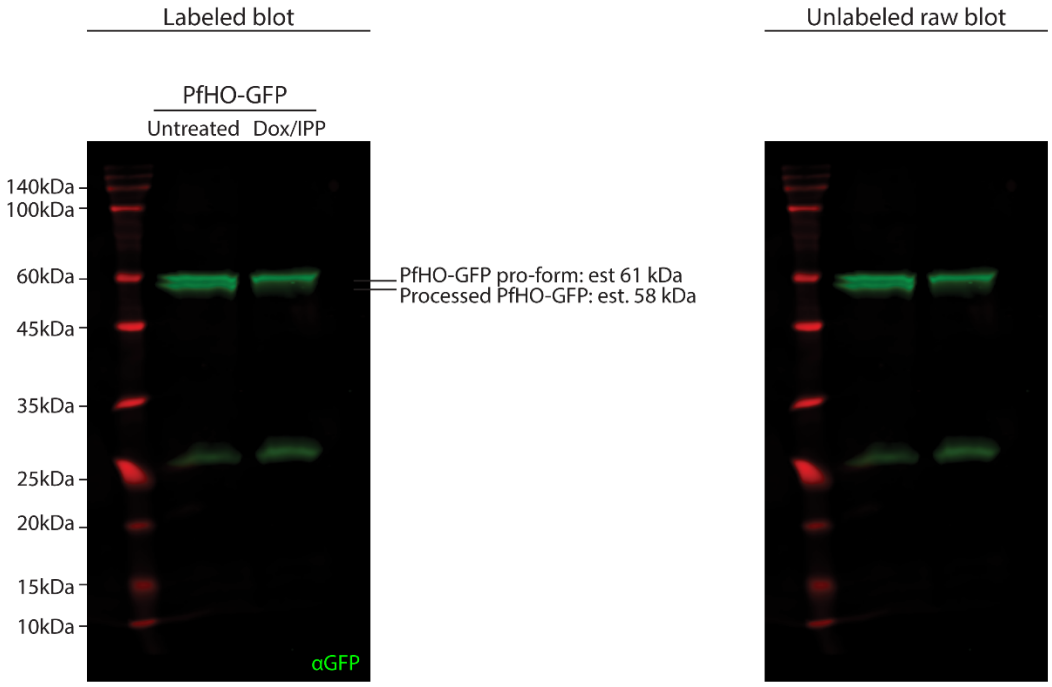

Figure 2 – Source Data 2. Uncropped western blots of untreated parasites episomally expressing PfHO N-term(1-83)-GFP, stained with goat anti-GFP and mouse anti-hDHFR primary antibodies and anti-goat-IRDye800 and anti-mouse-IRDye680 secondary antibodies, then visualized on a Licor CLx imager.

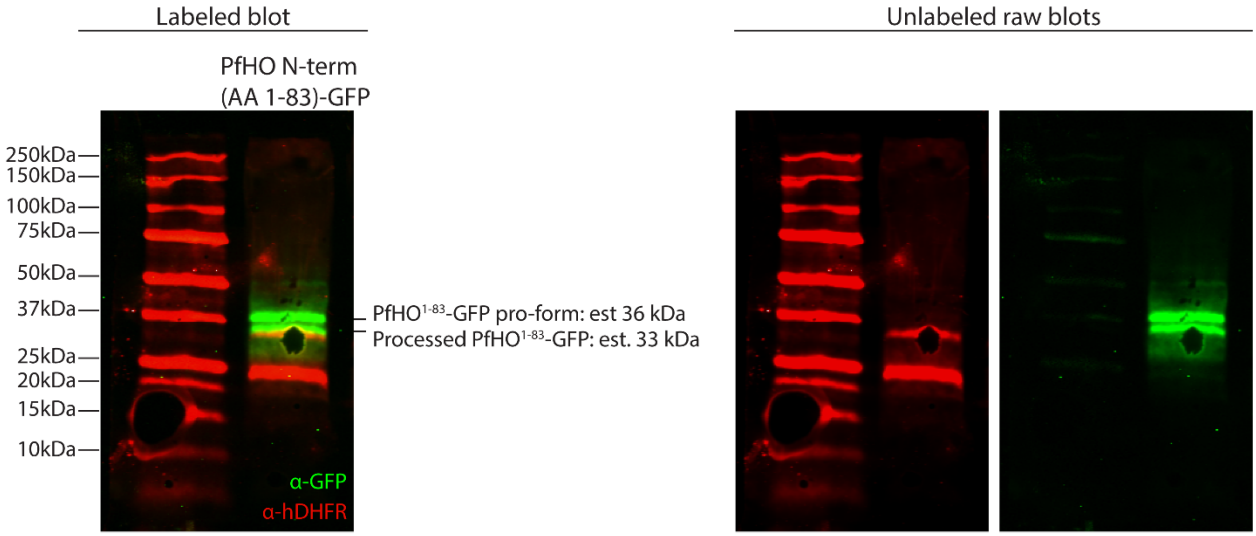

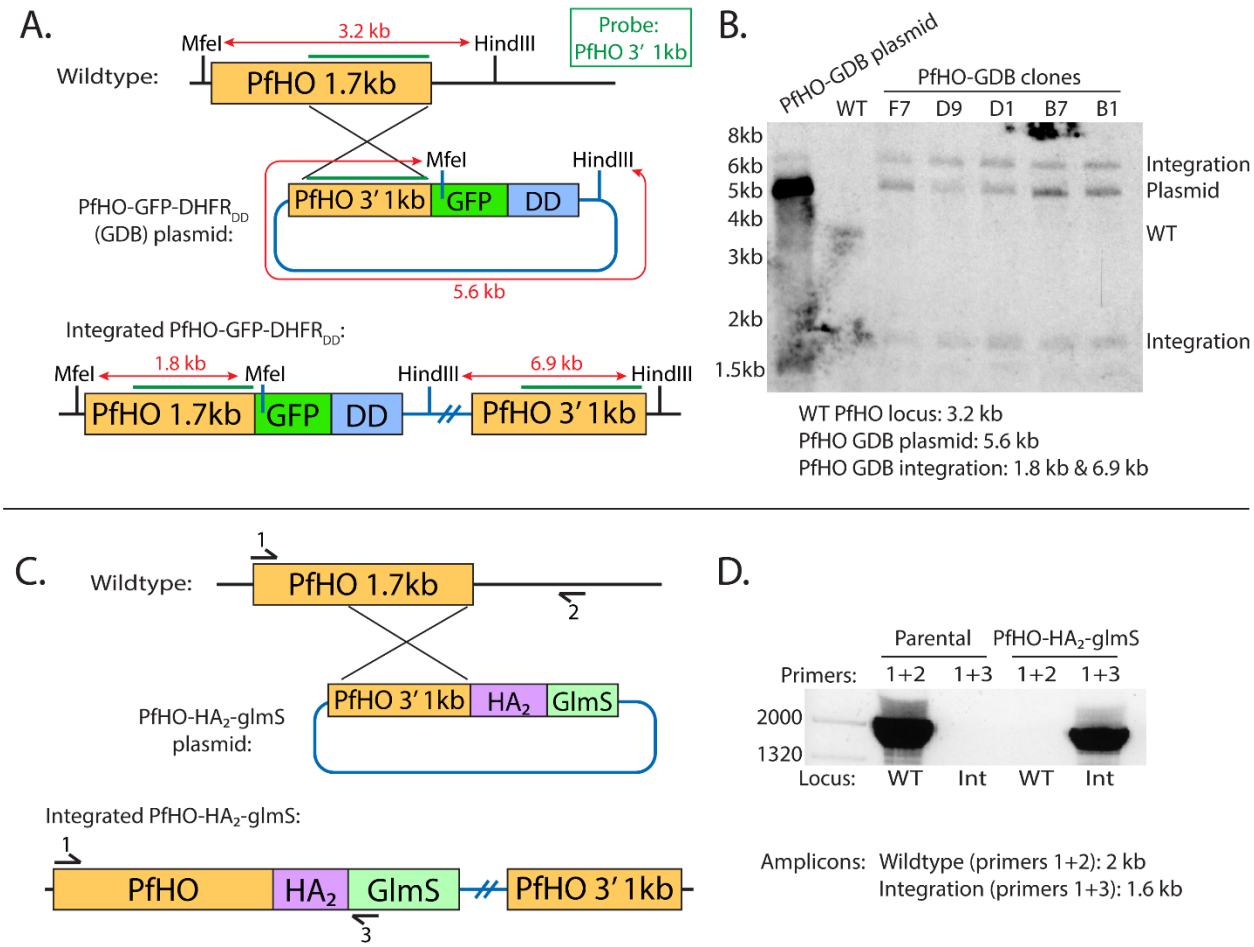

Figure 3 – Figure supplement 1. Schemes for modification of the PfHO genomic locus to integrate C-terminal GFP-DHFR$_{DD}$ or HA$_2$-glmS tags. A) Schematic of single-crossover strategy for tagging PfHO gene locus with C-terminal GFP-DHFR$_{DD}$. 1kb sequence at 3' of PfHO coding region (green line) was used as a probe to test for integration by Southern blot, and enzyme digestion sites with expected sizes are indicated. B) Southern blot of digested parasite DNA harvested from wildtype, polyclonal PfHO-GFP-DHFR$_{DD}$, and select clonal PfHO-GFP-DHFR$_{DD}$ cultures. C) Schematic of single-crossover integration strategy for tagging PfHO gene locus with C-terminal HA$_2$-glmS. Primer sites used to probe integration by genome PCR are indicated. D) Genome PCR of parasite DNA harvested from wildtype parental and PfHO- HA$_2$-glmS cultures.

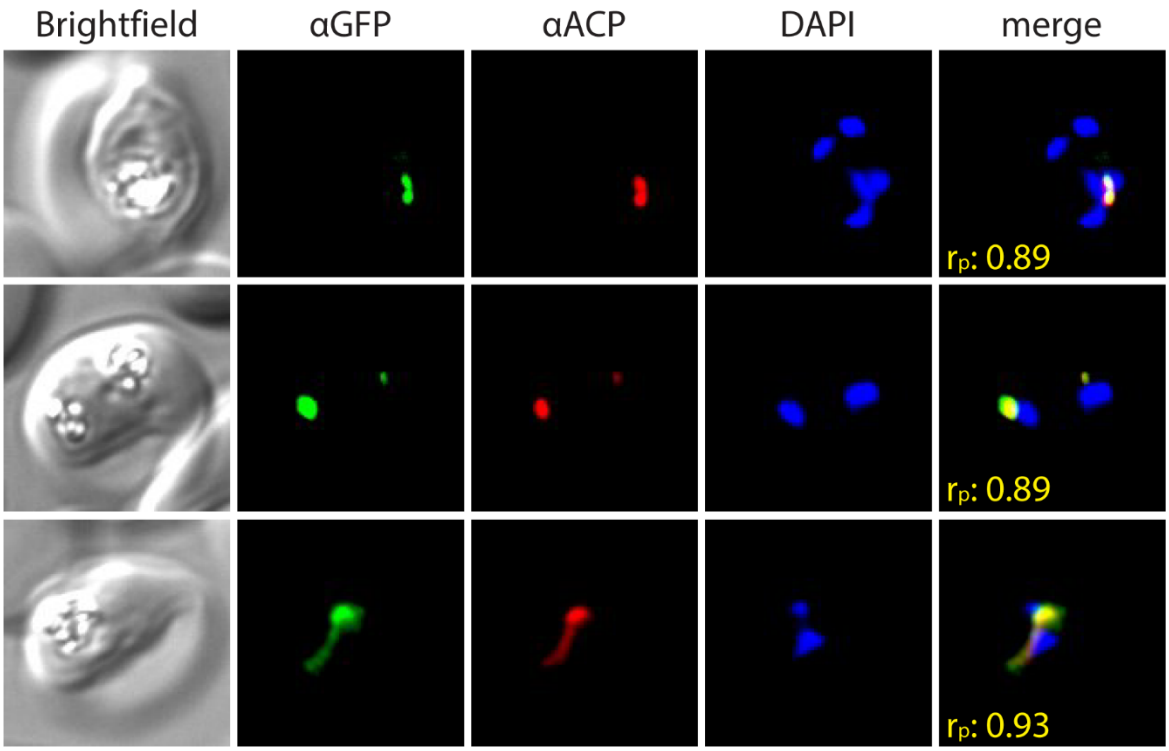

Figure 3 – Figure supplement 2. Widefield immunofluorescence microscopy of fixed 3D7 parasites endogenously expressing PfHO-GFP-DHFR$_{DD}$ and stained with anti-GFP and anti-apicoplast acyl carrier protein (ACP) antibodies, and DAPI. Pearson correlation coefficient (r_p) of red and green channels is shown in merged images in yellow.

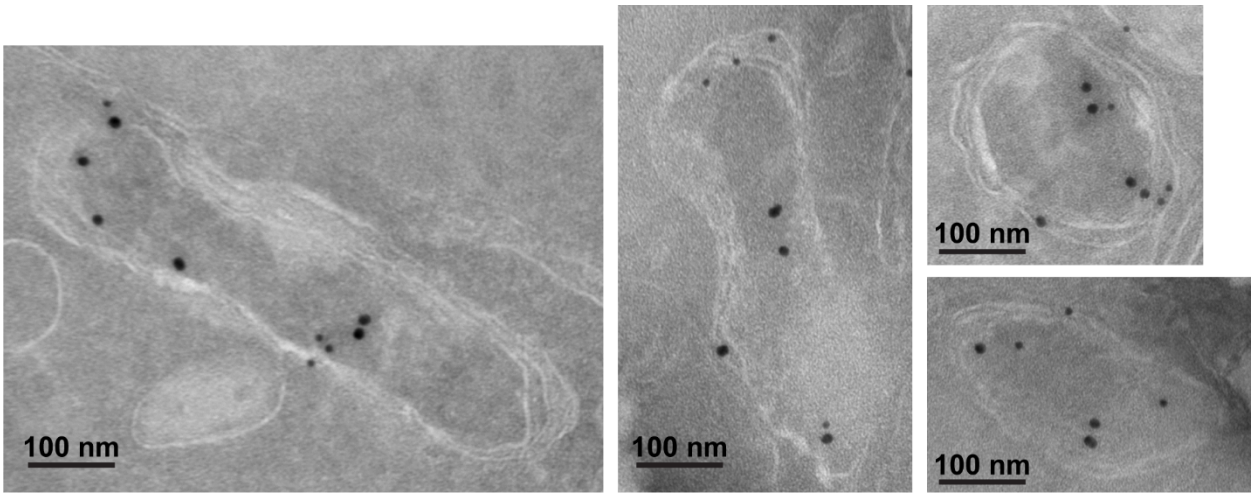

Figure 3 – Figure supplement 3. Additional immunogold transmission electron microscopy images of apicoplasts from fixed 3D7 parasite endogenously expressing PfHO-GFP-DHFR$_{DD}$ and stained with anti-GFP (12 nM, green arrows) and anti-apicoplast ACP (18 nM) antibodies.

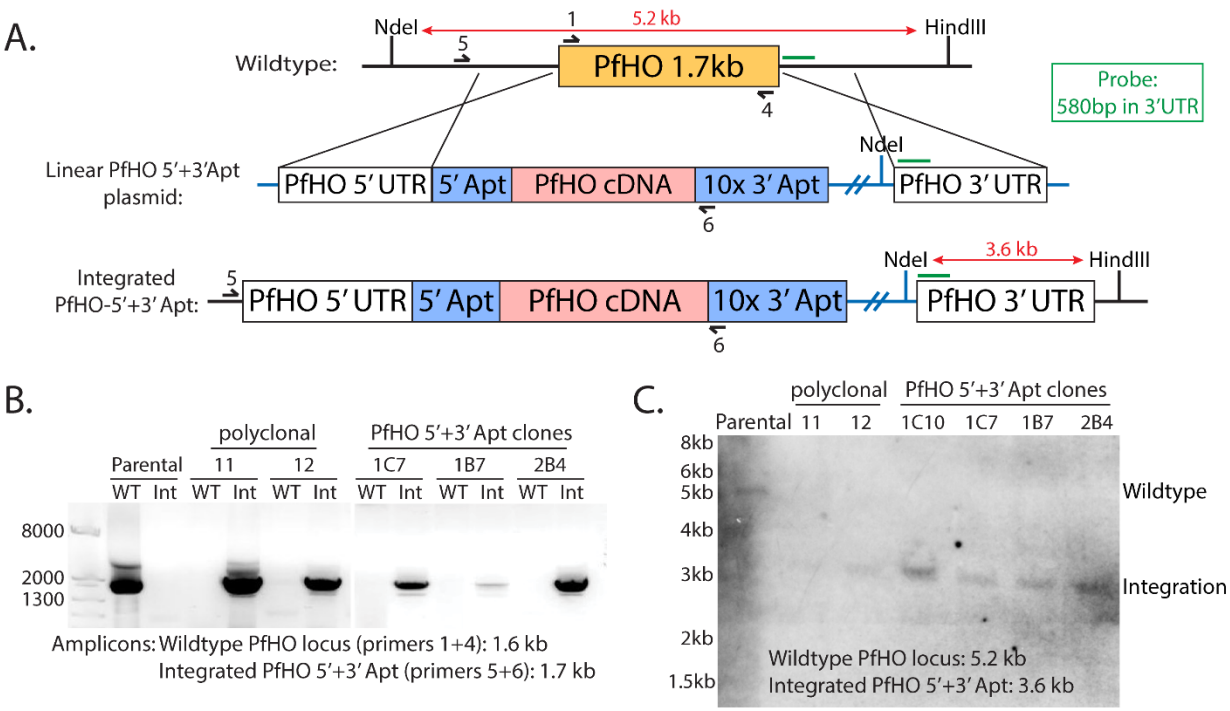

D. PfHO cDNA (*T. gondii* codon bias)

```
ATGATCCGCAAGATTATCATTTTGATGTTCACGTTCTTCAGTAACATCCATAACGAAAAAATTTACCATCACAAACAGCGCCGAAAGTTTCTCAAGGGCCCTC
TCGGCTACCTTAACCGGAACGTGATCCAGAAGAAACATTATAACTTGTACGCGAAAAAGTTTATCAACTACAAGGAGATCCAGATCCAGAGGATCAACGACTA
CCGTAAAAGGTCTGGAGTCGATAAGAATAATATTAATTACAACCTCCGGGACACTTACAACTACCACGAGACCCACCTCTTTGTGCGGAACGAGGTGCTGCCG
ACGCTCGCAAAGATCGAAAACGAAAACCTTAAAGAAAAGGAGAAGAACAAGGAAATCTTCCGAAATATCAATGACTACAATAGTAACTTTACGCGCCAGACTT
TCCTGCAATTCCTCATGGACCTCTACAATATCTTTCTTAAAATCGACGACCTGTTCCTCGAGAATAAGACTTACTTTTCCATCCTCATCTACAACGGGCCGAT
GCAGCTCACGAACCACCTGTACGACGACATTATTTACGTCAGTTCTGTTGTGGAGAATTCGGATGATGTCTCGCCGTCGGAGTACTGTATGGAGTACATCTCT
CATCTCGAAAACCTCTGCGAGGAGAACAAGTTGAGCTTTCTGGCTCACGCATACGTCTTCTACAAGAACTTCCATCTCTCCAAGGAACACTTGCTGAAGTCGA
TCTGCAAATATCTGAACATTATCAAAAAGCTCAAGAGTTCCACTTACGTTGCGGACGTTGAGAATTTTGAATTCTGCTTGAACAAAATGTCTCGCAAGTGGTC
TAGATGGGAAAAGGACAACTTTCTCGCAAGTCTGCATAACGCGACTAATAAGATGATGATCCTCACTAAGCATTTCGAAAAGGTGAAATCTTGA
```

Figure 3 – Figure supplement 4. Scheme for modification of the PfHO genomic locus to integrate the aptamer/TetR-DOZI system. A) Schematic of double-crossover integration strategy for replacing PfHO gene with cDNA encoding PfHO (*Toxoplasma gondii* codon bias) and RNA aptamers at the 5' and 3' ends of the gene. 580 bp sequence in 3' UTR of PfHO (green line) was used as a probe to test for integration by Southern blot, and enzyme digestion sites with expected sizes marked on locus and plasmid. Primers used to probe integration by genome PCR are marked on wildtype and tagged loci. B) Genome PCR of parasite DNA harvested from wildtype parental, polyclonal PfHO-aptamer/TetR-DOZI, and select PfHO-aptamer/TetR-DOZI clonal cultures. C) Southern blot of digested parasite DNA harvested from wildtype, polyclonal PfHO-aptamer/TetR-DOZI, and select clonal PfHO-aptamer/TetR-DOZI cultures. D) Complete PfHO cDNA sequence used to replace the endogenous PfHO gene (identical encoded protein sequence).

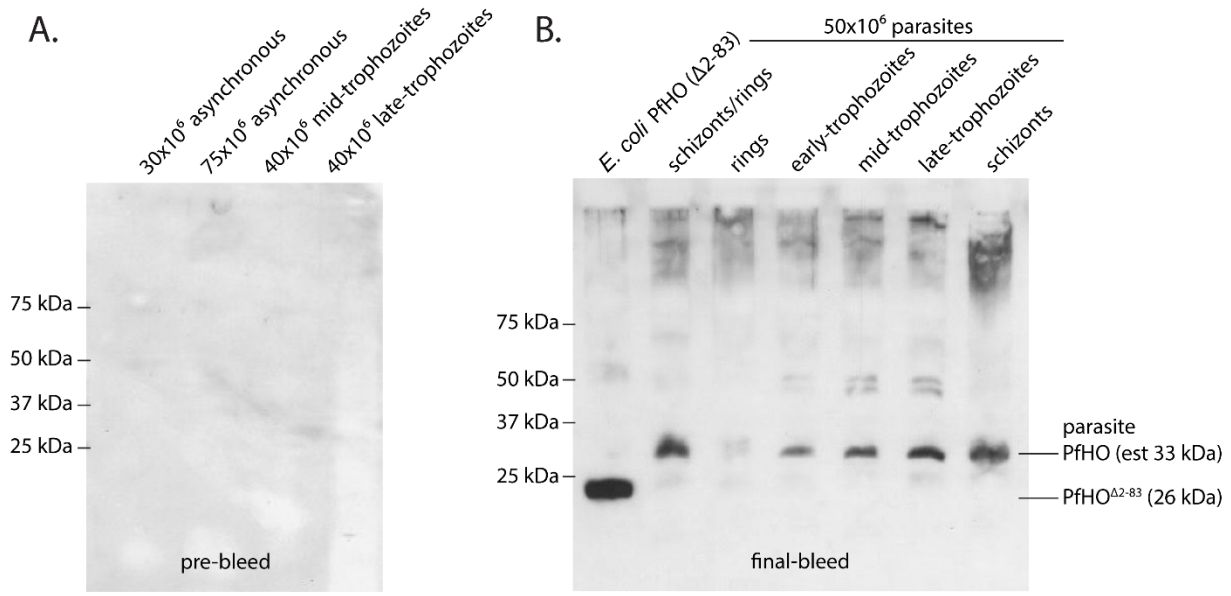

Figure 3 – Figure supplement 5. Validation of custom PfHO antibody specificity. Western blot specificity tests of custom PfHO rabbit antibody in parasite lysates. A) Lysates from asynchronous or synchronous parasite cultures stained with 1:1,000 dilution of rabbit serum prior to inoculation with PfHO protein antigen. B) Lysates from *E. coli* expressing $PfHO^{84\text{-}305}$ and from equal numbers of synchronous 3D7 parasites stained with 1:1,000 dilution of crude serum from the final bleed of a rabbit inoculated with PfHO protein antigen. Both blots were stained with an anti-rabbit HRP secondary antibody and visualized by chemiluminescence.

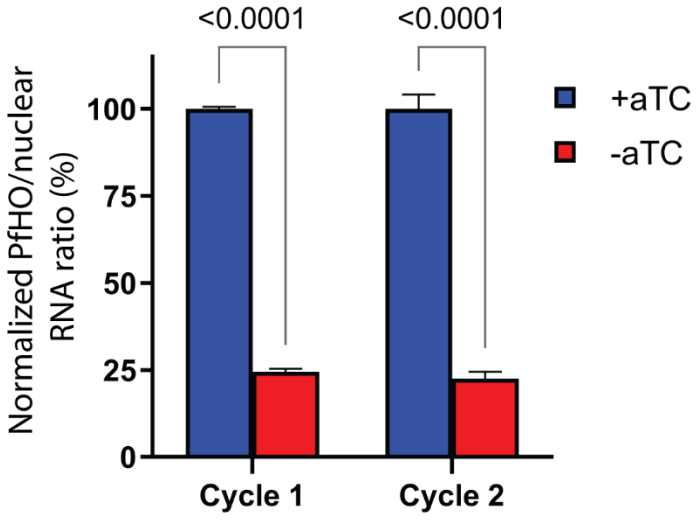

Figure 3 – Figure supplement 6. Quantitative PCR of PfHO expression ±aTC with 200 µM IPP. Transcript levels of endogenous PfHO from PfHO-aptamer/TetR-DOZI parasites grown 2 or 4 days ±aTC with 200 µM IPP. PfHO transcript abundance is normalized to the average abundance of nuclear-encoded I5P (Pf3D7_0802500), ADSL (Pf3D7_0206700), and STL (Pf3D7_0717700) transcripts, and +aTC is normalized to 100%. Normalized ratios and error bars are the average ±SD of biological triplicates.

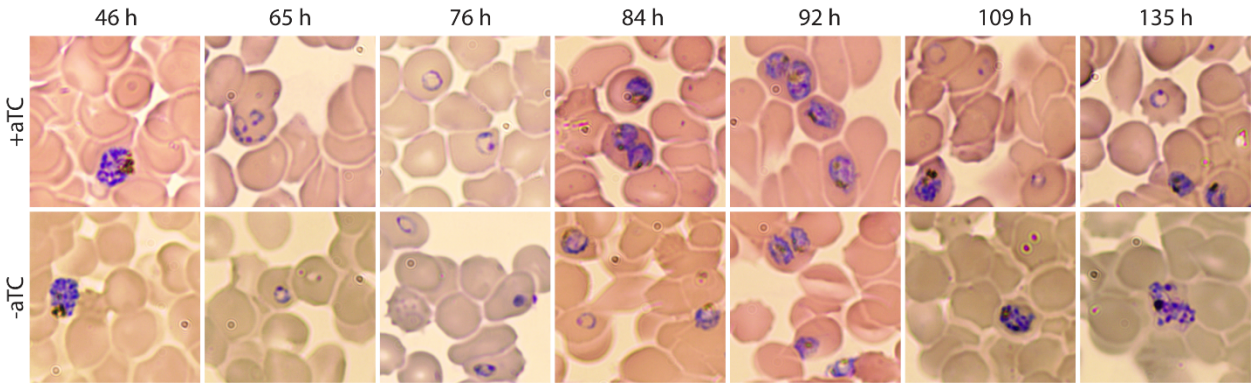

Figure 3 – Figure supplement 7. Giemsa-stained smears of PfHO-aptamer/TetR-DOZI parasites grown in ±aTC. Times indicated are hours post-synchronization.

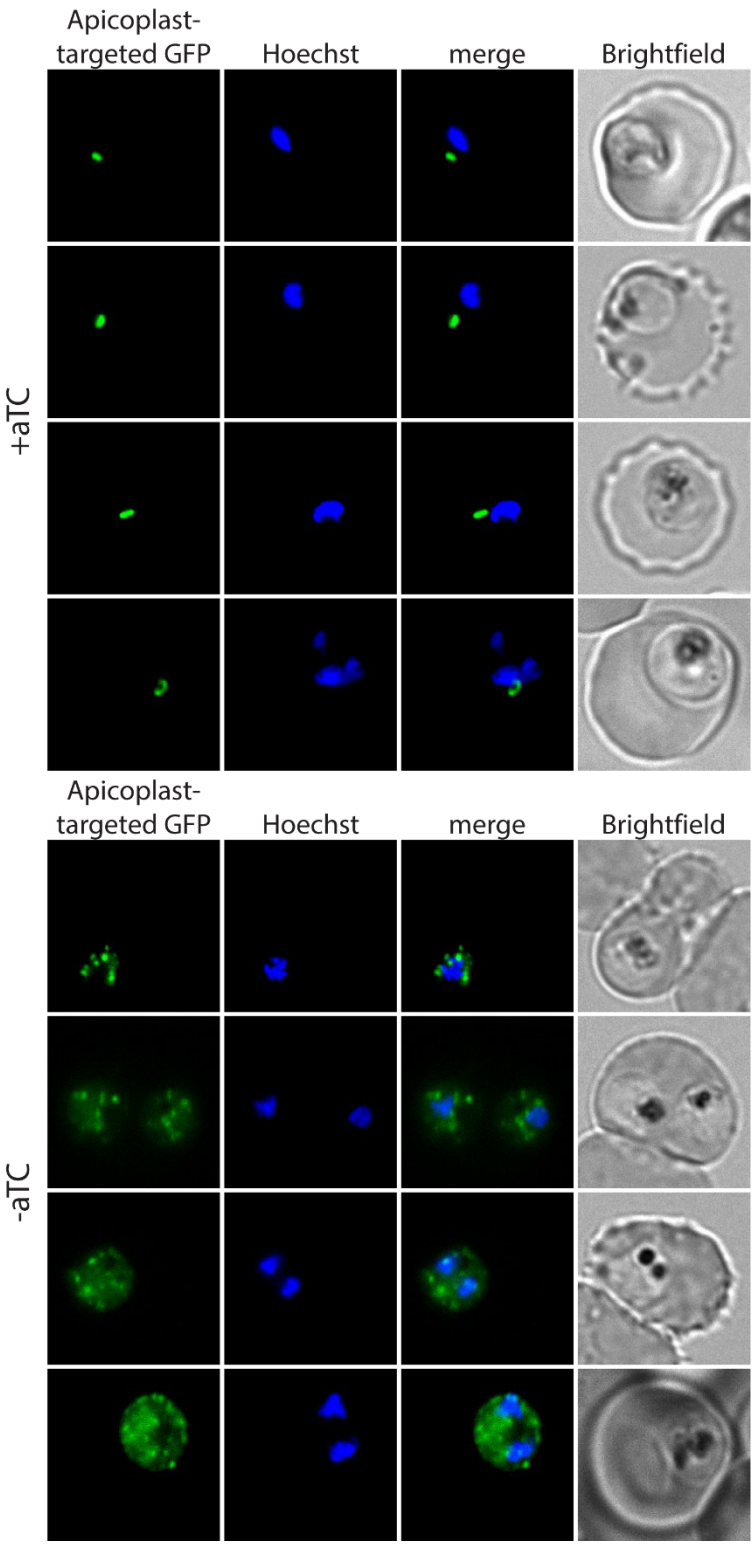

Figure 3 – Figure supplement 8. Additional live-parasite fluorescence microscopy images of apicoplast morphology after PfHO knockdown. PfHO-aptamer/TetR-DOZI parasites episomally expressing apicoplast-localized GFP were grown 5 days ±aTC with 200 µM IPP and stained with 10 nM Hoechst.

Figure 3 – Source data 1. Uncropped western blots of parasites endogenously expressing PfHO-GFP-DHFR$_{DD}$ that were untreated or Dox/IPP-treated for 5 days. Membrane was stained with goat anti-GFP and custom rabbit anti-PfHO primary antibodies then anti-goat-IRDye800 and anti-rabbit IRDye680 secondary antibodies. Stained membrane was visualized on a Licor CLx imager.

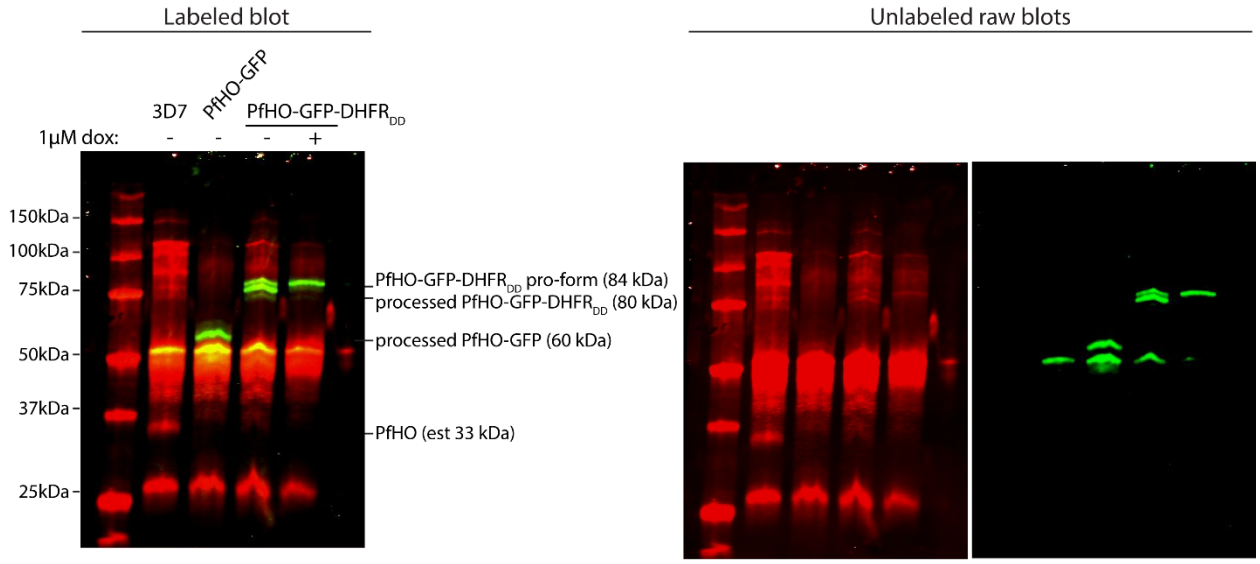

Figure 3 – Source data 2. Uncropped western blots of Dd2 parasites tagged with PfHO-Aptamer/TetR-DOZI grown in +aTC or -aTC/IPP conditions for 7 days, stained with rabbit anti-Ef1α and custom rabbit anti-PfHO primary antibodies and anti-rabbit-IRDye800 secondary antibody. Stained membrane was visualized on a Licor CLx imager.

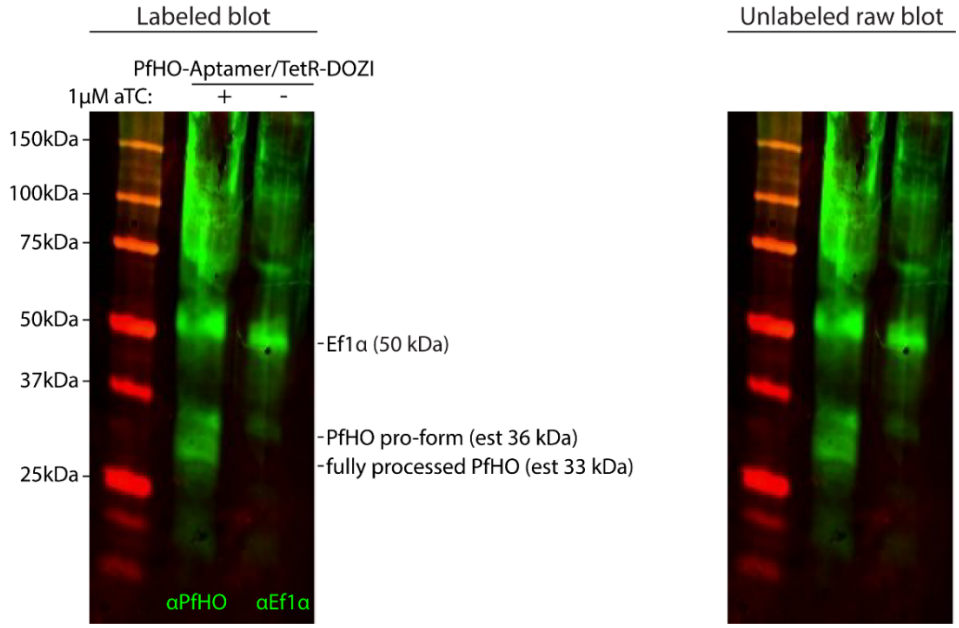

Figure 3 – Source data 3. Uncropped Southern blot of digested parasite DNA harvested from wildtype, polyclonal PfHO-GFP-DHFR$_{DD}$, and select clonal PfHO-GFP-DHFR$_{DD}$ cultures.

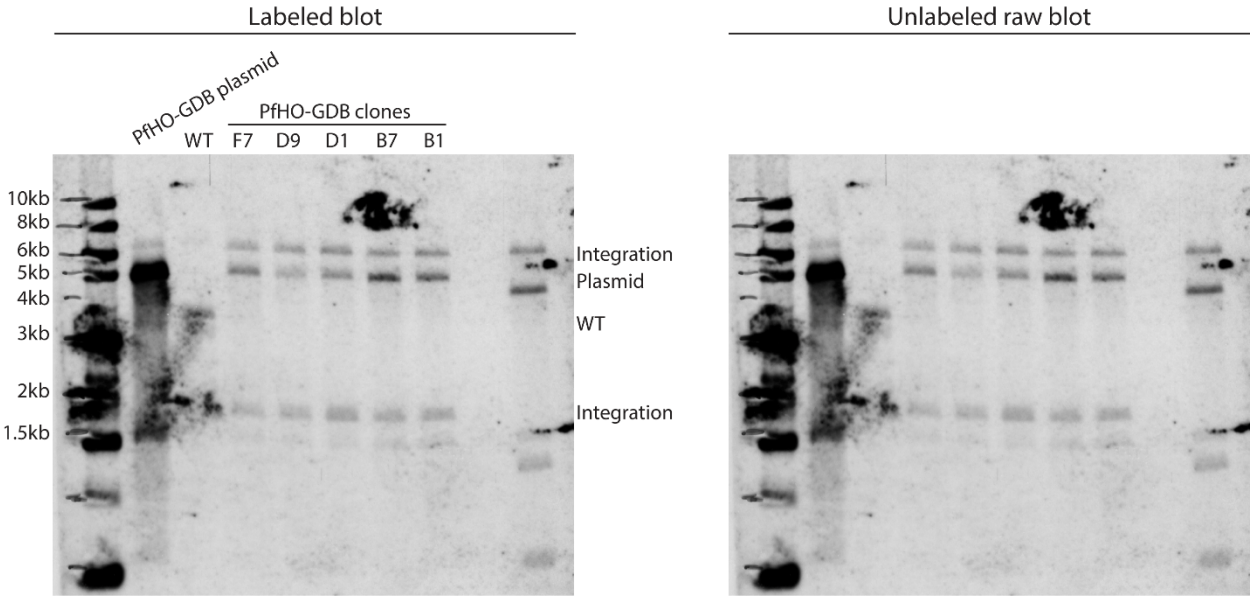

Figure 3 – Source data 4. Uncropped PCR gel of parasite DNA harvested from wildtype parental, polyclonal PfHO- HA$_2$-glmS, and select PfHO-HA$_2$-glmS clonal cultures.

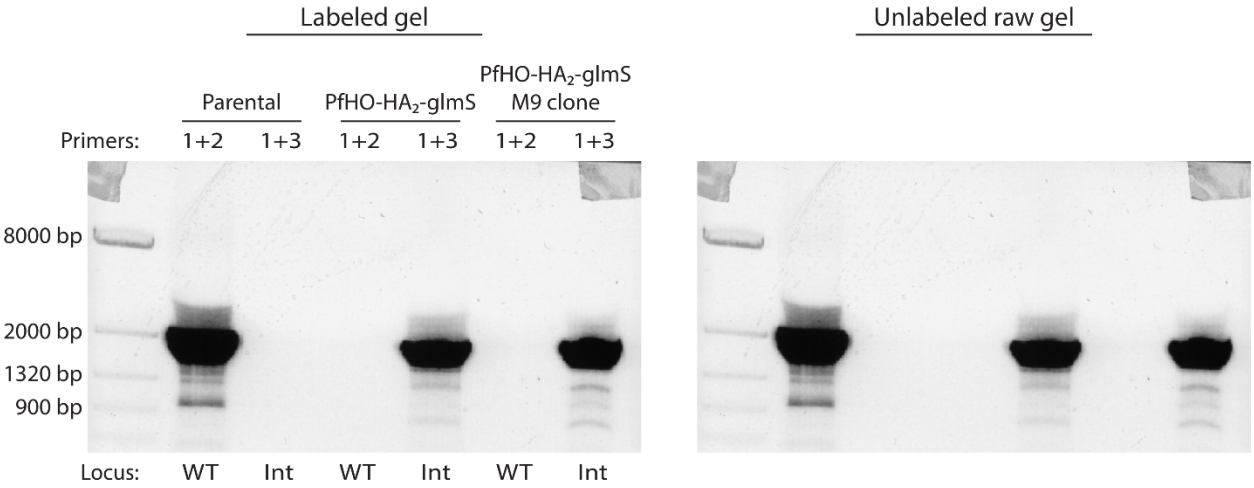

Figure 3 – Source data 5. Uncropped PCR gel of parasite DNA harvested from wildtype parental, polyclonal PfHO-aptamer/TetR-DOZI, and select PfHO-aptamer/TetR-DOZI clonal cultures.

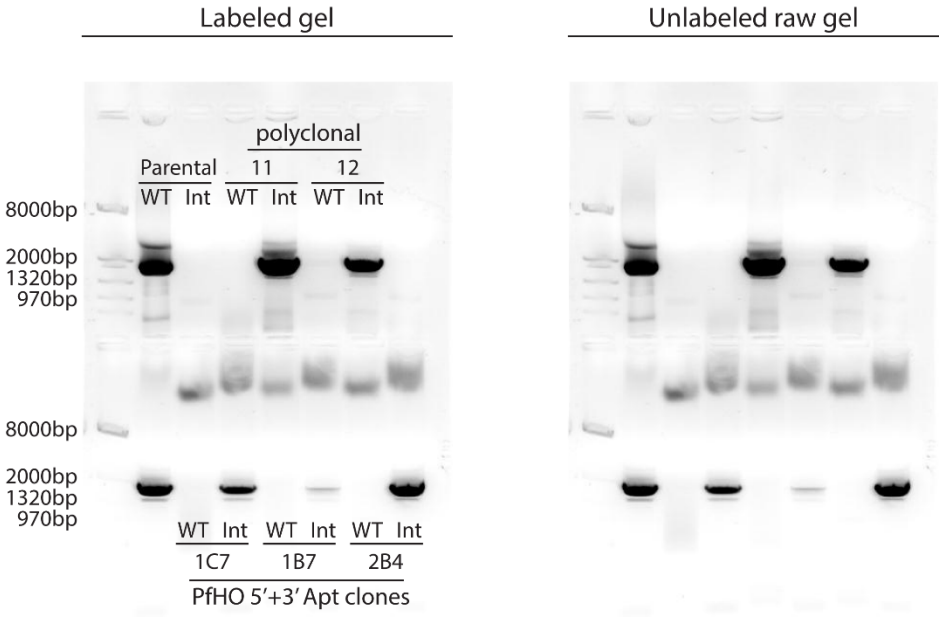

Figure 3 – Source data 6. Uncropped Southern blot of digested parasite DNA harvested from wildtype, polyclonal PfHO-aptamer/TetR-DOZI, and select clonal PfHO-aptamer/TetR-DOZI cultures.

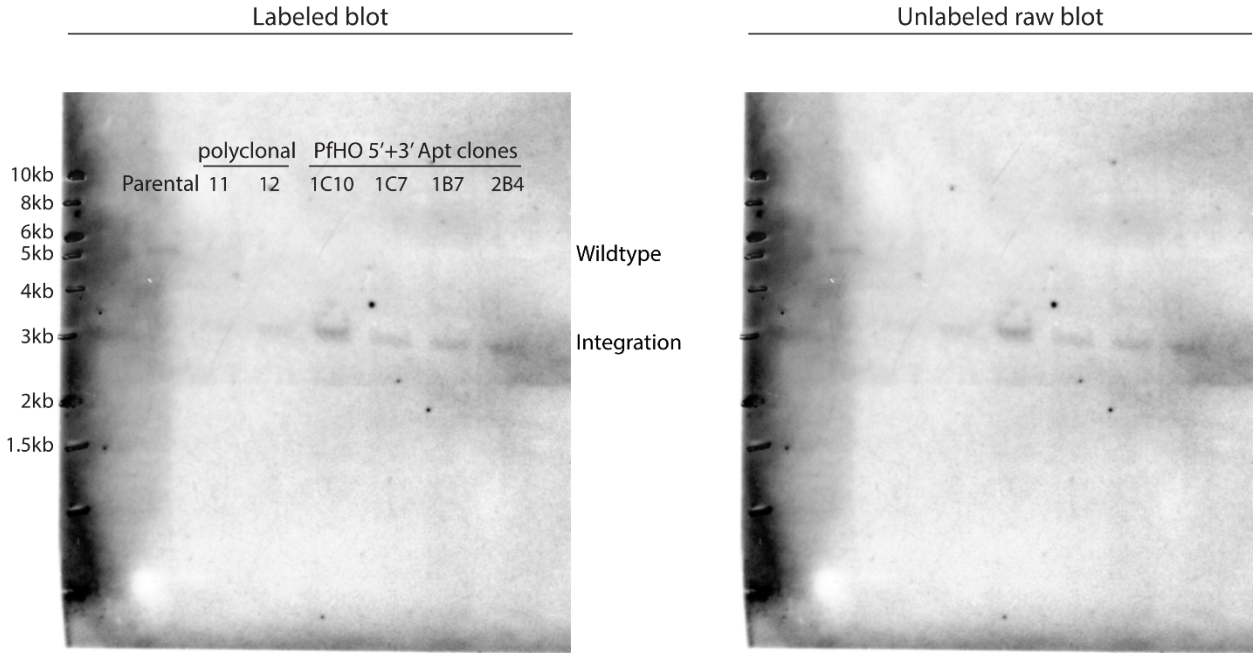

Figure 3 – Source data 7. Uncropped western blot of lysates from asynchronous or synchronous 3D7 parasites stained with 1:1,000 dilution of rabbit serum prior to inoculation with PfHO protein antigen.

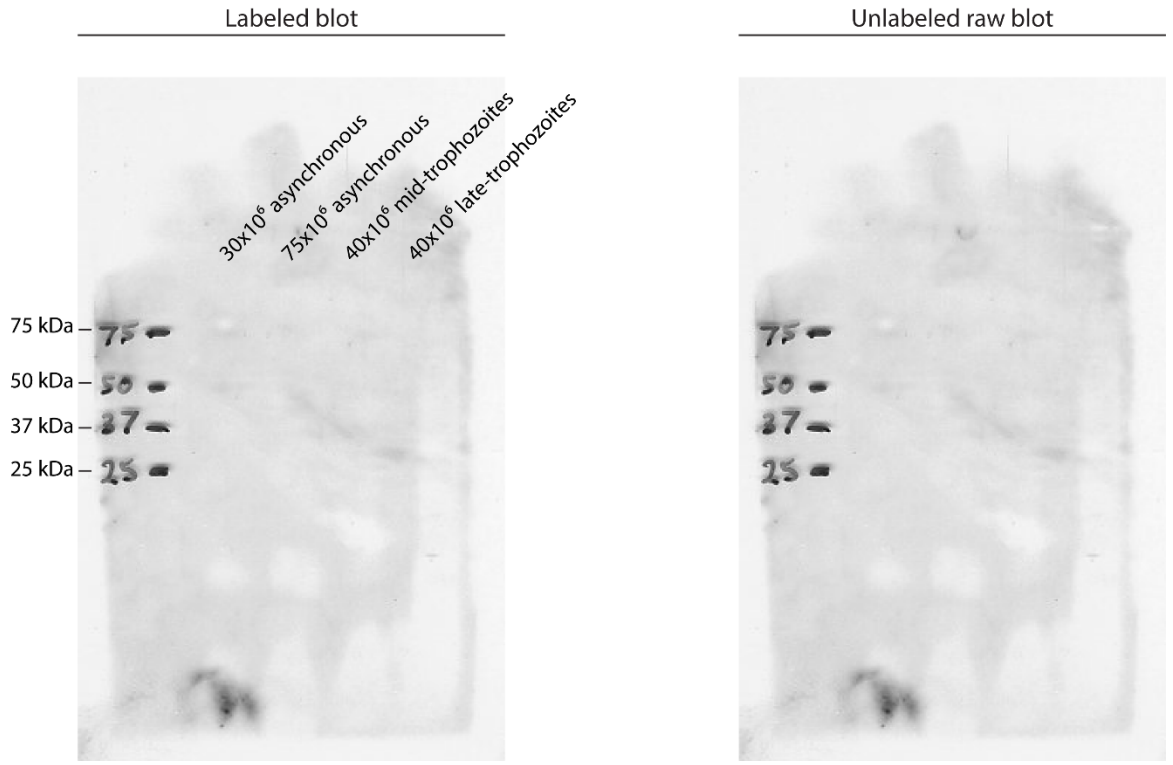

Figure 3 – Source data 8. Uncropped western blot of lysates from *E. coli* expressing PfHO$^{84\text{-}305}$ and from equal numbers of synchronous 3D7 parasites stained with 1:1,000 dilution of crude serum from the final bleed of a rabbit inoculated with PfHO protein antigen.

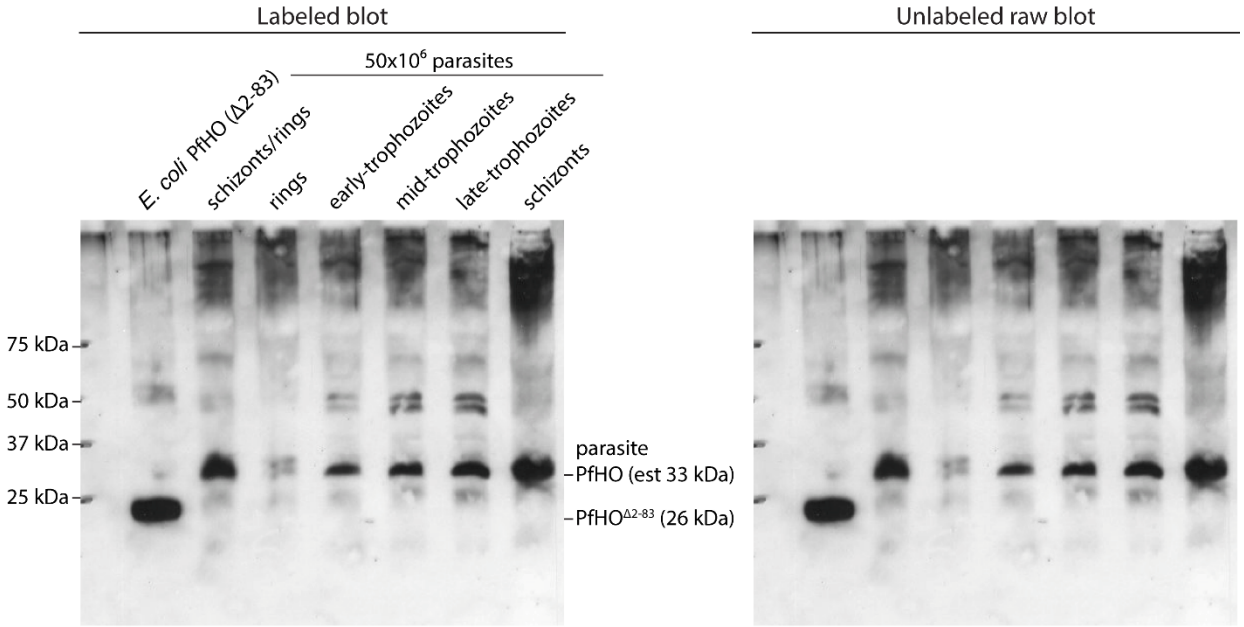

PfHO N-Term (1-83)

MIRKIIILMFTFFSNIHNEKIYHHKQRRKFLKGPLGYLNRNVIQKKHYNLYAKKFI
NYKEIQIQRINDYRKRSGVDKNNINYNLR

PfHO HO-domain (84-305)

DTYNYHETHLFVRNEVLPTLAKIENENLKEKEKNKEIFRNINDYNSNFTRQTFLQF
LMDLYNIFLKIDDLFLENKTYFSILIYNGPMQLTNHLYDDIIYVSSVVENSDDVSP
SEYCMEYISHLENLCEENKLSFLAHAYVFYKNFHLSKEHLLKSICKYLNIIKKLKS
STYVADVENFEFCLNKMSRKWSRWEKDNFLASLHNATNKMMILTKHFEKVKS

Peptides:

PfHO N-Term (1-83)	PfHO HO-domain (84-305)	
K.GPLGYLNR	R.DTYNYHETHLFVR	Y.VSSVVENSDDVSPSEYC
K.HYNLYAK	Y.NYHETHLFV	Y.VFYKNFH
K.KFINYK	R.NEVLPTLAK	L.KSICKYL
K.FINYK	K.IENENLK	K.YLNIIK
F.INYKEIQIQRINDYR	K.IENENLKEK	K.SSTYVADVENFEFCLNK
R.INDYR	F.RNINDYNSNFT	Y.VADVENFEFC
R.SGVDKNNINYNLR	R.NINDYNSNFTR	R.WEKDNFLASLHNATNK
K.NNINYNLR	K.IDDLFLENK	K.DNFLASLHNATNK
	F.LENKTYF	K.MMILTK
	L.TNHLYDDIIYV	

Figure 4 – Figure supplement 1. Peptide coverage of PfHO sequence detected by mass spectrometry. A) Red residues correspond to sequence detected by tryptic digest and tandem mass spectrometry after PfHO isolation from parasites. B) List of individual peptides detected within PfHO N-term and HO-domains.

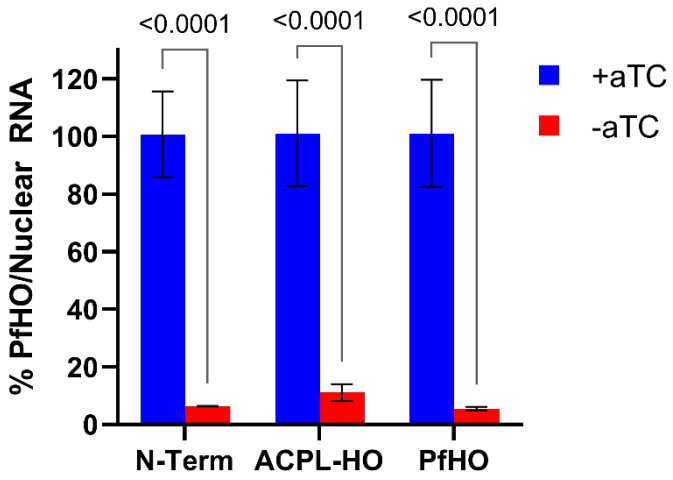

Figure 4 – Figure supplement 2. qPCR analysis of PfHO knockdown in PfHO-aptamer/TetR-DOZI parasites complemented with indicated episomes. Transcript levels of endogenous PfHO from PfHO-Aptamer/TetR-DOZI + episomal complement parasites grown in ±aTC with 200 µM IPP for 5 days. PfHO transcript abundance was normalized to the average abundance of nuclear-encoded I5P (Pf3D7_0802500), ADSL (Pf3D7_0206700), and STL (Pf3D7_0717700) transcripts, and +aTC was normalized to 100%. Normalized ratios and error bars are the average ±SD of biological triplicates.

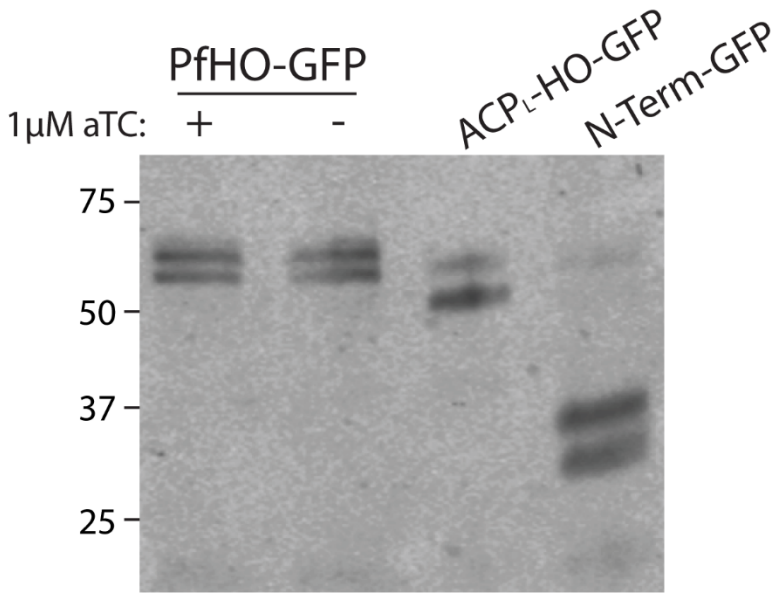

Figure 4 – Figure supplement 3. Western blot of PfHO-aptamer/TetR-DOZI parasites complemented with episomes expressing PfHO-GFP, ACP_L-HO-GFP, or PfHO N-Term-GFP. Membrane was stained with goat anti-GFP primary and anti-goat-HRP secondary antibodies and visualized by chemiluminescence. PfHO-GFP parasites were grown in ±aTC with 200 µM IPP for 5 days prior to lysis.

PfHO N-Term (1-83)

```
PfHO   MIRKIIILMFTFFSNIHNEKIY-HHKQRRKFLKGPLGYLNRNVIQKKHYNLY-AKKFINYKEIQIQRINDYRKRSGVDKNNIN---Y---N   83
ToHO   MYIGVVIATLTIFCDFNVIRCLGLAVESGLAFSPPRPYLRRIKVKNRISRDERKRRSEFSKQLHKELRMKYWRRIDPKINEILKFDD---P   88
BmHO   MHNGQV----NIFLAILYVTMVVGYVPKRATLRPPKPNRKTPKG--P--ILHRREKAKESNQLRDELIMKYWRRVGKEVNEVPFTDQ---S   80
Cvel   ----------------------------------------MIL-----------RSERYV---EELKRRENDILFKPFREHPLCDPFGKK   36
Vbra   -------------------------------------MGAINV-----------GLKEYQ----IMK---RMRIFTK-EQVDAFHDISRK   34
```

PfHO HO-domain (84-305)

```
PfHO   LRDTYNYHETHLFVRNEVLPTLAKIENENLKEKEKNKEIFR-NI------NDYNSNFTRQTFLQFLMDLYNIFLKIDDLFLENKTYFSILI   167
ToHO   LAESYDLDPKRGFVVQEVIPRMVYVSD-SLKP-------LP-LD------ESRSEEFDRQAGLQFLANIAAVTGVFVKEFES-RKGLSFLS   163
BmHO   H--QQHIDTRRAFMSMYVLPKMAEISYKECDI-------LK-LD------EKKSSNFTRHSCLQFLCEIRNFFSVCAHGFNK-NEGLKELV   154
Cvel   HLPEHSFVPKESFINKQVIPKLARLQYELDSNRKITGKSEWLLDEPWGKKDFYKRLPDIEDVKQLLVDIGHIFELFDLICTT-HGEFVPMW   126
Vbra   DWPVSTYVPEQSFVESEMHPVMARIELEEDKLTEEDRKSDPVLAPFYDD---VDRQLTREDFLQSLVDLKHVYEAYDSVIDN-YEMLAPLQ   121

PfHO   YNGPMQLTNHLYDDIIYVSSVVENSDDVSPSEYCMEYISHLENLCEE-NKLSFLAHAYVFYKNFHLSKEHLLKSICKYLNIIKKLKSSTYV   257
ToHO   EMGPSELLTRLETDISYISSLLNVEQ-QSLSRSCLEYVEFLKSLCEK-SEIRFLSQCYVFFKEWHVSKKTLLTNLRDHLRLVNKLKCSFYD   252
BmHO   EMGPINEIPYLSNDITYIRKLINGSG-E-FTTEHGKYIDFLQKIAEN-DPIALVSHAYYFYKEWCLCKFHVLNSIKLHLRITRHFQSAGFN   242
Cvel   TEGPRTKVKKIQADLKAIEEVYGKL--PGTGRWAARYGNFLLGLSRNGELARFLAHYYNWYLEWHMGGPTFFKYLQYYFKIVKRFRMMAWD   215
Vbra   ATGPMTRWAYLEEDIDALTELMGVDA-PEPSEVGAGYGDEIKSIAAR-SQPGVLGHLYNFYKEWDMGGRTVIKSTAARLNIPRNFKLARRD   210

PfHO   ADVENFEFCLNKMSRKWSRWEKDNFLASLHNATNKMM-ILTKHFEKVKS----------------   305
ToHO   PDARNLEGVLNLMASEWTRRQKDEFLNEIPLAYQKLSESLVMPFV--------------------   297
BmHO   EDVLNFEYVLNMLACSWSQVEKDNFLRNLSIASDMAK-CYTQCFT--------------------   286
Cvel   FDSDAAGYMIDYMAVDFTKEEKAQFLAALDEVNDMQSGLQE-YLTPRDKMPDLPS----------   269
Vbra   GDSWNIAATLDVIADKWTPEQKEECLTELSRANQLASQLVT-LLHGTEMEEEEDEEGEEEGGEDK   274
```

Figure 4 – Figure supplement 4. Sequence alignment of alveolate HO-like proteins in *Plasmodium falciparum*, *Theileria orientalis*, *Babesia microti*, *Chromera velia*, and *Vitrella brassicaformis.* Secondary α-helical structure, predicted by AlphaFold structural models, is underlined. Alveolate-specific N-terminal α-helix is underlined in pink.

Figure 4 – Source data 1. Uncropped western blots of parasites endogenously expressing PfHO-HA_2 and lysates from *E. coli* expressing PfHO HO-like domain ($PfHO^{84-305}$-HA_2) stained with rat anti-HA and custom rabbit anti-PfHO primary antibodies and anti-rabbit-IRDye680 and anti-rat-IRDye800 secondary antibodies then visualized with LICOR CLx imager. Indicated molecular masses were estimated using LICOR Image Studio software based on migration of the protein standards.

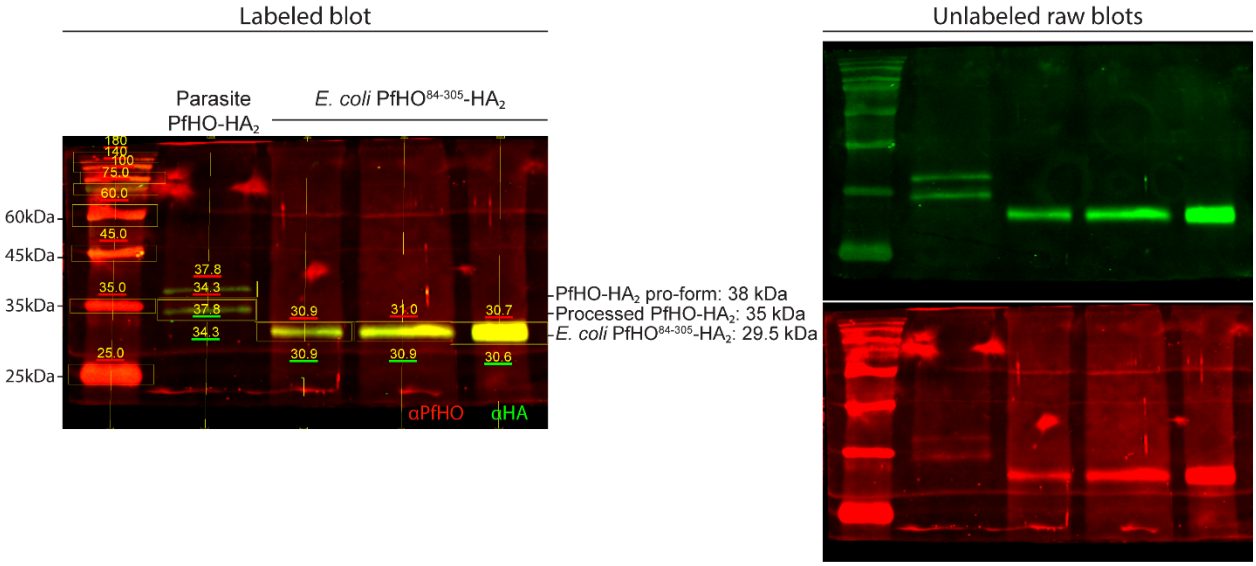

Figure 4 – Source data 2. Uncropped western blot of PfHO-aptamer/TetR-DOZI parasites complemented with episomes expressing PfHO-GFP, ACP_L-HO-GFP, or PfHO N-Term-GFP. Membrane was stained with goat anti-GFP primary and anti-goat-HRP secondary antibodies and visualized by chemiluminescence.

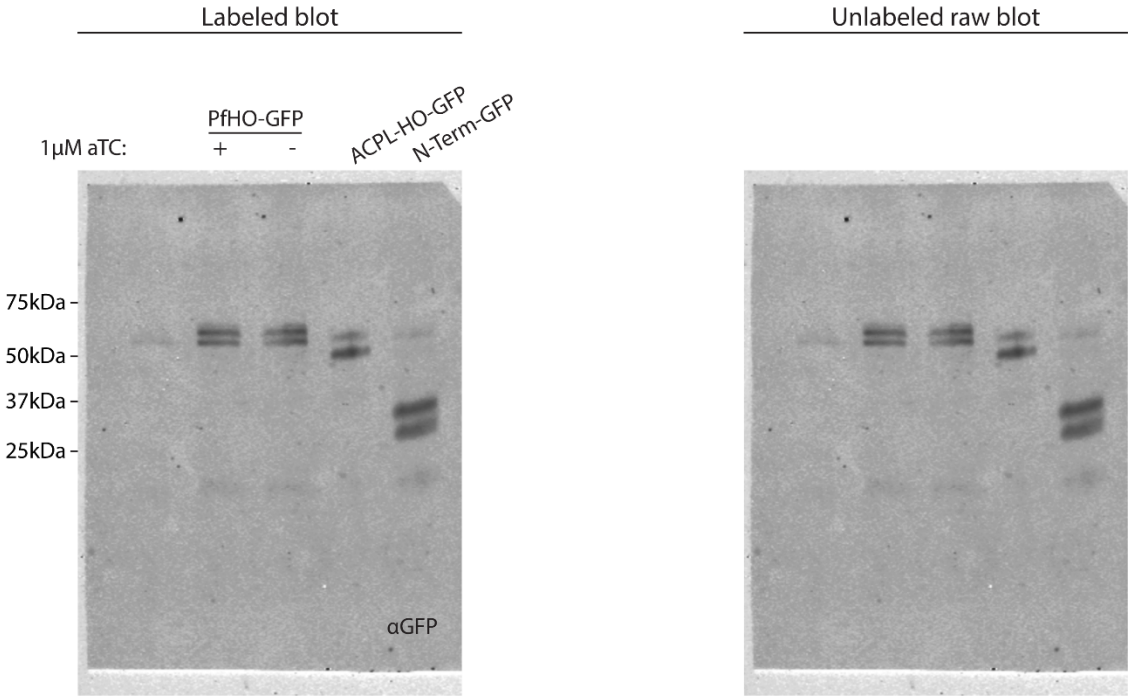

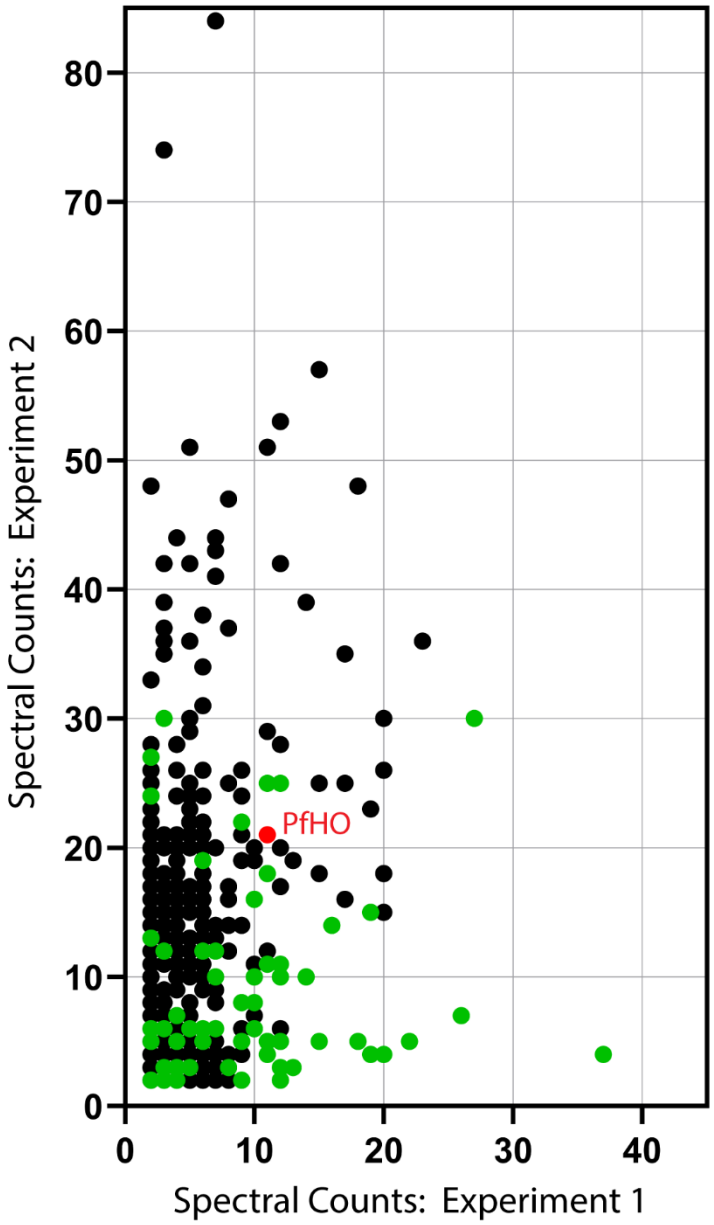

Figure 5 – Figure supplement 1. Spectral counts for proteins that co-purified with PfHO and not with either mitochondrial control in both IP/MS experiments. PfHO is marked in red, and proteins predicted to be apicoplast localized based on prior IP/MS studies are marked in green. The full list of proteins is provided in Figure 5 – source data 1.

apicoplast-localized proteins co-purified with PfHO			Spectral Counts		
Gene ID	Product Description	Gene Name	Exp 1	Exp 2	Average
PF3D7_1025300.1	conserved protein, unknown function	N/A	27	30	28.5
PF3D7_0707800.1	RAP protein, putative	RAP	37	4	20.5
PF3D7_1419200.1	thioredoxin-like protein, putative	ATrx1	12	25	18.5
PF3D7_1406600.1	ATP-dependent Clp protease regulatory subunit ClpC	ClpC	11	25	18
PF3D7_1358000.1	patatin-like phospholipase, putative	PLP	19	15	17
PF3D7_1445100.1	histidine--tRNA ligase, putative	HisRSL	3	30	16.5
PF3D7_0727100.1	conserved protein, unknown function	N/A	26	7	16.5
PF3D7_1011900.1	heme oxygenase	HO	11	21	16
PF3D7_1037100.1	pyruvate kinase 2	PyKII	9	22	15.5
PF3D7_1306200.1	conserved protein, unknown function	N/A	16	14	15
PF3D7_1234600.1	protein TOC75, putative	TOC75	11	18	14.5
PF3D7_1457300.1	MA3 domain-containing protein, putative	N/A	2	27	14.5
PF3D7_1369600.1	conserved Plasmodium protein, unknown function	N/A	22	5	13.5
PF3D7_1304100.1	DNA ligase I	LigI	10	16	13
PF3D7_0627700.1	transportin	TPNO	2	24	13
PF3D7_0530200.1	phosphoenolpyruvate/phosphate translocator	iTPT	6	19	12.5
PF3D7_1106200.1	conserved Plasmodium protein, unknown function	N/A	14	10	12
PF3D7_1225900.1	conserved Plasmodium protein, unknown function	N/A	20	4	12
PF3D7_1022800.1	4-hydroxy-3-methylbut-2-en-1-yl diphosphate synthase (ferredoxin)	ISPG	12	11	11.5
PF3D7_1333200.1	ubiquitin-activating enzyme	UBA1	19	4	11.5
PF3D7_1429100.1	ribosomal protein L15, apicoplast, putative	RPL15	18	5	11.5
PF3D7_1239500.1	DNA gyrase subunit B	GyrB	12	10	11
PF3D7_0804400.1	methionine aminopeptidase 1c, putative	METAP1c	11	11	11
PF3D7_0706100.1	EF hand domain-containing protein, putative	Nop52	10	10	10
PF3D7_1470800.1	conserved Plasmodium protein, unknown function	N/A	15	5	10
PF3D7_1337200.1	1-deoxy-D-xylulose 5-phosphate synthase	DXS	7	12	9.5
PF3D7_0504400.1	ATP-dependent helicase, putative	DDX21	10	8	9
PF3D7_1021300.1	apicoplast integral membrane protein, putative	N/A	6	12	9
PF3D7_1440200.1	stromal-processing peptidase, putative	SPP	12	5	8.5
PF3D7_0313800.1	conserved Plasmodium protein, unknown function	N/A	7	10	8.5
PF3D7_0520800.1	conserved protein, unknown function	N/A	7	10	8.5
PF3D7_0906200.1	conserved Plasmodium protein, unknown function	N/A	9	8	8.5
PF3D7_1411400.1	plastid replication-repair enzyme	PREX	11	5	8
PF3D7_0624400.1	conserved protein, unknown function	N/A	10	6	8
PF3D7_0913700.1	conserved protein, unknown function	N/A	13	3	8
PF3D7_0508800.1	single-stranded DNA-binding protein	SSB	3	12	7.5
PF3D7_0811900.1	RNA-binding protein, putative	RPS1	11	4	7.5
PF3D7_1323600.1	conserved protein, unknown function	N/A	2	13	7.5
PF3D7_0921700.1	conserved protein, unknown function	N/A	12	3	7.5
PF3D7_1223300.1	DNA gyrase subunit A	GyrA	12	2	7
PF3D7_1103400.1	iron-sulfur cluster assembly protein SufD	SufD	9	5	7
PF3D7_0602400.1	elongation factor G	EF-G	7	6	6.5
PF3D7_0719800.1	conserved protein, unknown function	N/A	6	6	6
PF3D7_0815700.1	ubiquitin	Ub	8	3	5.5
PF3D7_0907900.1	peptide deformylase	PDF	5	6	5.5
PF3D7_API02900.1	elongation factor Tu	TUFA	6	5	5.5
PF3D7_1212100.1	peripheral plastid protein 1, putative	PPP1	4	7	5.5
PF3D7_1305100.1	protein AMR3	AMR3	6	5	5.5
PF3D7_0505400.1	conserved protein, unknown function	N/A	9	2	5.5
PF3D7_0104400.1	4-hydroxy-3-methylbut-2-enyl diphosphate reductase	LytB	3	6	4.5
PF3D7_0925300.1	proline--tRNA ligase, putative	aPRS	4	5	4.5
PF3D7_1413400.1	30S ribosomal protein S9, putative	RPS9	5	3	4
PF3D7_0721100.1	conserved protein, unknown function	N/A	2	6	4
PF3D7_1005900.1	conserved protein, unknown function	N/A	2	5	3.5
PF3D7_1228700.1	conserved Plasmodium protein, unknown function	N/A	4	3	3.5
PF3D7_1352000.1	GTP-binding protein, putative	N/A	4	3	3.5
PF3D7_0305000.1	elongation factor Ts	EF-Ts	3	3	3
PF3D7_1106100.1	ribosomal protein S15, apicoplast, putative	RPS15	4	2	3
PF3D7_0411200.1	PP-loop family protein, putative	IleRS	4	2	3
PF3D7_0728800.1	conserved Plasmodium protein, unknown function	N/A	3	3	3
PF3D7_0904700.1	bacterial histone-like protein	HU	3	2	2.5
PF3D7_1210000.1	50S ribosomal protein L1, apicoplast, putative	RPL1	3	2	2.5
PF3D7_1209900.1	ABC transporter B family member 7, putative	ABCB7	2	2	2
PF3D7_0628800.1	glutamyl-tRNA(Gln) amidotransferase subunit B	GATB	2	2	2
PF3D7_1409100.1	aldo-keto reductase, putative	N/A	2	2	2

Figure 5 – Figure supplement 2. List of apicoplast-localized proteins co-purified with PfHO in two IP/MS experiments ordered by average of spectral counts for each experiment.

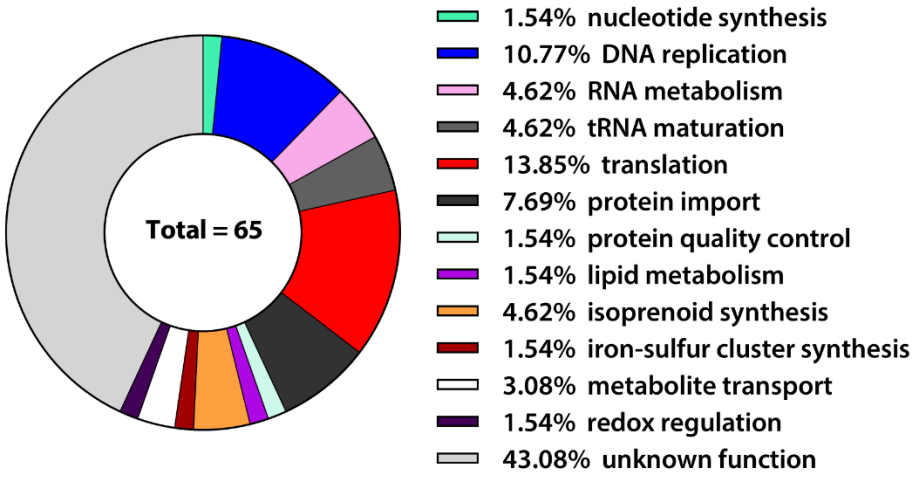

Figure 5 – Figure supplement 3. Functional pathway predictions for the 65 apicoplast-localized proteins that co-purified with PfHO in two IP/MS experiments.

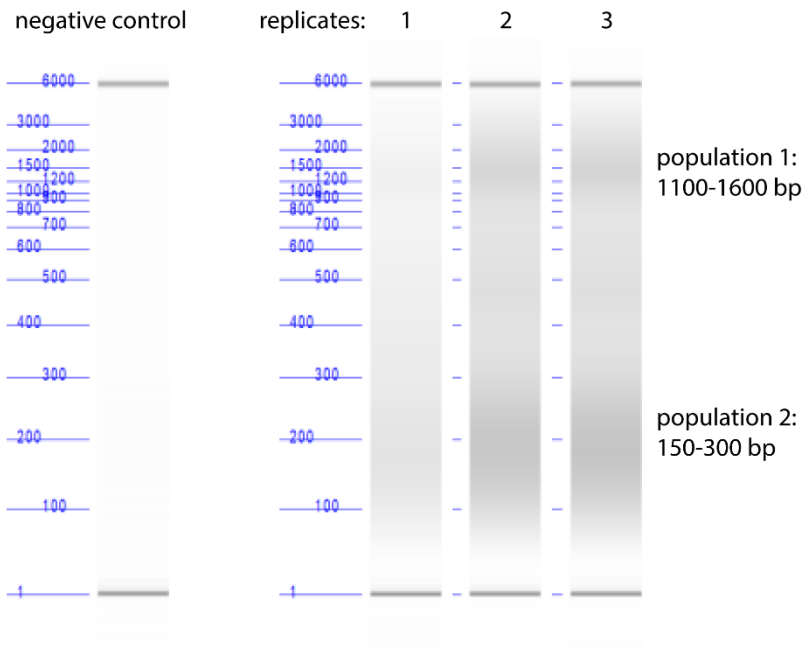

Figure 5 – Figure supplement 4. Quantification of parasite DNA fragment size by Agilent Bioanalyzer DNA analysis after pulse-sonication shearing of parasite lysates. Our DNA shearing method produced two populations of DNA fragment sizes, 1100-1600 bp and 150-300 bp.

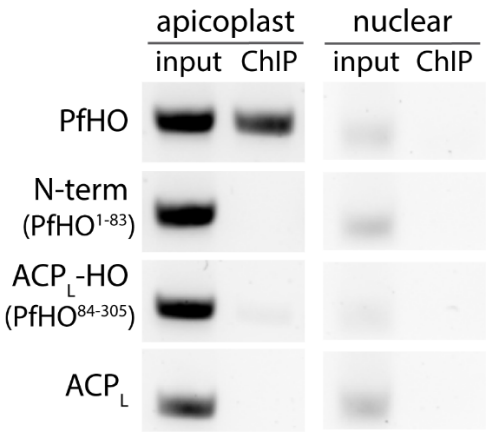

Figure 5 – Figure supplement 5. Steady-state PCR amplification of additional nuclear (mACP: Pf3D7_1208300) and apicoplast (ClpM: Pf3D7_API03600) genes from DNA co-purified with indicated PfHO constructs.

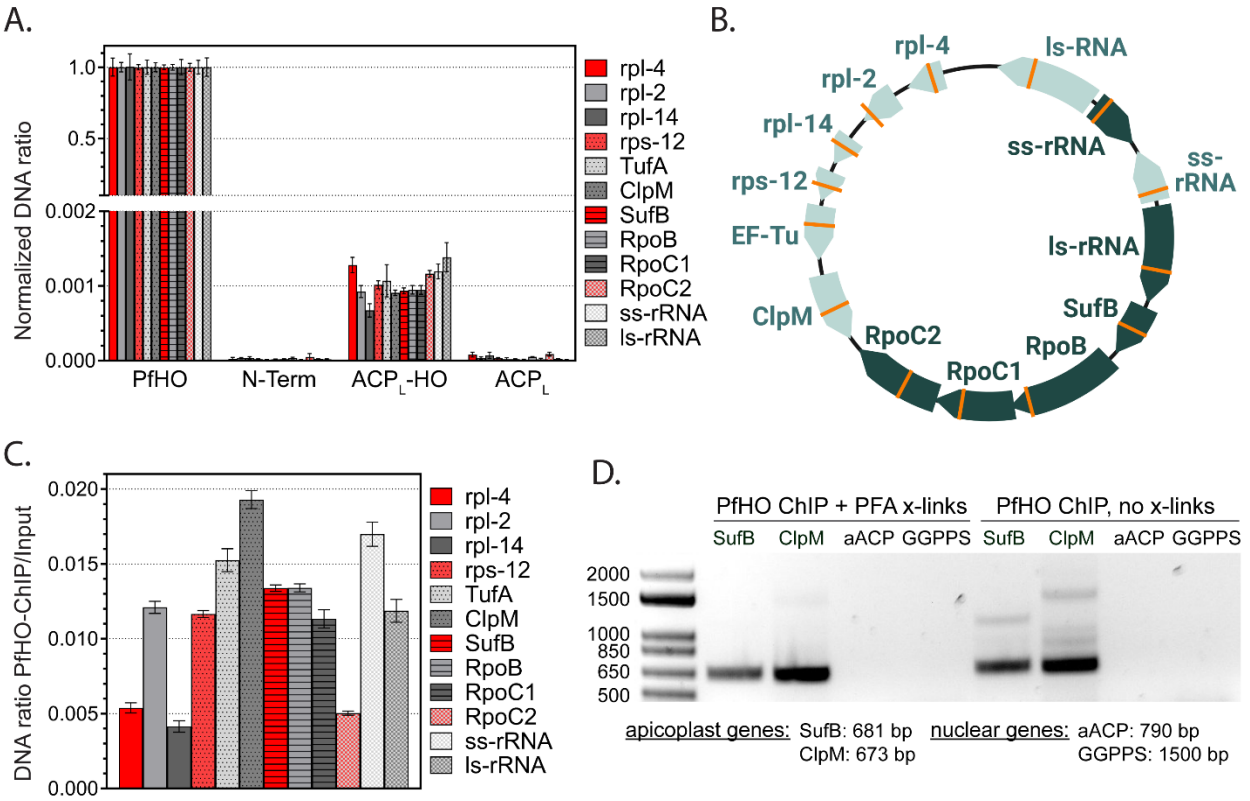

Figure 5 – Figure supplement 6. Additional ChIP experiments in parasites with GFP-tagged PfHO constructs. (A) Relative abundance of apicoplast-encoded genes in DNA co-purified with the indicated GFP-tagged PfHO constructs by ChIP normalized to PfHO-GFP. B) Distribution and orientation of target genes on 35 kb apicoplast genome. Orange lines mark the location of the ~100bp qPCR amplicon for each gene. C) Relative abundance of apicoplast-encoded genes in DNA co-purified with PfHO-GFP by ChIP normalized to input. D) Steady-state PCR amplification of nuclear-encoded (aACP: Pf3D7_0208500, GGPPS: Pf3D7_1128400) and apicoplast-encoded (SufB: Pf3D7_API04700, ClpM: Pf3D7_API03600) genes from DNA co-purified with full-length PfHO-GFP by ChIP ±PFA crosslinking.

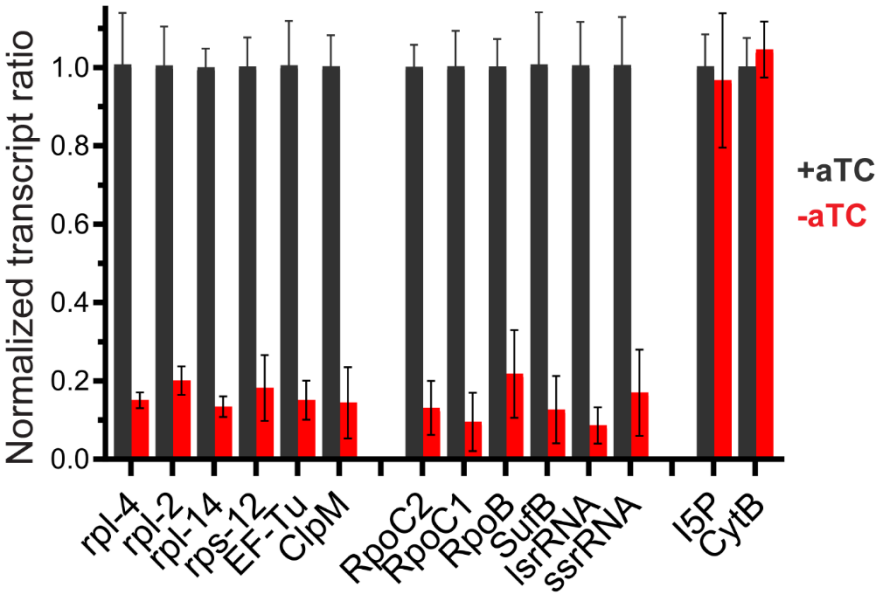

Figure 5 – Figure supplement 7. RT-qPCR data for additional apicoplast genes. Transcript levels of apicoplast, nuclear, and mitochondrial genes were assessed in PfHO-Aptamer/TetR-DOZI parasites grown in ±aTC with 200 µM IPP for 3 days (84 hours post-synchronization). Each transcript is normalized to average of two nuclear transcripts – I5P (Pf3D7_0802500) and ADSL (Pf3D7_0206700). As an additional control, mitochondrial-encoded CytB (Pf3D7_MIT02300) transcript abundance is also measured relative to nuclear controls. Error bars represent average ±SD of independent biological triplicates.

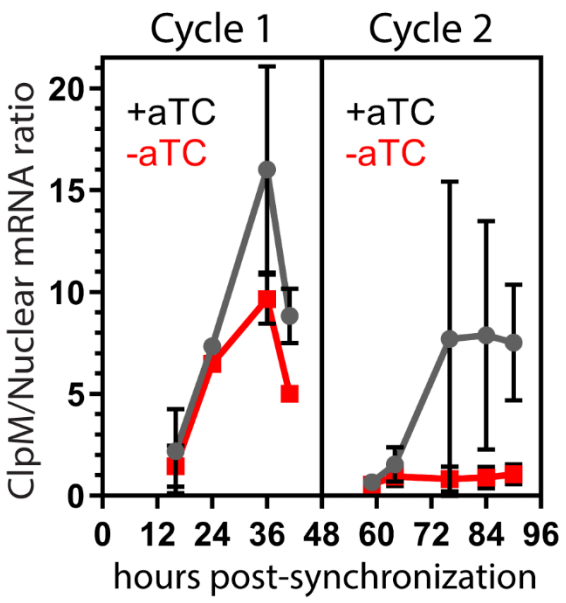

Figure 5 – Figure supplement 8. Representative time-course showing ClpM: nuclear transcript levels at indicated times during first and second cycle of parasite growth ±aTC in the presence of IPP. Large error bars between independent replicate experiments are due to large variance in total ClpM expression. Within each experiment, ClpM transcripts are >10-fold less abundant in -aTC parasites at cycle 2 time-points 72, 84, and 90 hours. Error bars represent average ±SD of independent biological triplicates.

Figure 5 – Source data 1. Table of proteins identified in PfHO IP/MS experiments

Excel file

Figure 5 – Source data 2. Uncropped PCR gel of nuclear-encoded and apicoplast-encoded genes from DNA co-purified with GFP-tagged PfHO constructs. Input ("I") is total parasite DNA collected after parasite lysis and sonication, and ChIP ("C") is DNA eluted from αGFP IP.

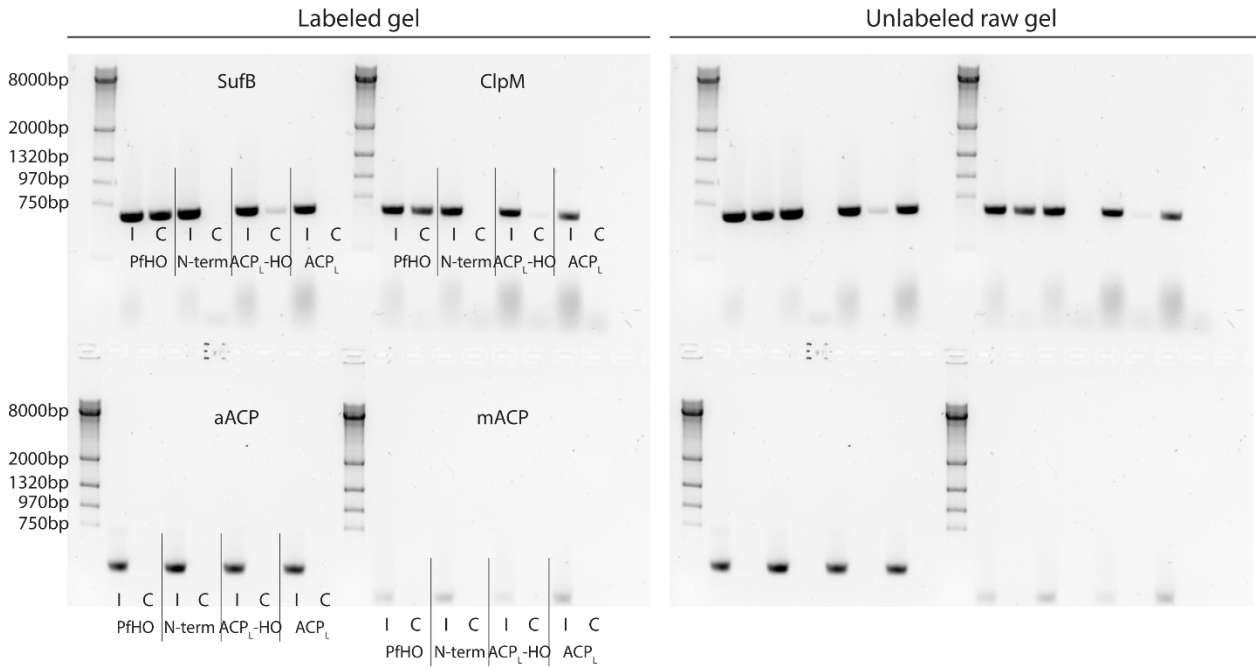

Figure 5 – Source data 3. Uncropped PCR gel of nuclear-encoded and apicoplast-encoded genes from DNA co-purified with GFP-tagged PfHO constructs ±crosslinking.

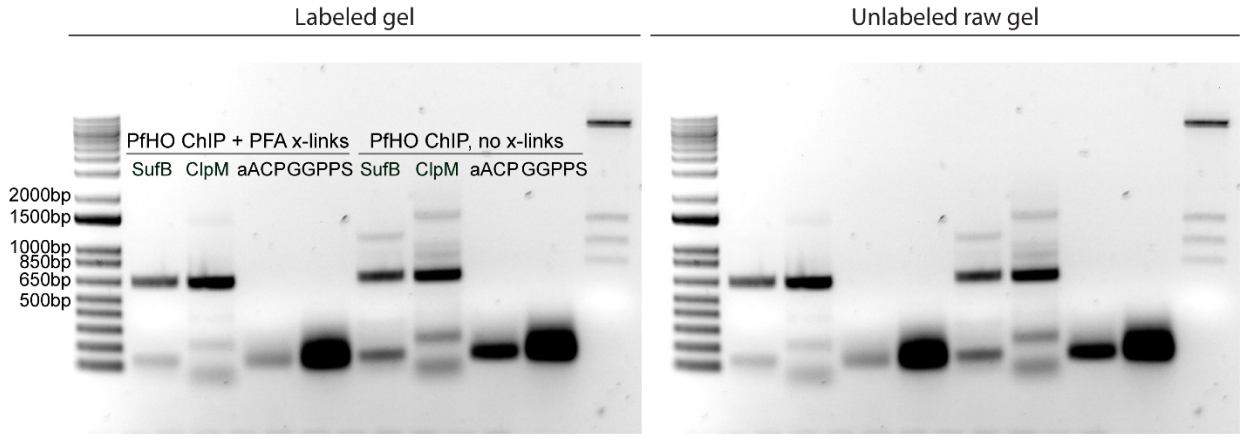

References.

1. Altschul SF, Gish W, Miller W, Myers EW, Lipman DJ. Basic local alignment search tool. *J Mol Biol*. 1990;215(3):403-410. doi:10.1016/S0022-2836(05)80360-2

2. Potter SC, Luciani A, Eddy SR, Park Y, Lopez R, Finn RD. HMMER web server: 2018 update. *Nucleic Acids Res*. 2018;46(W1):W200-W204. doi:10.1093/nar/gky448

3. Amos B, Aurrecoechea C, Barba M, et al. VEuPathDB: the eukaryotic pathogen, vector and host bioinformatics resource center. *Nucleic Acids Res*. 2022;50(D1):D898-D911. doi:10.1093/nar/gkab929

4. Jurrus E, Engel D, Star K, et al. Improvements to the APBS biomolecular solvation software suite. *Protein Sci Publ Protein Soc*. 2018;27(1):112-128. doi:10.1002/pro.3280